

**TWO SELECTED TOPICS INVOLVING THEORY AND APPLICATIONS OF
INFINITE ARRAYS OF MICROSTRIP ELEMENTS**

A Dissertation Presented

by

STEPHEN DONALD TARGONSKI

Submitted to the Graduate School of the
University of Massachusetts in partial fulfillment
of the requirements for the degree of

DOCTOR OF PHILOSOPHY

September 1995

Department of Electrical and Computer Engineering

DISTRIBUTION STATEMENT A

Approved for public release;
Distribution Unlimited

19980115 197

© Copyright by Stephen Donald Targonski 1995

All Rights Reserved

REPORT DOCUMENTATION PAGE			Form Approved OMB No. 0704-0188	
Public reporting burden for this collection of information is estimated to average 1 hour per response, including the time for reviewing instructions, searching existing data sources, gathering and maintaining the data needed, and completing and reviewing the collection of information. Send comments regarding this burden estimate or any other aspect of this collection of information, including suggestions for reducing this burden, to Washington Headquarters Services, Directorate for Information Operations and Reports, 1215 Jefferson Davis Highway, Suite 1204, Arlington, VA 22202-4302, and to the Office of Management and Budget, Paperwork Reduction Project (0704-0188) Washington, DC 20503.				
1. AGENCY USE ONLY (Leave Blank)		2. REPORT DATE September 1995	3. REPORT TYPE AND DATES COVERED Final	
4. TITLE AND SUBTITLE Two Selected Topics Involving Theory and Applications of Infinite Arrays of Microstrip Elements			5. FUNDING NUMBERS AFRL-SR-BL-TR-98- G033	
6. AUTHORS Stephen Donald Targonski				
7. PERFORMING ORGANIZATION NAME(S) AND ADDRESS(ES) University of Massachusetts				
9. SPONSORING/MONITORING AGENCY NAME(S) AND ADDRESS(ES) AFOSR/NI 110 Duncan Avenue, Room B-115 Bolling Air Force Base, DC 20332-8080				
11. SUPPLEMENTARY NOTES				
12a. DISTRIBUTION AVAILABILITY STATEMENT Approved for Public Release			12b. DISTRIBUTION CODE	
13. ABSTRACT (Maximum 200 words) The objective of this work was to develop theory for infinite arrays of microstrip elements, and incorporate that theory into the modeling of large finite arrays. The first topic, the effect of random positioning errors on the input impedance of an infinite array of printed dipoles, utilizes the infinite array solution to gain insight into the reduction or possible elimination of scan blindness for these arrays through the intentional introduction of random element positioning errors. Both planar and linear infinite random arrays are examined. In the second topic, the analysis and design of a microstrip reflectarray using patches of variable size, a rigorous solution to plane wave scattering from an infinite array of microstrip patches is performed. The data from this solution is then used to design a finite sized microstrip reflectarray. Several new topics in reflectarray analysis and design are examined, including the design of millimeter wave microstrip reflectarrays.				
14. SUBJECT TERMS			15. NUMBER OF PAGES	
			16. PRICE CODE	
17. SECURITY CLASSIFICATION OF REPORT Unclassified	18. SECURITY CLASSIFICATION OF THIS PAGE Unclassified	19. SECURITY CLASSIFICATION OF ABSTRACT Unclassified	20. LIMITATION OF ABSTRACT UL	

**TWO SELECTED TOPICS INVOLVING THEORY AND APPLICATIONS OF
INFINITE ARRAYS OF MICROSTRIP ELEMENTS**

A Dissertation Presented

by

STEPHEN DONALD TARGONSKI

Approved as to style and content by:

David M. Pozar, Chairperson of Committee

Daniel H. Schaubert, Member

Robert W. Jackson, Member

George H. Knightly, Outside Member

Daniel H. Schaubert, Department Head
Electrical and Computer Engineering

DEDICATION

I dedicate this dissertation to my parents, Edwin and Judith, whose help and encouragement have aided tremendously in my studies and made the writing of this dissertation possible.

ACKNOWLEDGMENTS

First of all, I would very much like to thank my advisor, Professor David M. Pozar, for all of his guidance, insight, and support of my work during my years at the University of Massachusetts. I would also like to thank the other members of my committee for their ideas and input toward my research, and Harry Syrigos of Alpha Corporation who provided for the fabrication of several of the microstrip reflectarray designs, and without whom much of this work would not have been possible.

ABSTRACT

TWO SELECTED TOPICS INVOLVING THEORY AND APPLICATIONS OF INFINITE ARRAYS OF MICROSTRIP ELEMENTS

SEPTEMBER 1995

STEPHEN DONALD TARGONSKI

B.S.E.E., UNIVERSITY OF MASSACHUSETTS

M.S.E.E., UNIVERSITY OF MASSACHUSETTS

Ph.D., UNIVERSITY OF MASSACHUSETTS

Directed by: Professor David M. Pozar

The objective of this work was to develop theory for infinite arrays of microstrip elements, and incorporate that theory into the modeling of large finite arrays. The first topic, the effect of random positioning errors on the input impedance of an infinite array of printed dipoles, utilizes the infinite array solution to gain insight into the reduction or possible elimination of scan blindness for these arrays through the intentional introduction of random element positioning errors. Both planar and linear infinite random arrays are examined. In the second topic, the analysis and design of a microstrip reflectarray using patches of variable size, a rigorous solution to plane wave scattering from an infinite array of microstrip patches is performed. The data from this solution is then used to design a finite sized microstrip reflectarray. Several new topics in reflectarray analysis and design are examined, including the design of millimeter wave microstrip reflectarrays.

TABLE OF CONTENTS

ACKNOWLEDGEMENTS	v
ABSTRACT	vi
LIST OF TABLES	ix
LIST OF FIGURES	x
 1. EFFECT OF RANDOM POSITIONING ERRORS ON THE INPUT IMPEDANCE OF AN INFINITE ARRAY OF PRINTED DIPOLES	 1
1.1 Introduction	1
1.2 The Infinite Random Planar Array	2
1.3 The Infinite Random Linear Array	13
1.4 A Finite Linear Array Example	14
 2. ANALYSIS AND DESIGN OF MICROSTRIP REFLECTARRAYS USING PATCHES OF VARIABLE SIZE	 34
2.1 Introduction	34
2.2 The Moment Method Solution of Plane Wave Scattering From an Infinite Array of Microstrip Patches	36
2.2.1 An Efficient Mode Set for the Plane Wave Scattering Problem	40
2.2.2 Increasing the Computational Efficiency of the Floquet Mode Summation	45
2.3 Effect of Using TE and TM Incident Field Components	48
2.4 Finite Reflectarray Design	55
2.5 Prime Focus and Offset Feeds	57
2.6 Computation of Reflectarray Directivity	60
2.7 Microstrip Reflectarray Gain Loss Budget	63
2.7.1 Spillover and Taper Loss	64
2.7.2 Dielectric and Conductor Loss	66
2.7.3 Losses Due to Phase Errors	68

3. MICROSTRIP REFLECTARRAY DESIGN EXAMPLES	73
3.1 Introduction	73
3.2 Microstrip Reflectarray Design Example #1	74
3.3 Microstrip Reflectarray Design Example #2	85
3.4 Microstrip Reflectarray Design Example #3	92
3.5 Microstrip Reflectarray Design Example #4	96
3.6 Microstrip Reflectarray Design Example #5	106
3.7 Microstrip Reflectarray Design Example #6	110
4. CONCLUSIONS	114
APPENDIX: GREEN'S FUNCTION FOR THE MICROSTRIP ELEMENT	116
BIBLIOGRAPHY	118

LIST OF TABLES

3.1	List of microstrip reflectarray designs	73
3.2	Gain-loss budget for reflectarray #1	83
3.3	Microstrip reflectarray performance comparison	84
3.4	Gain-loss budget for reflectarray #2	90
3.5	Gain-loss budget for reflectarray #3	94
3.6	Gain-loss budget for reflectarray #4	104
3.7	Gain-loss budget for 9" diameter parabolic reflector	106
3.8	Gain-loss budget for reflectarray #5	110
3.9	Gain-loss budget for reflectarray #6	113

LIST OF FIGURES

1.1	Geometry of the infinite random planar array of printed dipoles	3
1.2	Equivalent circuit for dipoles fed with current generators	7
1.3	Ratio of average dipole (radiated & surface wave) power to total power supplied by source for an infinite planar array of printed dipoles. E-plane scan. Values are normalized at broadside. (a) $a=b=0.5\lambda$, $L=0.39\lambda$, $w=0.01\lambda$, $d=0.19\lambda$, $\epsilon_r=2.55$. (b) $a=b=0.5\lambda$, $L=0.156\lambda$, $w=0.01\lambda$, $d=0.06\lambda$, $\epsilon_r=12.8$	10
1.4	Expected value of input impedance for infinite random planar array versus E-plane scan. Normalized to 50 ohms. $a=b=0.5\lambda$, $L=0.39\lambda$, $w=0.01\lambda$, $d=0.19\lambda$, $\epsilon_r=2.55$	11
1.5	Surface wave efficiency versus E-plane scan for infinite random planar array. (a) $a=b=0.5\lambda$, $L=0.39\lambda$, $w=0.01\lambda$, $d=0.19\lambda$, $\epsilon_r=2.55$. (b) $a=b=0.5\lambda$, $L=0.156\lambda$, $w=0.01\lambda$, $d=0.06\lambda$, $\epsilon_r=12.8$	12
1.6	Geometry of the infinite random linear array of printed dipoles	13
1.7	Ratio of average dipole (radiated & surface wave) power to total power supplied by source for an infinite E-plane linear array of printed dipoles. Values are normalized at broadside. (a) $a=0.5\lambda$, $L=0.39\lambda$, $w=0.01\lambda$, $d=0.19\lambda$, $\epsilon_r=2.55$. (b) $a=0.5\lambda$, $L=0.156\lambda$, $w=0.01\lambda$, $d=0.06\lambda$, $\epsilon_r=12.8$	15
1.8	Surface wave efficiency for an infinite E-plane linear array of printed dipoles. (a) $a=0.5\lambda$, $L=0.39\lambda$, $w=0.01\lambda$, $d=0.19\lambda$, $\epsilon_r=2.55$. (b) $a=0.5\lambda$, $L=0.156\lambda$, $w=0.01\lambda$, $d=0.06\lambda$, $\epsilon_r=12.8$	16
1.9	Ratio of average dipole (radiated & surface wave) power to total power supplied by source for 99 element finite linear array and infinite linear array. Values are normalized at broadside. $a=0.5\lambda$, $L=0.156\lambda$, $w=0.01\lambda$, $d=0.06\lambda$, $\epsilon_r=12.8$. (a) $\delta=0$ (b) $\delta=0.1\lambda$, (c) $\delta=0.2\lambda$, (d) $\delta=0.25\lambda$	19
1.10	Plot of average input impedance for 99 element finite linear array and infinite linear array cases. Values are normalized to 50 ohms. $a=0.5\lambda$, $L=0.156\lambda$, $w=0.01\lambda$, $d=0.06\lambda$, $\epsilon_r=12.8$. (a) $\delta=0$ (b) $\delta=0.1\lambda$, (c) $\delta=0.2\lambda$, (d) $\delta=0.25\lambda$	21

1.11 Average surface wave efficiency for 99 element finite linear arrays and infinite linear array. $a=0.5\lambda$, $L=0.156\lambda$, $w=0.01\lambda$, $d=0.06\lambda$, $\epsilon_r=12.8$. (a) $\delta=0$ (b) $\delta=0.1\lambda$, (c) $\delta=0.2\lambda$, (d) $\delta=0.25\lambda$	27
1.12 Distribution of reflection coefficient magnitude for periodic finite linear arrays. Five 99 element arrays considered. (a) Broadside. (b) 45 degree scan	29
1.13 Distribution of reflection coefficient magnitude for finite linear arrays with $\delta=0.25\lambda$. Five 99 element arrays considered. (a) Broadside. (b) 45 degree scan	30
1.14 Radiation patterns for a 99 element E-plane linear array of printed dipoles with randomly spaced elements. Element positions were generated with $\delta=0.2\lambda$. $a=0.5\lambda$, $l=0.156\lambda$, $w=0.01\lambda$, $d=0.06\lambda$, $\epsilon_r=12.8$	32
2.1 Geometry of the infinite array scattering problem. (a) Rectangular array grid. (b) Triangular array grid	38
2.2 Computed reflection phase of infinite array of microstrip patches versus number of entire domain expansion modes. Thick line is reflection phase computed with one entire domain mode and one edge condition mode. $f=27.3$ GHz, $a=.6087$ cm, $b=.6667$ cm, $\epsilon_r=2.95$, $d=.0254$ cm, $\tan \delta=.0074$, $l=.3$ cm, $w=.3$ cm, $\theta=0^\circ$, $\phi=0^\circ$	42
2.3 Computed magnitude of current coefficients of entire domain expansion modes for the moment method solution of an infinite array of microstrip patches versus mode number. $f=27.3$ GHz, $a=.6087$ cm, $b=.6667$ cm, $\epsilon_r=2.95$, $d=.0254$ cm, $\tan \delta=.0074$, $l=.3$ cm, $w=.3$ cm, $\theta=0^\circ$, $\phi=0^\circ$	43
2.4 Area of summation of Floquet modes in the spectral domain. Indices shown are m,n . (a) Square region. (b) Hyperbolic region	46
2.5 Contour plot of magnitude of $i=1, j=1$ impedance matrix element versus m,n . $f=27.3$ GHz, $a=.6087$ cm, $b=.6667$ cm, $\epsilon_r=2.95$, $d=.0254$ cm, $\tan \delta=.0074$, $l=.3$ cm, $w=.3$ cm, $\theta=0^\circ$, $\phi=0^\circ$	47
2.6 Computed reflection coefficient phase versus element length using Floquet mode summation over rectangular and hyperbolic regions. $f=27.3$ GHz, $a=.6087$ cm, $b=.6667$ cm, $\epsilon_r=2.95$, $d=.0254$ cm, $\tan \delta=.0074$, $l=.3$ cm, $w=.3$ cm, $\theta=0^\circ$, $\phi=0^\circ$	49

2.7	Computed reflection coefficient phase versus azimuth incidence angle for different elevation incidence angles. $f=28$ GHz, $a=.5442$ cm, $b=.5442$ cm, $\epsilon_r=2.2$, $d=.0508$ cm, $\tan \delta=.0028$, $l=.315$ cm, $w=.315$ cm	52
2.8	Example of equivalent currents used in computer model for reflectarray scattered field. $f=27.3$ GHz, $a=.6087$ cm, $b=.6667$ cm, $\epsilon_r=2.95$, $d=.0254$ cm, $\tan \delta=.0074$, $l=.3$ cm, $w=.3$ cm, $\theta=0^\circ$, $\phi=0^\circ$	54
2.9	Geometry of finite sized reflectarray. (a) Side view. (b) Top view	56
2.10	Position of main beam versus frequency for 64 element E-plane linear reflectarray. Feed illumination is $\cos^8 \theta$. $x_{\text{off}}=-42$ cm, $h=50$ cm for offset feed; $h=70$ cm for prime focus feed	61
2.11	Computed ohmic (conductor and dielectric) losses for reflectarray elements. (a) for varying substrate thicknesses; element width is 0.4cm. (b) for varying element widths; substrate thickness is 0.0508cm. $f=27.3$ GHz, $a=.6087$ cm, $b=.6667$ cm, $\epsilon_r=2.95$, $\tan \delta=.0074$, $\theta=0^\circ$, $\phi=0^\circ$	69
2.12	Reflection phase versus patch length for plane wave scattering from an infinite array of microstrip patches. $f=27.3$ GHz, $a=.6087$ cm, $b=.6667$ cm, $\epsilon_r=2.95$, $d=.0254$ cm, $\tan \delta=.0074$, $l=.3$ cm, $w=.3$ cm, $\theta=0^\circ$, $\phi=0^\circ$	71
3.1	Scaled drawing of reflectarray design example #1	75
3.2	Computed reflection phase of infinite array of microstrip patches versus patch length. Triangular array grid. $f=5.3$ GHz, $a=5.39$ cm, $b=3.23$ cm, $\alpha=33.4^\circ$, $\epsilon_r=2.33$, $d=.158$ cm, $\tan \delta=.001$, $w=2.382$ cm, $\theta=0^\circ$, $\phi=0^\circ$	76
3.3	E-plane patterns at 5.2 GHz for reflectarray example #1	78
3.4	H-plane patterns at 5.2 GHz for reflectarray example #1	79
3.5	H-plane cross-polarization patterns at 5.2 GHz for reflectarray example #1 ...	80
3.6	Measured E-plane radiation patterns at 5.2 GHz and 5.7 GHz	82
3.7	Measured and computed gain for reflectarray design example #1	83
3.8	Scaled drawing of reflectarray design example #2	86
3.9	Measured and computed E-plane radiation patterns at 27.3 GHz for design example #2	88

3.10 Measured and computed H-plane radiation patterns at 27.3 GHz for design example #2	89
3.11 Measured and computed gain for reflectarray design example #2	91
3.12 Scaled drawing of reflectarray design example #3	93
3.13 Measured and computed gain for reflectarray design example #3	95
3.14 Scaled drawing of reflectarray design example #4	97
3.15 Backfire feed used in reflectarray design example #4	98
3.16 Measured E-plane pattern from backfire feed and computed pattern from pyramidal horn used to model feed. Frequency = 27 GHz	99
3.17 Measured H-plane pattern from backfire feed and computed pattern from pyramidal horn used to model feed. Frequency = 27 GHz	100
3.18 Measured and computed E-plane radiation patterns at 27.3 GHz for reflectarray #4	102
3.19 Measured and computed H-plane radiation patterns at 27.3 GHz for reflectarray #4	103
3.20 Measured gain for reflectarray design example #4	104
3.21 Actual size overhead drawing of reflectarray design example #5	107
3.22 Computed and measured radiation patterns for reflectarray #5. Measured patterns at 75 GHz; computed at 76.5 GHz. (a) E-plane. (b) H-plane	109
3.23 Geometry of cassegrain feed for reflectarray design example #6	111
3.24 Measured and computed radiation patterns at 76.5 GHz for reflectarray #6. (a) E-plane. (b) H-plane	112

CHAPTER 1

EFFECT OF RANDOM POSITIONING ERRORS ON THE INPUT IMPEDANCE OF AN INFINITE ARRAY OF PRINTED DIPOLES

1.1 Introduction

A problem in the use of phased arrays of printed elements is the appearance of scan blindnesses at certain angles [1]. These blindnesses occur because the mutual coupling between the elements in the array add in phase at the blind angles, creating a highly reactive input impedance. This problem can be alleviated by introducing random positioning of the elements in the array, thereby randomizing the phase of the mutual impedance between the elements.

Two articles discuss the removal of scan blindness through the use of random element positioning [2,3]. However, these and other papers on random arrays have always studied the effect on the array pattern only, and have not examined the input impedance of the elements.

In order to study the effect of random positioning errors in an infinite array an impedance analysis must be done, since there is no specific definition of an antenna pattern for an infinite array. The active element pattern is often referred to, however, this also depends on the input impedance of the elements. In this chapter the solution for the expected value of the input impedance of an infinite array of printed dipoles on a dielectric substrate is presented. However, a limitation exists in the analysis in the fact that the terminal current at each dipole must be fixed.

Specifically, in this chapter:

- Two infinite planar arrays with random positioning and varying degrees of randomization will be analyzed.
- Two infinite linear arrays with random positioning and varying degrees of randomization will be analyzed.
- Averaged results from several large, but finite, random linear arrays will be compared to the results from an infinite random linear array to validate the analysis.

1.2 The Infinite Random Planar Array

The geometry of the infinite random planar array is shown in Figure 1.1. The element positions along the x axis are placed at $x_m = ma + \Delta_m$, where the Δ_m 's are independent identically distributed uniform random variables with zero mean defined on the interval $[-\delta, \delta]$. This formulation is of the form of a "binned" random array [4], as compared to the totally random array. It has been shown that for element spacings of less than a wavelength, scan blindness for this array geometry occurs primarily in the E-plane [1]. Therefore, randomization has only been introduced in the x-direction.

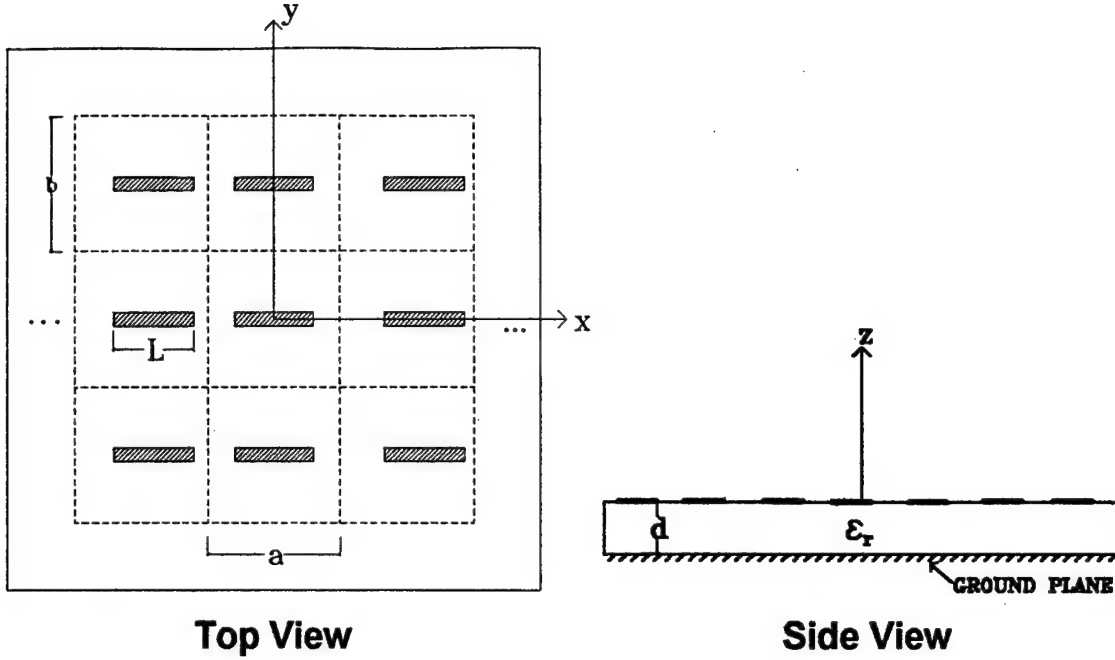


Figure 1.1 Geometry of the infinite random planar array of printed dipoles.

A theoretical approach similar to the one presented in reference [1] was used, with a single PWS mode assumed for the current on each dipole. The single PWS mode, while not providing a rigorous solution for the actual input impedance, should be sufficient for predicting the existence or non-existence of scan blindnesses.

The analysis begins with the Green's function for the electric field at (x, y, d) of a single infinitesimal electric dipole located at (x_o, y_o, d) on a grounded dielectric slab,

$$G_{xx}(x, y | x_o, y_o) = -\frac{jZ_o}{4\pi^2 k_o} \int_{-\infty}^{\infty} \int_{-\infty}^{\infty} Q_{xx}(k_x, k_y) e^{jk_x(x-x_o)} e^{jk_y(y-y_o)} dk_x dk_y \quad (1-1)$$

where Z_o is the intrinsic impedance of free space and the kernel function Q_{xx} is listed in the Appendix.

For the infinite planar random array, the total electric field is the superposition of the electric field from each element. The elements are phased to produce a beam in the $(u,v)=(\sin \theta \cos \phi, \sin \theta \sin \phi)$ direction, and the appropriate phasing is selected to account for the non-periodic positioning. This yields

$$E_x(x,y) = -\frac{jZ_o}{4\pi^2 k_o} \sum_{m=-\infty}^{\infty} \sum_{n=-\infty}^{\infty} e^{jk_o[(ma+\Delta_m)u+nbv]} \int_{-\infty}^{\infty} \int_{-\infty}^{\infty} Q_{xx}(k_x, k_y) F(k_x, k_y) e^{jk_x(x-ma-\Delta_m)} e^{jk_y(y-nb)} dk_x dk_y \quad (1-2)$$

In the above expression, $F(k_x, k_y)$ is the Fourier transform of the piecewise sinusoidal mode used on the dipoles, given by

$$F(k_x, k_y) = \frac{2k_e(\cos k_x h - \cos k_e h)}{\sin k_e h(k_e^2 - k_x^2)} \frac{\sin k_y w/2}{k_y w/2} \quad (1-3)$$

where h is the mode half-length and $k_e = k_o \sqrt{(\epsilon_r + 1)/2}$.

The input impedance of the $(m,n)=(0,0)$ dipole can then be computed as

$$Z_{in}^{00} = -\iint_S E_x(x,y) \cdot J_x(x,y) dx dy \quad (1-4)$$

where the area of integration is over the surface of the dipole. This yields

$$Z_{in}^{00} = \frac{jZ_o}{4\pi^2 k_o} \sum_{m=-\infty}^{\infty} \sum_{n=-\infty}^{\infty} e^{jk_o(mau+nbv)} \int_{-\infty}^{\infty} \int_{-\infty}^{\infty} Q_{xx}(k_x, k_y) F^2(k_x, k_y) e^{jk_x ma} e^{jk_y nb} e^{j(k_o u - k_x)(\Delta_m - \Delta_0)} dk_x dk_y \quad (1-5)$$

The above equation for the input impedance is a random variable which is a function of the independent random variables Δ_m . The expected value of a function of a random variable is computed as

$$E[Y] = \int_{-\infty}^{\infty} g(x) f_X(x) dx \quad (1-6)$$

where the random variable Y is a function of the random variable X, i.e. $Y=g(X)$. Also, $f_X(x)$ is the probability density function for X.

Using (1-6), the expected value of input impedance is computed as

$$E[Z_{in}] = \frac{jZ_o}{4\pi^2 k_o} \sum_{m=-\infty}^{\infty} \sum_{n=-\infty}^{\infty} e^{jk_o(mau+nbv)} \int_{-\infty}^{\infty} \int_{-\infty}^{\infty} Q_{xx}(k_x, k_y) F^2(k_x, k_y) e^{jk_x ma} e^{jk_y nb} E[e^{j(k_o u - k_x)(\Delta_m - \Delta_0)}] dk_x dk_y \quad (1-7a)$$

where

$$E[e^{j(k_o u - k_x)(\Delta_m - \Delta_0)}] = \begin{cases} 1 & ; m = 0 \\ S(k_x) & ; m \neq 0 \end{cases} \quad (1-7b)$$

and

$$S(k_x) = \left(\frac{\sin(k_o u - k_x) \delta}{(k_o u - k_x) \delta} \right)^2 \quad (1-7c)$$

While the input impedance of (1-6) is not periodic, the expected value of (1-7a) is. Therefore, the Poisson sum formula can be applied to this expression. Applying the formula and performing some algebraic manipulation yields

$$E[Z_{in}] = \frac{jZ_o}{2\pi b k_o} \sum_{n=-\infty}^{\infty} \int_{-\infty}^{\infty} Q(k_x, k_y) F^2(k_x, k_y) [1 - S(k_x)] dk_x + \frac{jZ_o}{ab k_o} \sum_{m=-\infty}^{\infty} \sum_{n=-\infty}^{\infty} Q(k_x, k_y) F^2(k_x, k_y) S(k_x) \quad (1-8)$$

The first term in (1-7) resembles the solution for an infinite H-plane linear array, while the second term resembles the solution of an infinite planar array. For E-plane scan the first term remains constant, but the second term contributes a scan blindness. This blindness is caused by coupling to higher-order Floquet modes [1].

An interesting result occurs when the degree of randomization is increased by enlarging δ . As δ approaches $0.5a$, its maximum allowable extent, the function $S(k_x)$ approaches zero for $m \neq 0$. This has the effect of eliminating coupling to any higher-order Floquet modes, thereby eliminating the scan blindness, at least in the average sense.

At this time an important point must be brought up in the analysis. In the above formulation, the terminal current on each dipole is held constant with uniform amplitude. While this assumption is valid for the periodic array, in the case of the random array differences in the mutual coupling between elements will in general excite different

currents on each dipole. Therefore, for the analysis to be valid, each dipole must be fed with a current generator which holds the dipole currents fixed as their positions are varied inside each bin. This gives rise to the equivalent circuit shown in Figure 1.2. Here a current generator with internal impedance Z_b^* feeds the dipole with input impedance Z_d . As the position of the dipole varies inside the bin, the current supplied by the generator changes accordingly to keep the current i_d constant. This fact is not critical in interpreting the results of the infinite array analysis, however, it becomes crucial when formulating large finite arrays that simulate the behavior of the random infinite array.

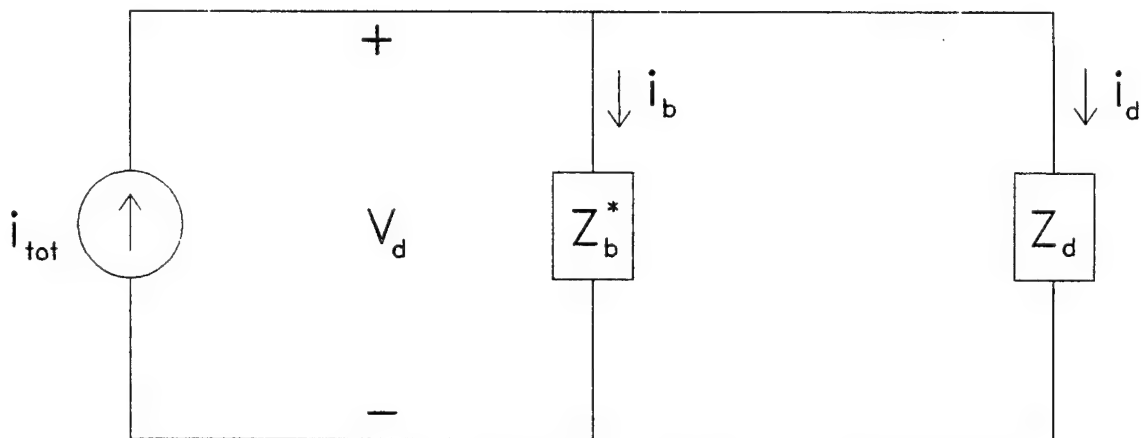


Figure 1.2. Equivalent circuit for dipoles fed with current generators.

From this equivalent circuit, the total power supplied and the portion supplied to the dipole can be easily computed. Keeping in mind that the magnitude of the dipole current, i_d , is unity and is fixed, we get

$$P_{tot} = \operatorname{Re} \left\{ \frac{|Z_d|^2}{Z_b} + Z_d \right\} \quad (1-9a)$$

$$P_d = \operatorname{Re}\{Z_d\} \quad (1-9b)$$

In the case of the random infinite array considered here, $Z_d = E[Z_{in}]$. The power P_d as defined in (1-9b) can be interpreted as the average combined radiated power and power launched into surface waves.

The surface wave efficiency, computed from the expected value of radiated power and power coupled into surface waves, of the infinite random planar array is an interesting topic. For the periodic infinite planar array, there is no power transferred into surface waves except exactly when scan blindness occurs - i.e. for all other scan angles the surface wave efficiency is 100%. However, as randomization of the element positioning is introduced, power can be coupled into surface waves. The mathematical interpretation of this power is the contribution of the surface wave poles in the first term of (1-8). The contribution of these poles is included in the numerical calculation of the infinite integral, and is denoted as Z_{sw} . The surface wave efficiency is then computed as

$$\eta_{sw} = \frac{\operatorname{Re}\{E[Z_{in}] - Z_{sw}\}}{\operatorname{Re}\{E[Z_{in}]\}} \quad (1-10)$$

Examples of the ratio of average power dissipated by the dipole array to the total power supplied by the source are shown in Figures 1.3a and 1.3b. Scan is in the E-plane. The average power is plotted for various degrees of randomization. It is evident from the figure that for the periodic array ($\delta=0$) a scan blindness occurs around 45° for both cases. The blindness is narrowed as randomization is introduced but is not completely removed until the maximum amount of randomization ($\delta=.25\lambda$) is introduced.

The expected value of input impedance for an infinite random planar array is plotted on a 50 ohm Smith chart in Figure 1.4. Again, it is evident that a blindness appears at 45.6° in the E-plane. This plot gives an insight into the blindness phenomenon for the infinite random array, especially the curve for $\delta=0.2\lambda$. The expected value of the impedance for this particular randomization follows the curve for $\delta=0.25\lambda$ closely except near the blindness angle, where it exhibits behavior similar to the periodic array. As will be seen in the next section, blindness in the infinite linear array exhibits a different behavior.

The surface wave efficiency for both examples is shown in Figures 1.5a and 1.5b. For the periodic array, no power is coupled into the surface wave except exactly at blindness, yielding an efficiency of unity at all other angles. As the degree of randomization is increased, more power is allowed to be coupled into a surface wave thereby decreasing the efficiency. The efficiency of the example shown in Figure 1.4b has a markedly lower efficiency than the example of Figure 1.4a, suggesting a "stronger" surface wave in this case.

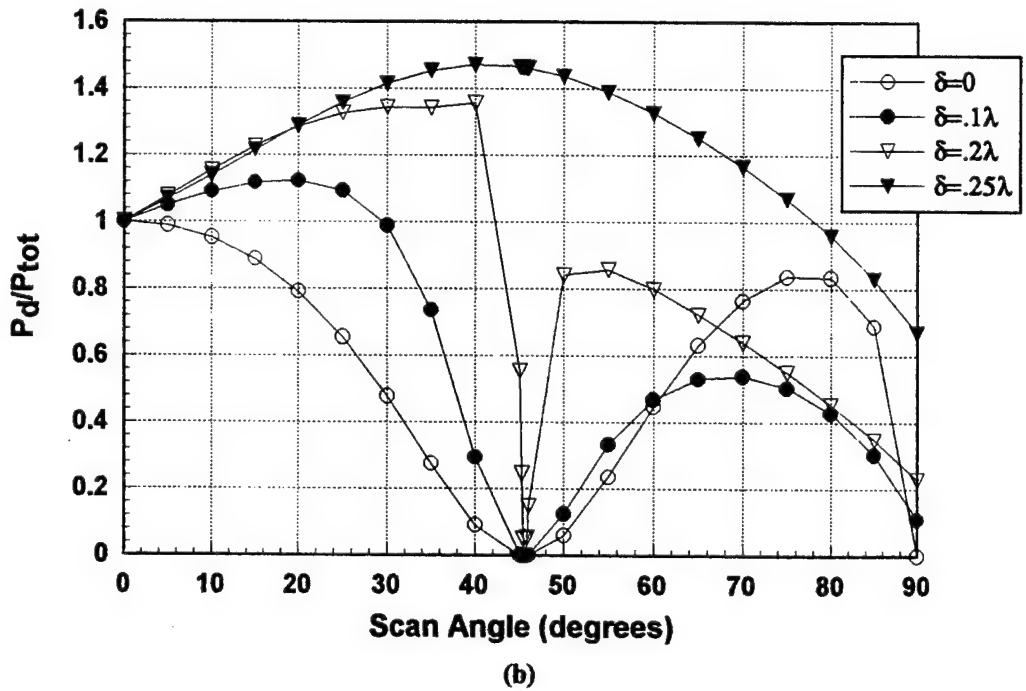
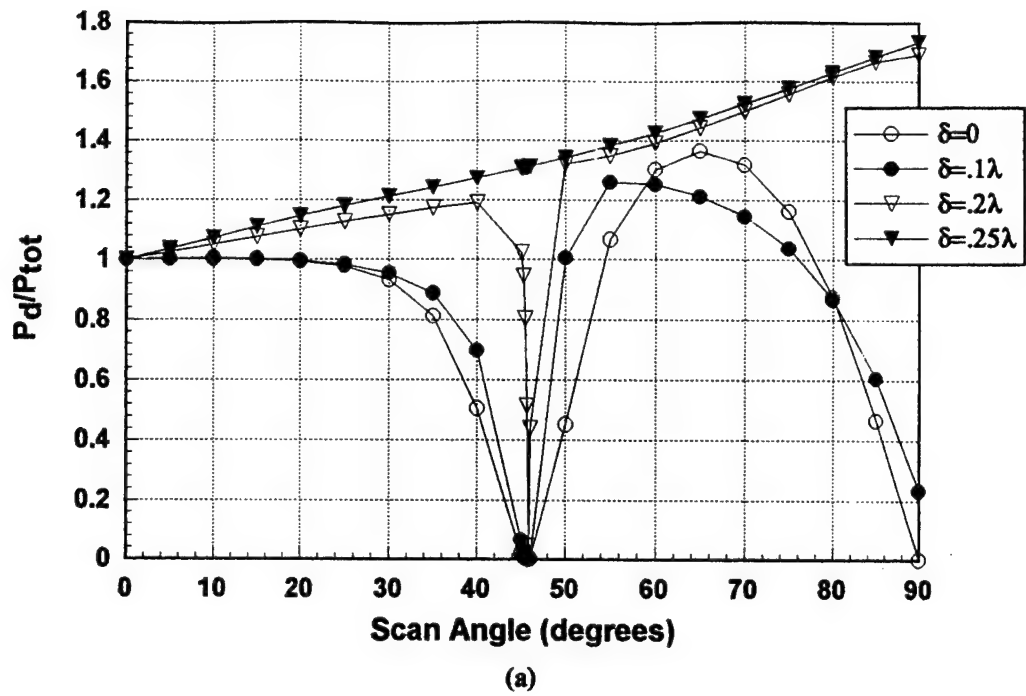


Figure 1.3. Ratio of average dipole (radiated & surface wave) power to total power supplied by source for an infinite planar array of printed dipoles. E-plane scan. Values are normalized at broadside. (a) $a=b=0.5\lambda$, $L=0.39\lambda$, $w=0.01\lambda$, $d=0.19\lambda$, $\epsilon_r=2.55$. (b) $a=b=0.5\lambda$, $L=0.156\lambda$, $w=0.01\lambda$, $d=0.06\lambda$, $\epsilon_r=12.8$.

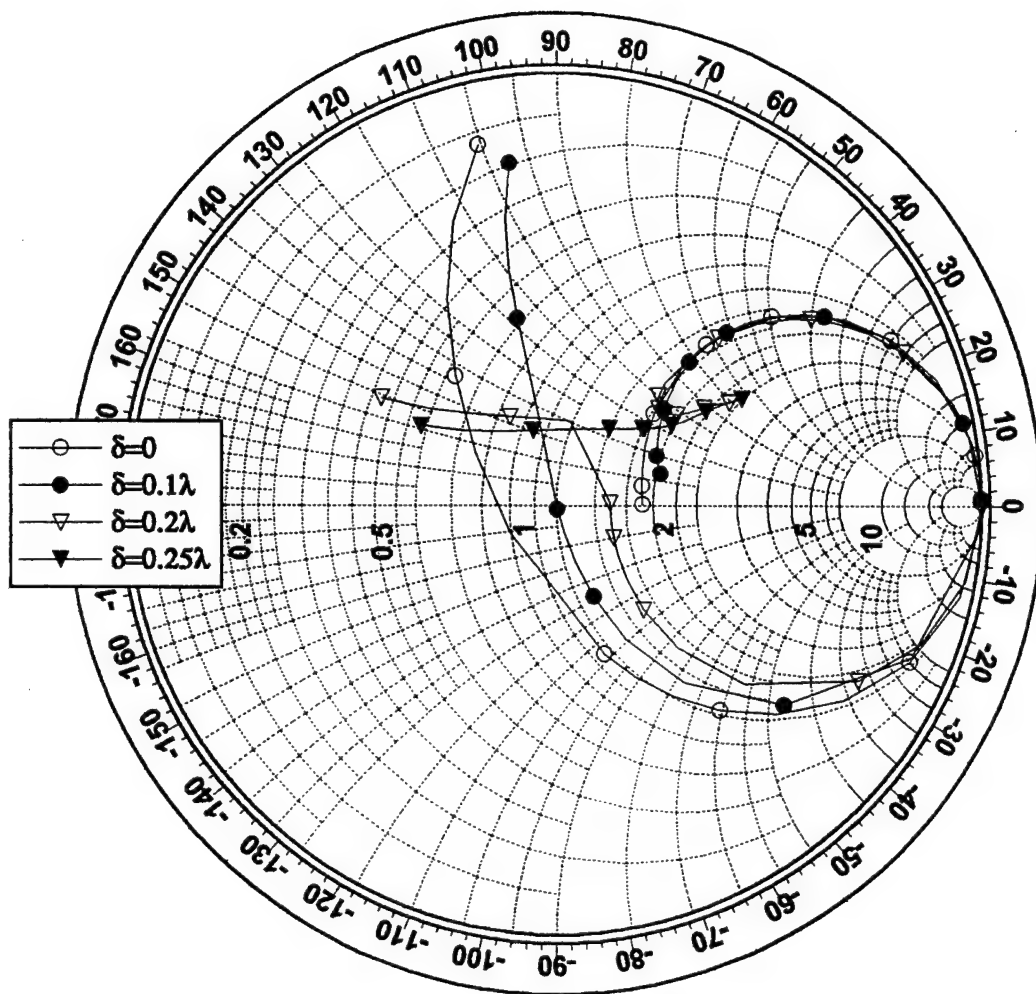
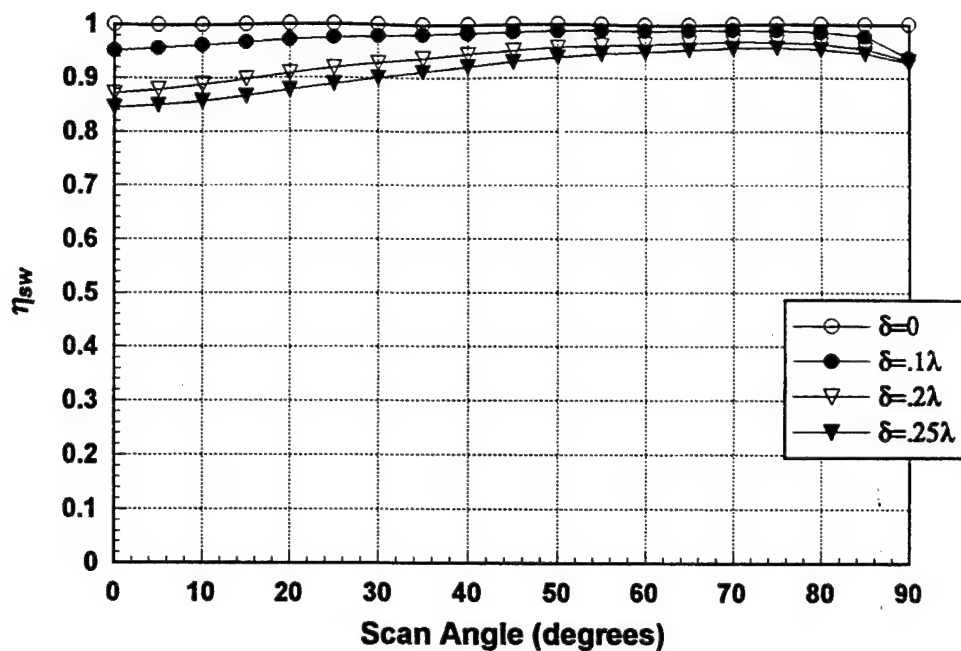
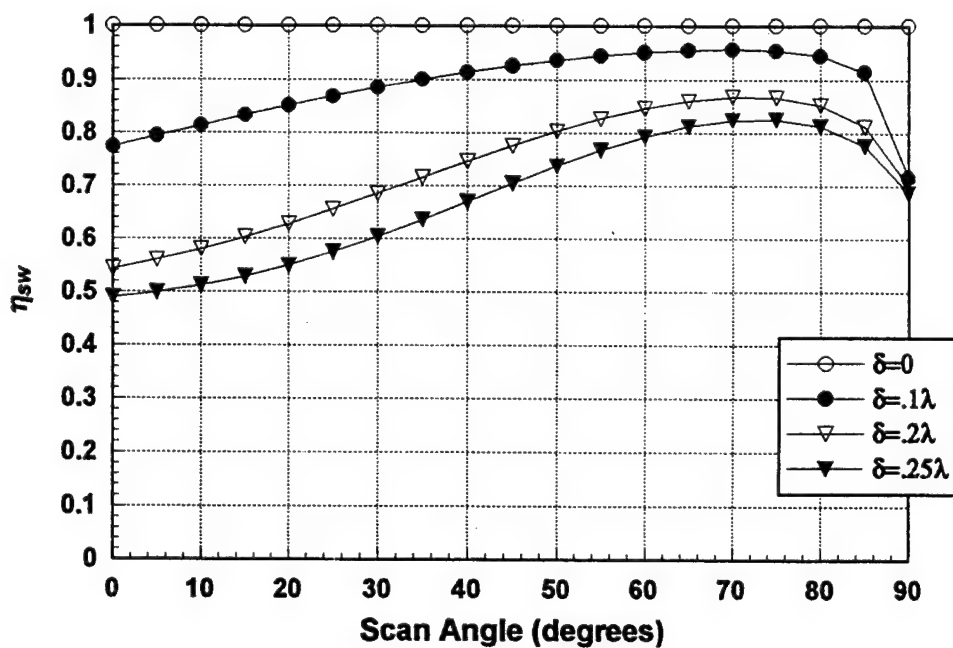


Figure 1.4. Expected value of input impedance for infinite random planar array versus E-plane scan. Normalized to 50 ohms. $a=b=0.5\lambda$, $L=0.39\lambda$, $w=0.01\lambda$, $d=0.19\lambda$, $\epsilon_r=2.55$.



(a)



(b)

Figure 1.5. Surface wave efficiency versus E-plane scan for infinite random planar array.
 (a) $a=b=0.5\lambda$, $L=0.39\lambda$, $w=0.01\lambda$, $d=0.19\lambda$, $\epsilon_r=2.55$. (b) $a=b=0.5\lambda$, $L=0.156\lambda$, $w=0.01\lambda$, $d=0.06\lambda$, $\epsilon_r=12.8$.

1.3 The Infinite Random Linear Array

The geometry of the infinite random linear array is shown in Figure 1.6. The geometry is similar to that of the planar array, with element positions along the x axis given by $x_m = ma + \Delta_m$, where the Δ_m 's are as defined in the previous section. The equivalent circuit shown in Figure 1.2 is used to feed the elements. An E-plane array is considered.

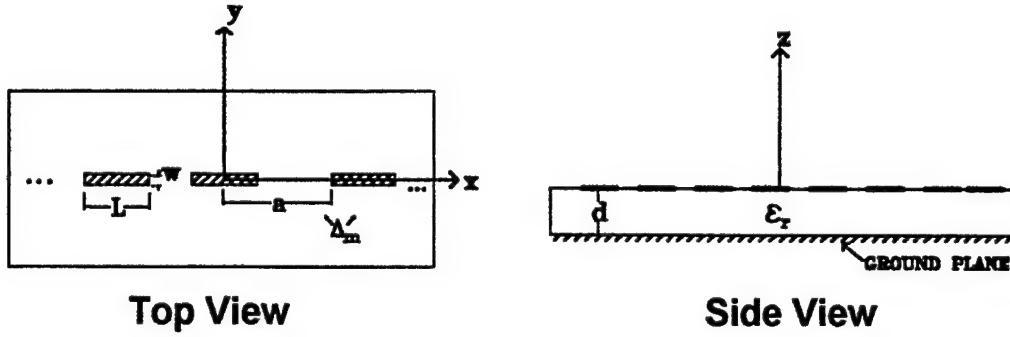


Figure 1.6 Geometry of the infinite random linear array of printed dipoles.

The method of analysis closely follows that of the planar array with a single PWS mode assumed for the current on each dipole. The total electric field for the array in the array plane is given by

$$E_x(x, y) = -\frac{jZ_o}{4\pi^2 k_o} \sum_{m=-\infty}^{\infty} e^{jk_o[(ma + \Delta_m)u]} \int_{-\infty}^{\infty} \int_{-\infty}^{\infty} Q_{xx}(k_x, k_y) F(k_x, k_y) e^{jk_x(x - ma - \Delta_m)} e^{jk_y y} dk_x dk_y \quad (1-11)$$

Following the same steps taken in the analysis of the planar array yields the expected value of the input impedance as

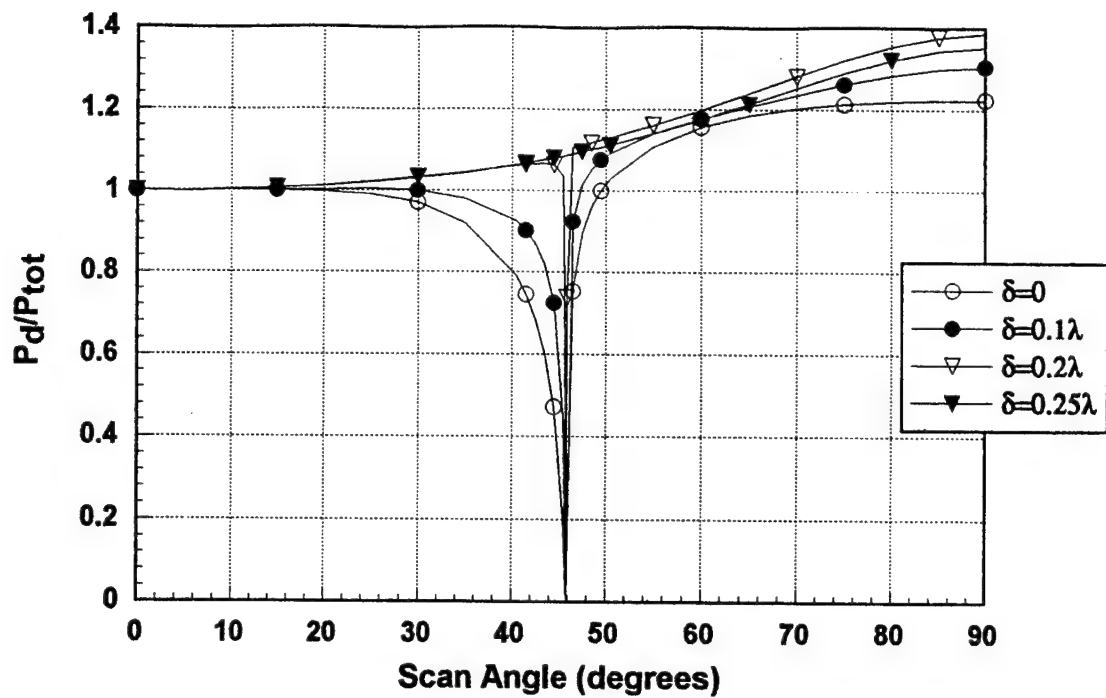
$$E[Z_{in}] = \frac{jZ_o}{4\pi^2 k_o} \int_{-\infty}^{\infty} \int_{-\infty}^{\infty} Q(k_x, k_y) F^2(k_x, k_y) [1 - S(k_x)] dk_x dk_y + \frac{jZ_o}{2\pi a k_o} \sum_{m=-\infty}^{\infty} \int_{-\infty}^{\infty} Q(k_x, k_y) F^2(k_x, k_y) S(k_x) dk_y \quad (1-11)$$

Examples of the ratio of average power dissipated by the dipole array to the total power supplied by the source are shown in Figures 1.7a and 1.7b. For the periodic array ($\delta=0$) a scan blindness occurs around 45° for both cases. As was the case with the infinite planar array, the blindness is narrowed greatly as randomization is introduced but is not completely removed until the maximum amount of randomization ($\delta=.25\lambda$) is introduced.

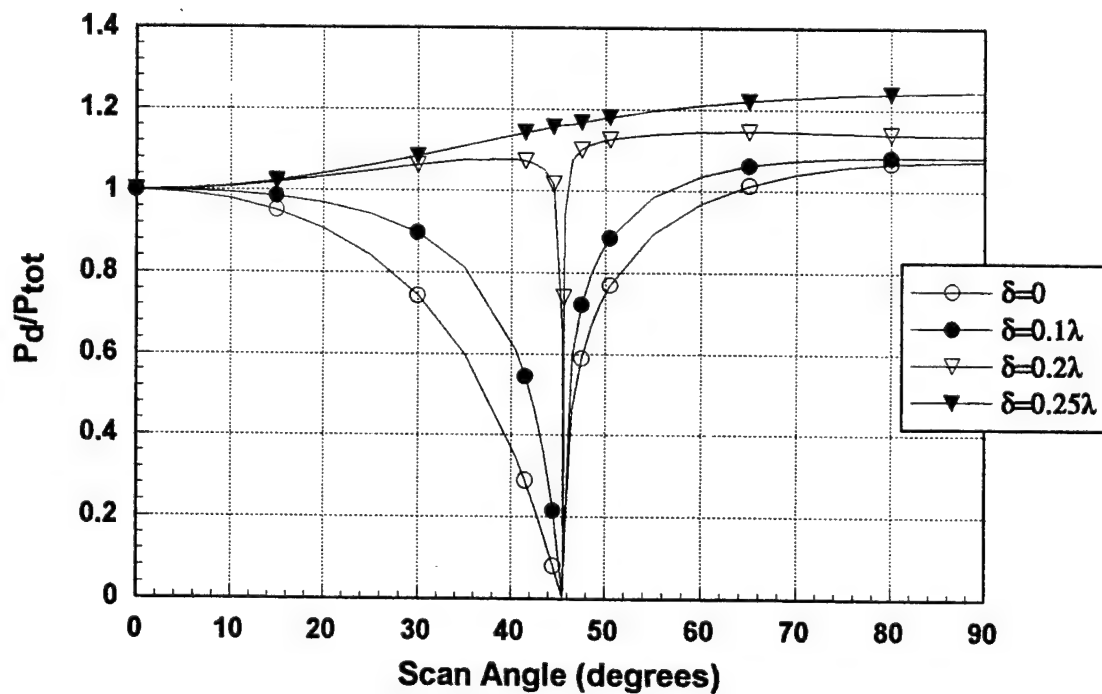
The surface wave efficiency for both examples is shown in Figures 1.8a and 1.8b. The infinite linear array differs from the planar array in that even in the periodic case a surface wave can be launched (the periodic planar array can support a surface wave only *exactly* at blindness). For scan angles that are greater than the blindness angle, a large amount of power is coupled into this surface wave, thereby lowering the efficiency. As the degree of randomization is increased, the efficiency decreases near broadside but increases for those angles which are greater than the blindness angle. Again, the average efficiency of the example with high relative permittivity has a markedly lower efficiency than the example of Figure 1.8a.

1.4 A Finite Linear Array Example

The ultimate goal of any infinite array analysis is to try to effectively model large finite arrays with the added bonus of increased computational efficiency. Therefore, a set of fixed parameters for a large finite linear array were chosen and several random arrays were analyzed to see if the solution for the infinite array does in fact model the behavior of the finite array. Also, looking at the input impedances of the individual elements in the finite random array gives a good idea of the variance of the input impedance, a calculation which is extremely complicated for the infinite array. The average surface wave efficiency for the finite arrays can also be examined. For this example, linear arrays consisting of 99 elements were considered with the other parameters as listed in Figure 1.8b.

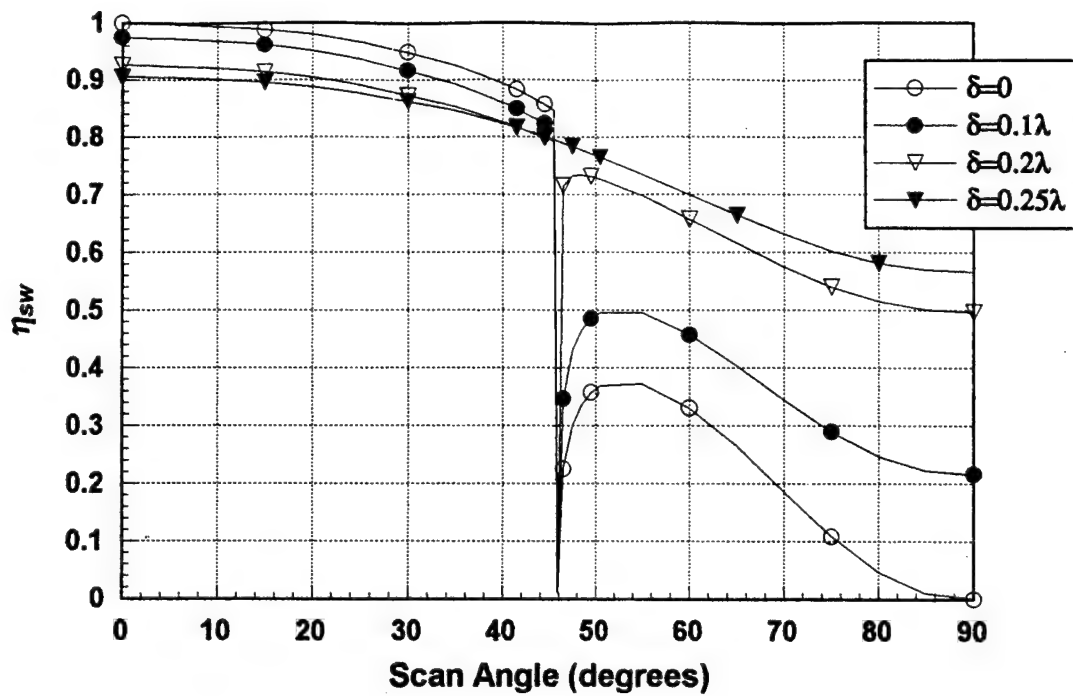


(a)

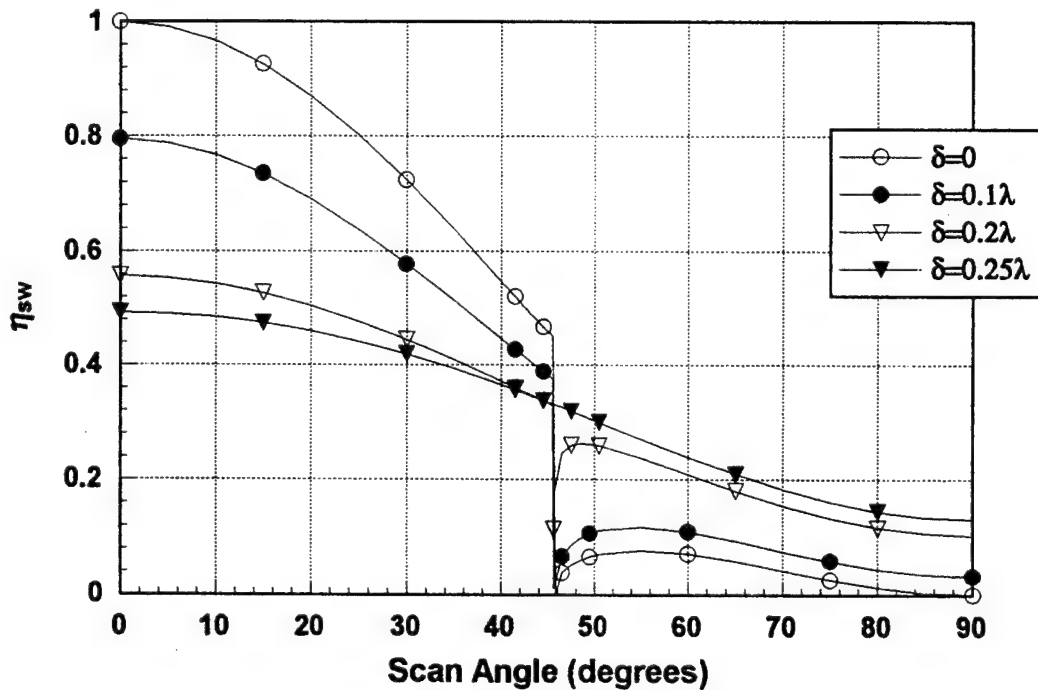


(b)

Figure 1.7. Ratio of average dipole (radiated & surface wave) power to total power supplied by source for an infinite E-plane linear array of printed dipoles. Values are normalized at broadside. (a) $a=0.5\lambda$, $L=0.39\lambda$, $w=0.01\lambda$, $d=0.19\lambda$, $\epsilon_r=2.55$. (b) $a=0.5\lambda$, $L=0.156\lambda$, $w=0.01\lambda$, $d=0.06\lambda$, $\epsilon_r=12.8$.



(a)



(b)

Figure 1.8. Surface wave efficiency for an infinite E-plane linear array of printed dipoles. (a) $a=0.5\lambda$, $L=0.39\lambda$, $w=0.01\lambda$, $d=0.19\lambda$, $\epsilon_r=2.55$. (b) $a=0.5\lambda$, $L=0.156\lambda$, $w=0.01\lambda$, $d=0.06\lambda$, $\epsilon_r=12.8$.

In order to provide data to compare to the infinite array solution, several random finite arrays were generated and the results from each were averaged. The element positions along the x axis are given by $x_m = ma + \Delta_m$, and for each element the value Δ_m was generated from a uniform random variable with zero mean defined on the interval $[-\delta, \delta]$. The result is a finite array with fixed, but non periodic, element positions.

For large degrees of randomization many arrays had to be analyzed to get a good average result due to the large variance in input impedance. For this purpose a full-wave moment method solution for the finite array, even using only a single mode on each dipole, is computationally impractical. Fortunately an asymptotic expression for the mutual impedance between elements exists [5] and data computed by this method can easily be curve fitted for the case of the linear E-plane array. For closely spaced elements the mutual impedance was computed using a spectral domain integration and also curve-fitted. With this approach solutions for several random finite arrays with a large number of elements can be computed rapidly with a great deal of accuracy.

The analysis proceeds similarly to that of the infinite random linear array with a fixed terminal current on each dipole. The input impedance for the n^{th} dipole is then computed as

$$Z_{in}^n = \frac{jZ_o}{4\pi^2 k_o} \sum_{m=1}^N e^{jk_o u(x_n - x_m)} \int_{-\infty}^{\infty} \int_{-\infty}^{\infty} Q_{xx}(k_x, k_y) F^2(k_x, k_y) e^{jk_x(x_m - x_n)} dk_x dk_y \quad (1-12)$$

where N is the number of elements and x_m is the position of the m^{th} element. The spectral integral in (1-12) is just the mutual impedance of two dipoles in the array (obviously the

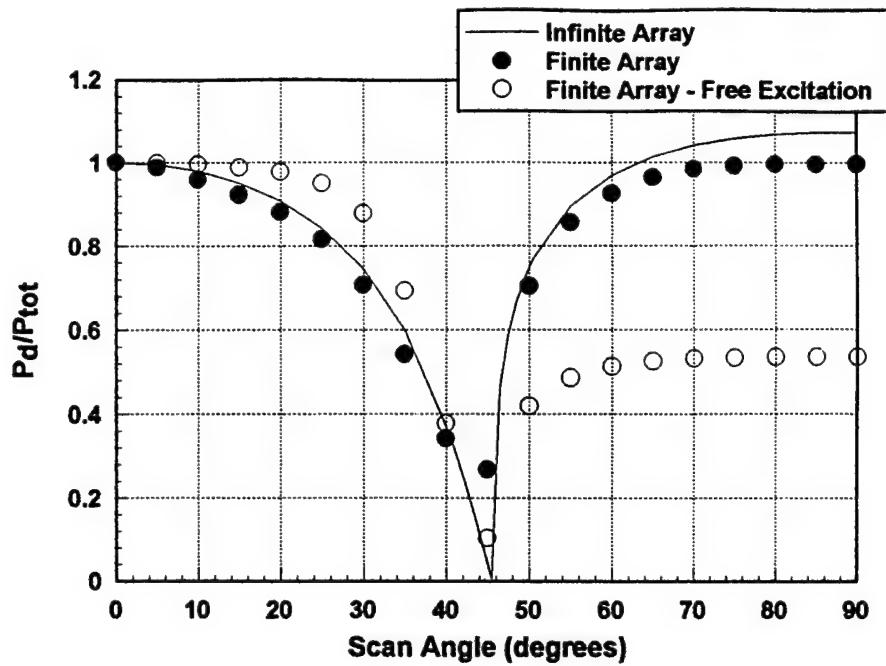
dipole self-impedance in the case where $m=n$) so the asymptotic data mentioned above may be used and the input impedance computed as

$$Z_{in}^n = \frac{jZ_o}{4\pi^2 k_o} \sum_{m=1}^N e^{jk_o u(x_n - x_m)} Z_{mut}(x_m - x_n) \quad (1-13)$$

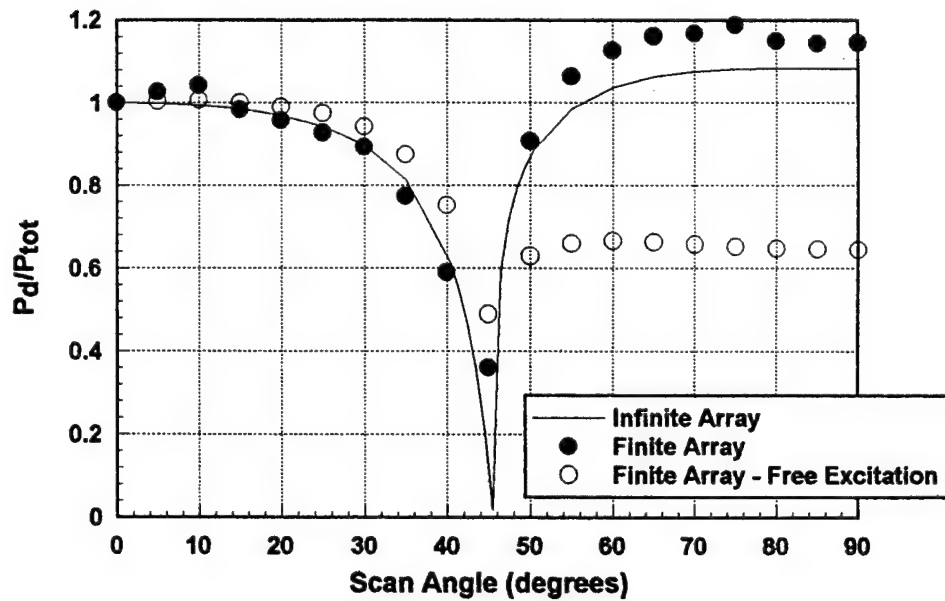
Plots comparing the ratio of average power dissipated by the dipole array to the total power supplied by the source for the finite and infinite cases are shown in Figures 1.9a,b,c,d for cases with $\delta=0$, $\delta=0.1\lambda$, $\delta=0.2\lambda$, and $\delta=0.25\lambda$ respectively. Twenty-five distinct finite arrays were used to generate the data. The agreement is quite good in all cases, and while a true blindness is not seen in the finite array, a dip in the power ratio is evident near the 45° scan angle except for the $\delta=0.25\lambda$ case. The case of free excitation for a finite array is also considered in Figure 1.9. It is seen that with varying randomization the blindness is reduced to a greater extent with free excitation than by using fixed terminal currents at each dipole. The results between the two cases are not significantly different, however.

The average value of input impedance for the finite and infinite arrays is compared in Figures 1.10a,b,c,d for cases with $\delta=0$, $\delta=0.1\lambda$, $\delta=0.2\lambda$, and $\delta=0.25\lambda$ respectively. Agreement is excellent, with slight deviations at the blindness angle due to the finite size of the array and possible errors in the curve fit used for the mutual impedance.

The calculation of surface wave efficiency for the finite arrays is much more involved than in the case of the infinite array. Because a curve fit was used to find the mutual impedance between elements, Z_{sw} cannot be computed and (1-10) cannot be used. However, the total radiated power can be computed by integrating the far-fields of the array, and the surface wave efficiency defined as

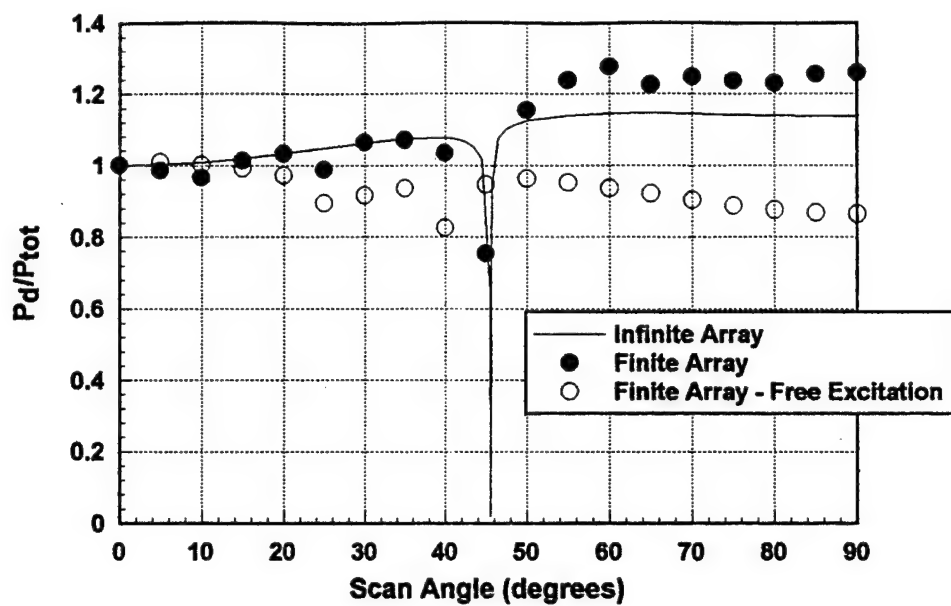


(a)

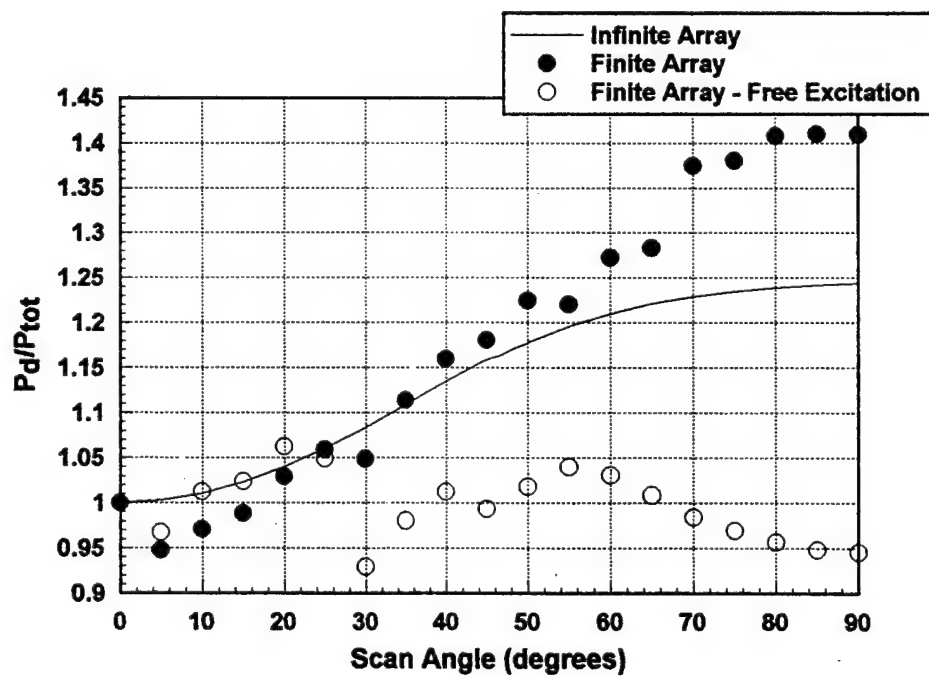


(b)

Figure 1.9. Ratio of average dipole (radiated & surface wave) power to total power supplied by source for 99 element finite linear array and infinite linear array. Values are normalized at broadside. $a=0.5\lambda$, $L=0.156\lambda$, $w=0.01\lambda$, $d=0.06\lambda$, $\epsilon_r=12.8$. (a) $\delta=0$ (b) $\delta=0.1\lambda$, (c) $\delta=0.2\lambda$, (d) $\delta=0.25\lambda$.



(c)



(d)

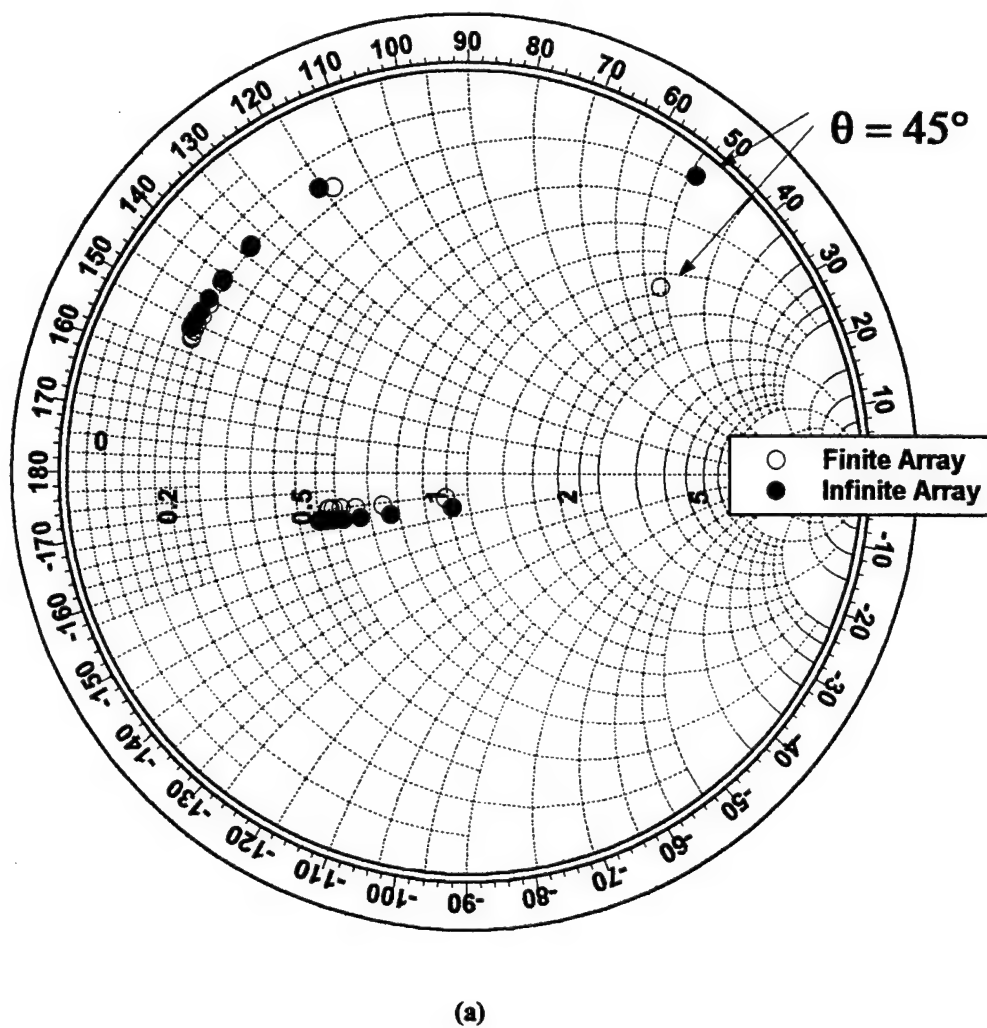
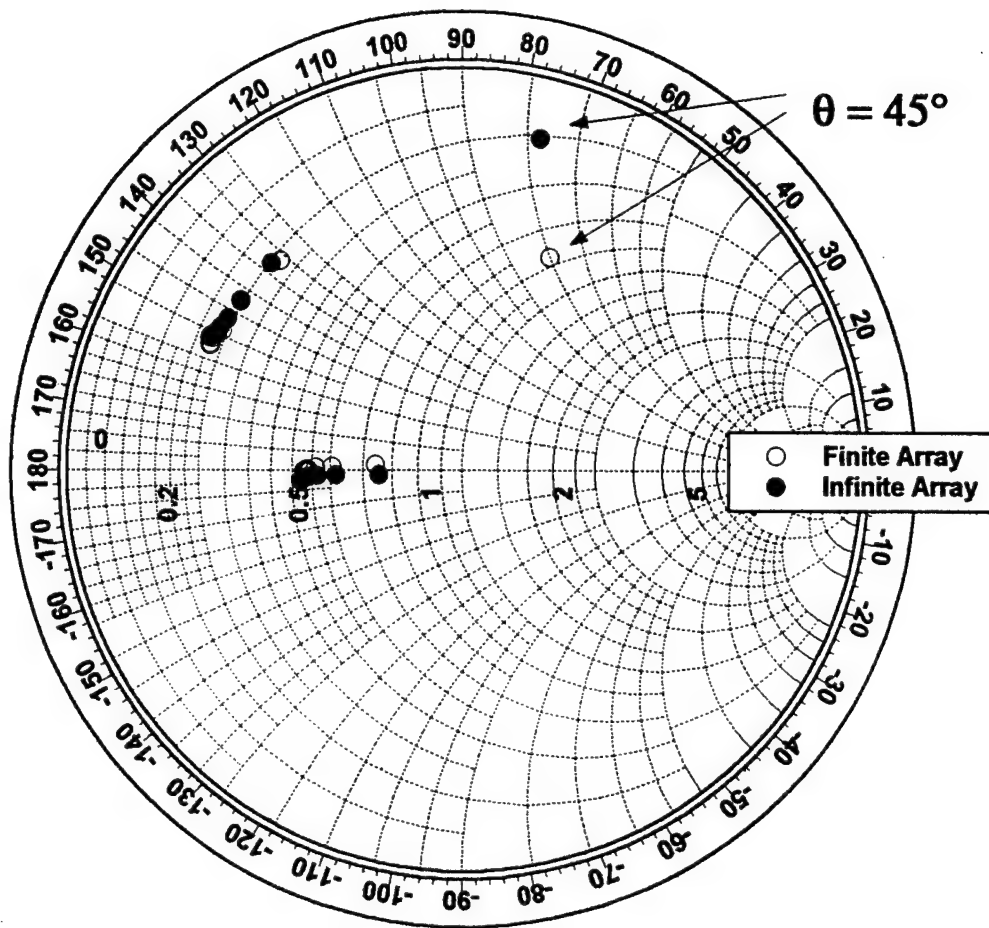
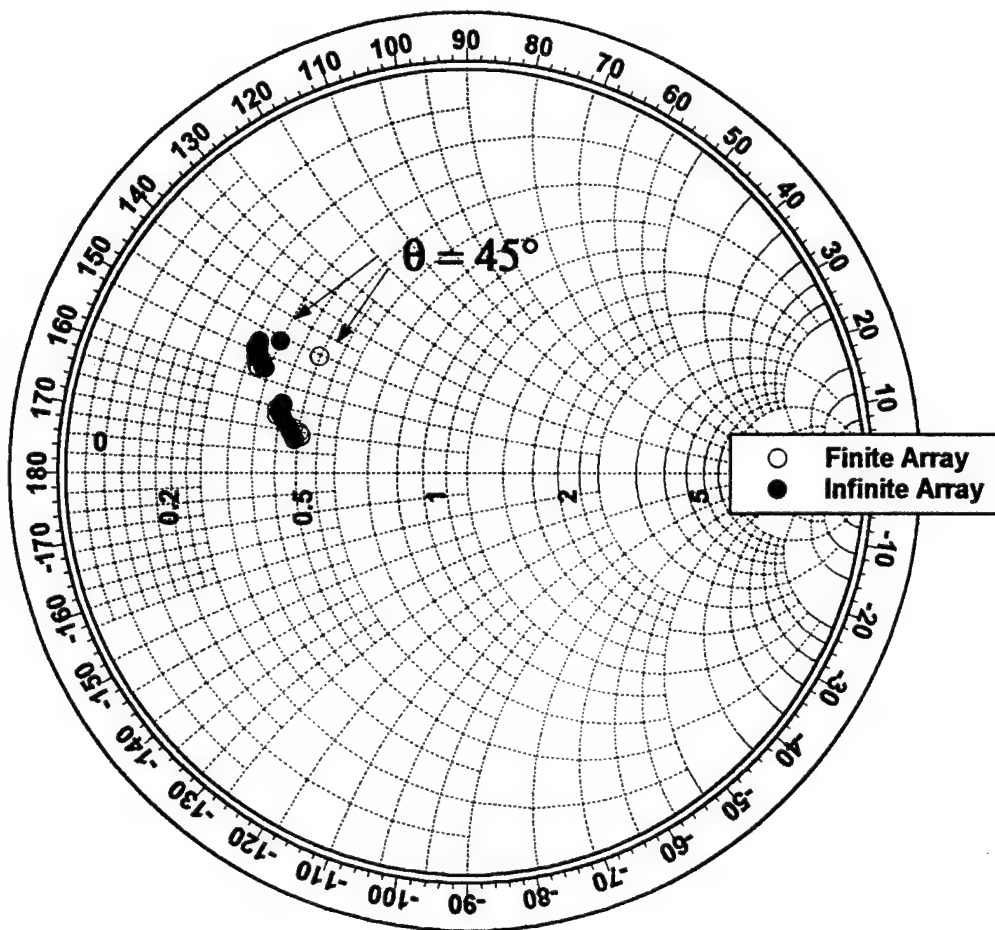


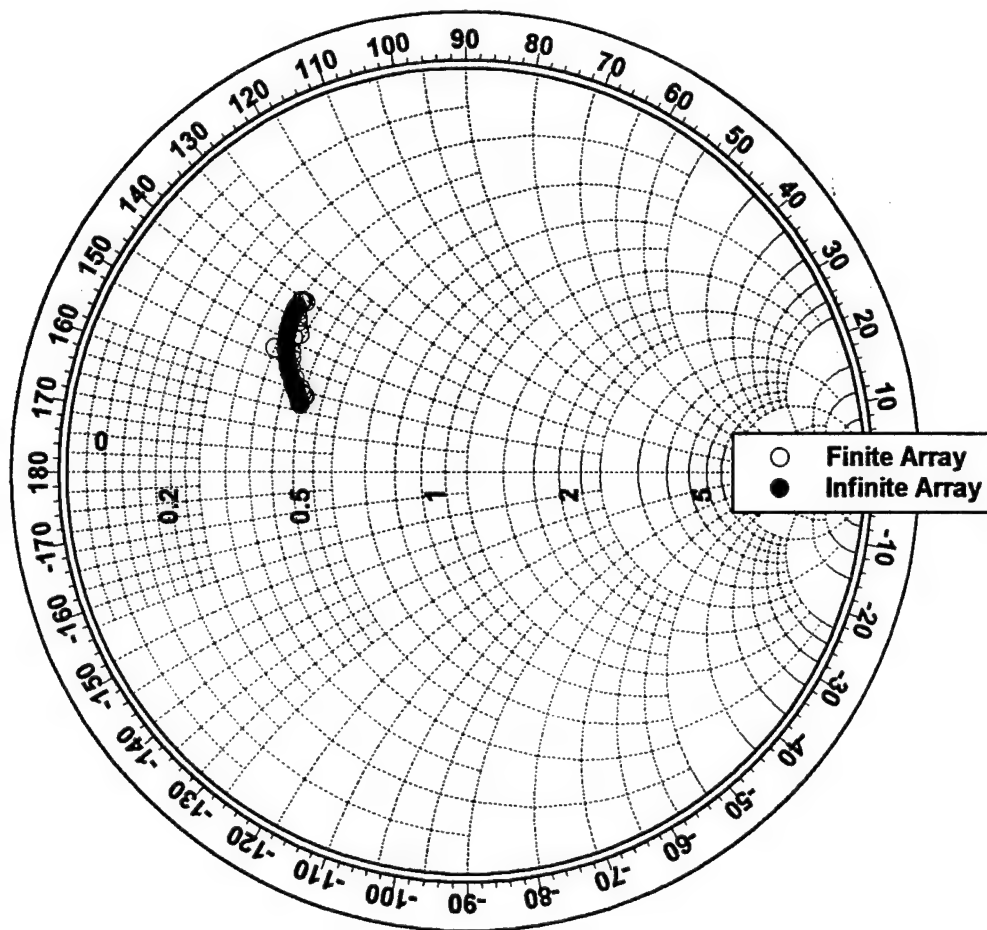
Figure 1.10. Plot of average input impedance for 99 element finite linear array and infinite linear array cases. Values are normalized to 50 ohms. $a=0.5\lambda$, $L=0.156\lambda$, $w=0.01\lambda$, $d=0.06\lambda$, $\epsilon_r=12.8$. (a) $\delta=0$ (b) $\delta=0.1\lambda$, (c) $\delta=0.2\lambda$, (d) $\delta=0.25\lambda$,



(b)



(c)



(d)

$$\eta_{sw} = \frac{P_{rad}}{\sum_{n=1}^N P_d^n} \quad (1-14)$$

where P_d^n is the power delivered to the n^{th} dipole as is given by (1-9b).

To find the radiated far field of the dipole array, a stationary phase evaluation of the Green's function is performed [6]. The far field of the n^{th} dipole with an x-directed current is given by

$$E_{\theta n} = -I_n \frac{e^{-jk_o r}}{r} \frac{Z_o}{2\pi} e^{jk_2 d} F(k_x, k_y) \left(\frac{k_o^2 \sin k_1 d}{T_e} \right) \cos \theta \sin \phi \quad (1-15a)$$

$$E_{\phi n} = I_n \frac{e^{-jk_o r}}{r} \frac{Z_o}{2\pi} e^{jk_2 d} F(k_x, k_y) \left(\frac{k_o k_1 \sin k_1 d}{T_m} \right) \cos \theta \cos \phi \quad (1-15b)$$

$$k_x = \sin \theta \cos \phi \quad ; \quad k_y = \sin \theta \sin \phi$$

where Z_o is the intrinsic impedance of free space and $I_n = e^{jk_o x_n \sin \theta}$ is the dipole terminal current. The expressions for k_1 , k_2 , T_e , and T_m are given in the Appendix.

The total radiated far field from the array is then given by

$$E_{\theta} = \sum_{n=1}^N E_{\theta n} e^{jk_o x_n \sin \theta \cos \phi} \quad (1-16a)$$

$$E_{\phi} = \sum_{n=1}^N E_{\phi n} e^{jk_0 x_n \sin \theta \cos \phi} \quad (1-16b)$$

The radiated power is then found by integrating the far fields,

$$P_{rad} = \frac{1}{Z_0} \int_0^{2\pi} \int_0^{\pi/2} (|E_{\theta}|^2 + |E_{\phi}|^2) \sin \theta d\theta d\phi \quad (1-17)$$

Plots comparing the average surface wave efficiency of the finite arrays to the surface wave efficiency of the infinite random linear array are shown in Figures 1.11a,b,c,d for cases with $\delta=0$, $\delta=0.1\lambda$, $\delta=0.2\lambda$, and $\delta=0.25\lambda$ respectively. To find the average surface wave efficiency, the surface wave efficiency of each individual finite array is computed using (1-14), and the results are averaged. The agreement in all cases is excellent, thereby validating the use of (1-10) in computing the surface wave efficiency for the infinite array and showing that the infinite array solution sufficiently models the behavior of the finite arrays.

To complete the analysis, the computed reflection coefficient for each dipole in the finite arrays was also calculated. The matching impedance, Z_b , used in the calculation was the expected value for the infinite array at broadside, and the dipoles were conjugate matched, i.e. $|\Gamma_n| = (Z_{in}^n - Z_b) / (Z_{in}^n + Z_b^*)$. While this calculation does not present any significant physical meaning, it does give some insight into the variance of the input impedance as the dipole positions are randomized.

Histograms showing the distribution of the magnitude of this reflection coefficient are shown for no randomization in Figures 1.12a&b, and for cases with $\delta=0.25\lambda$ in Figures 1.13a&b. In the periodic case the reflection coefficient is quite small for the great

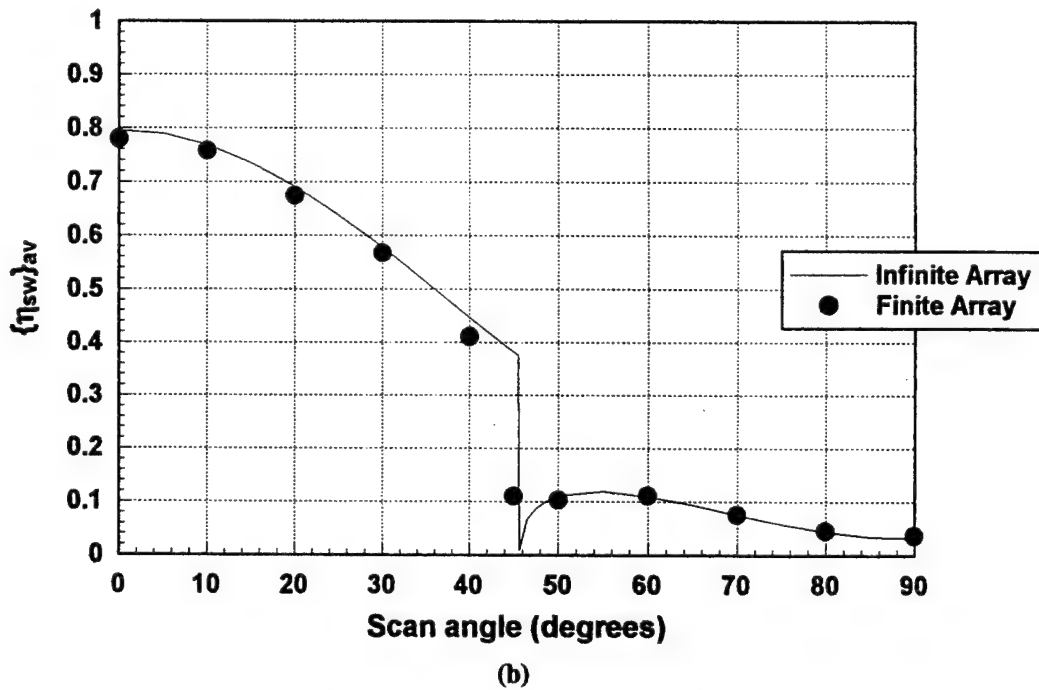
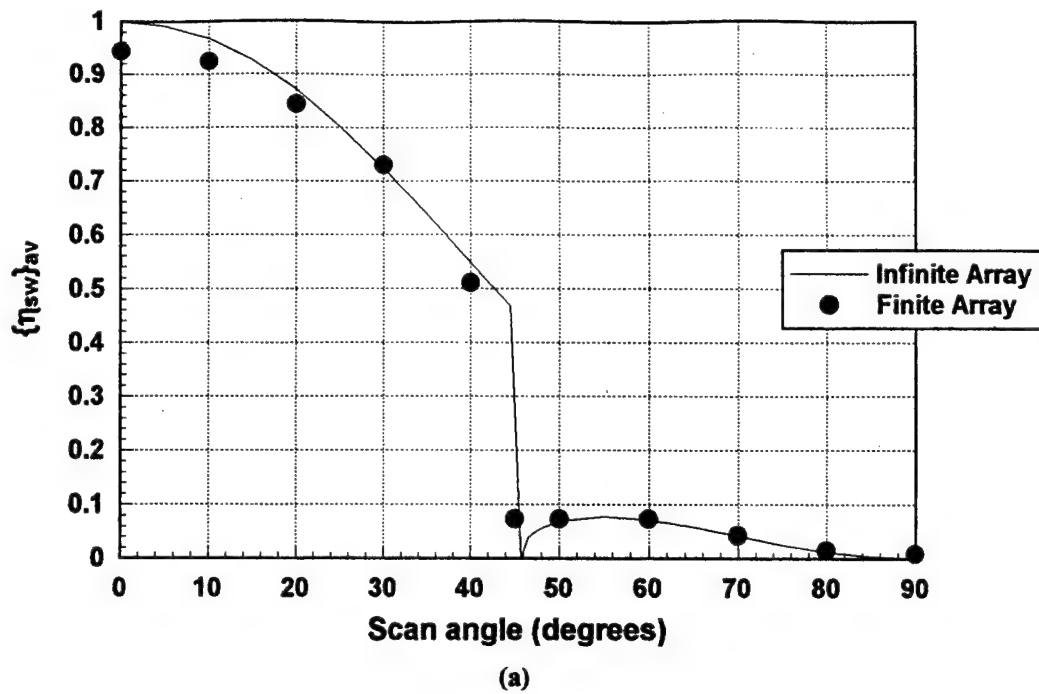
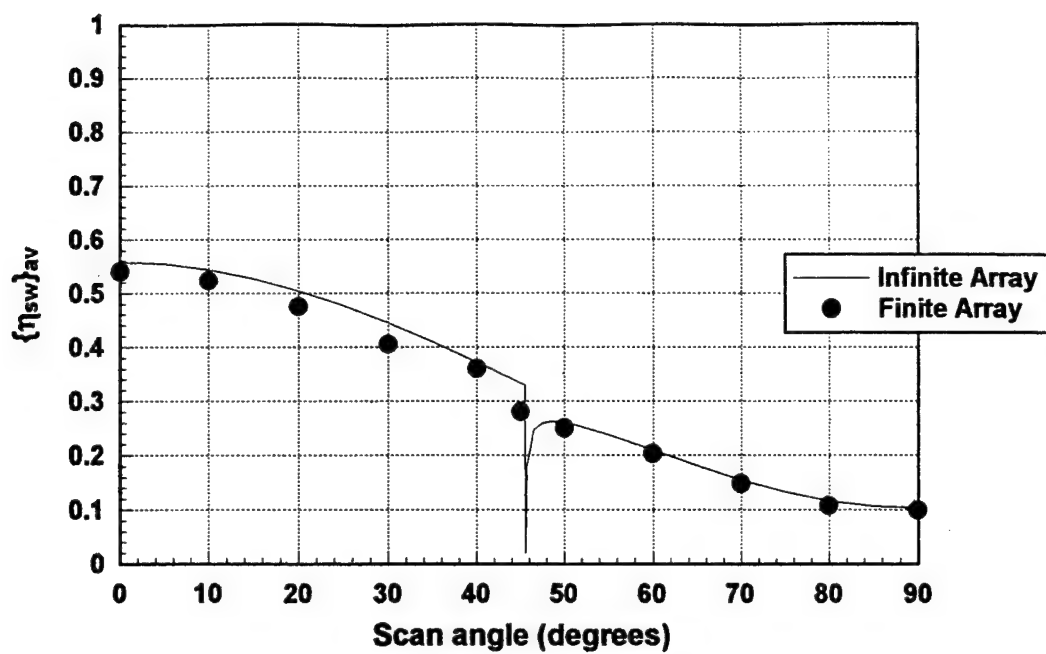
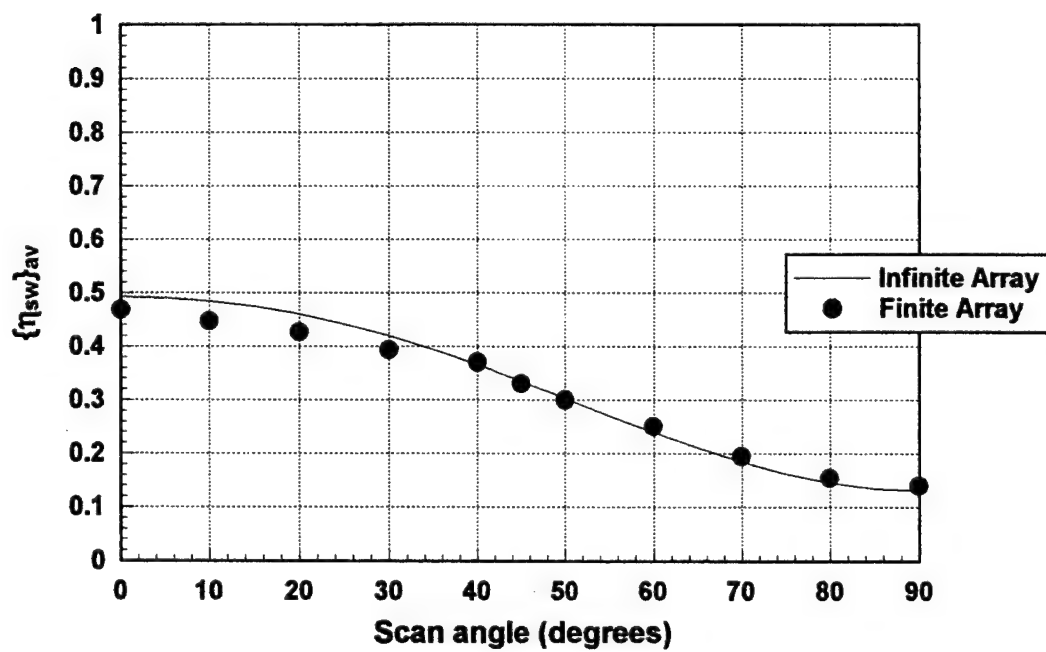


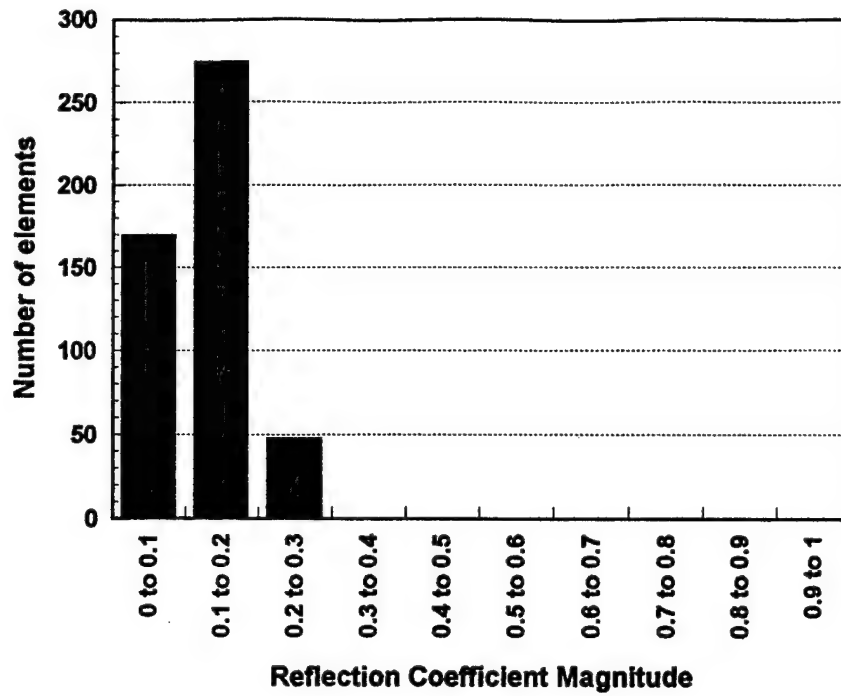
Figure 1.11. Average surface wave efficiency for 99 element finite linear arrays and infinite linear array. $a=0.5\lambda$, $L=0.156\lambda$, $w=0.01\lambda$, $d=0.06\lambda$, $\epsilon_r=12.8$. (a) $\delta=0$ (b) $\delta=0.1\lambda$, (c) $\delta=0.2\lambda$, (d) $\delta=0.25\lambda$



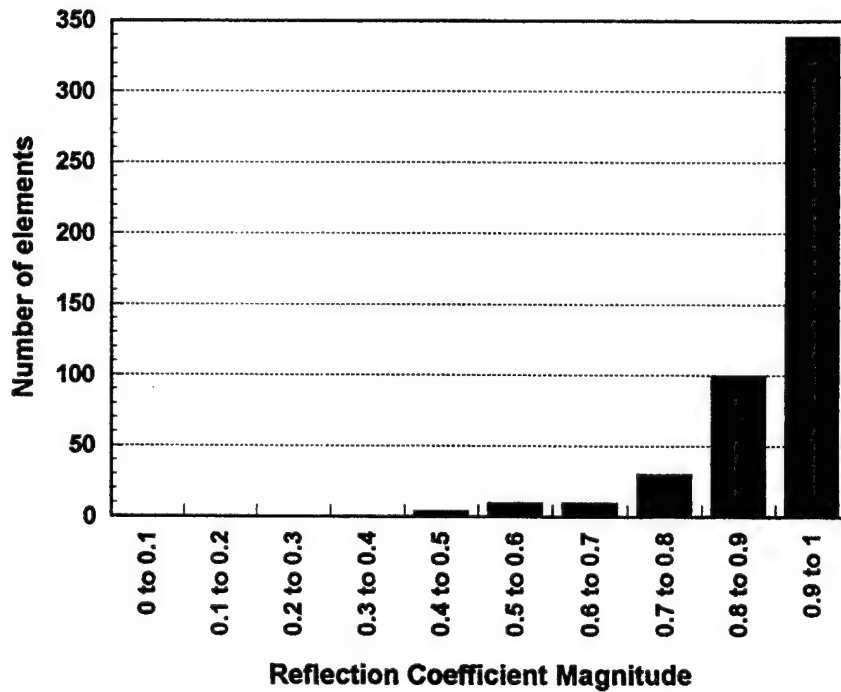
(c)



(d)

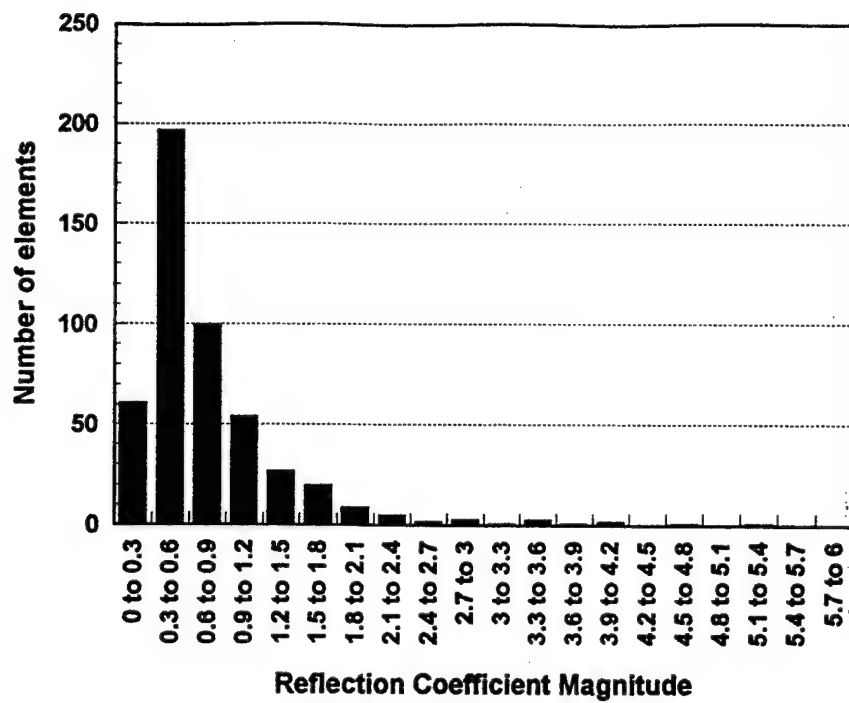


(a)

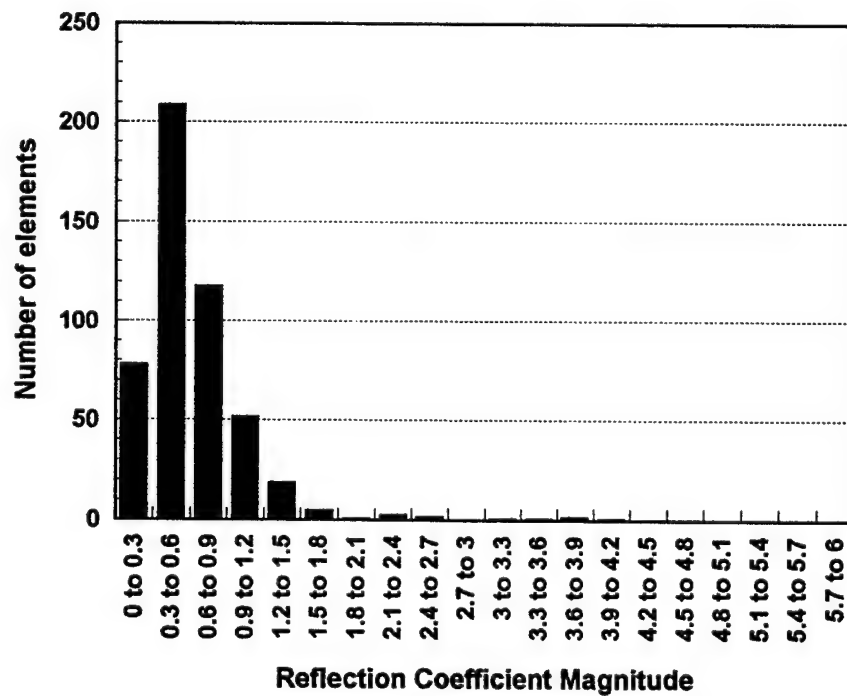


(b)

Figure 1.12. Distribution of reflection coefficient magnitude for periodic finite linear arrays. Five 99 element arrays considered. (a) Broadside. (b) 45 degree scan.



(a)



(b)

Figure 1.13. Distribution of reflection coefficient magnitude for finite linear arrays with $\delta=0.25\lambda$. Five 99 element arrays considered. (a) Broadside. (b) 45 degree scan.

majority of the dipoles, with elements near the edge exhibiting a slightly higher reflection coefficient magnitude. The case with $\delta=0.25\lambda$ is much more interesting. The majority of dipoles at broadside have reflection coefficient magnitudes in the 0.3 to 0.6 range, showing that the median and mean values for the input impedance are quite different. Also, there are a few elements exhibiting reflection coefficient magnitudes of greater than unity.

While this seems like an erroneous result at first glance, it can be explained by mutual coupling of power between the dipoles [7]. When the mutual coupling between elements is strong, a great deal of power can be delivered through this mutual coupling to some elements, and in some cases this coupled power exceeds the power supplied to the element by the feed. This results in a negative input resistance for the element and a greater than unity magnitude reflection coefficient. The total power balance for the array is preserved, however.

In this chapter the solution for the expected value of input impedance for an infinite array of printed dipoles was presented. Planar and linear E-plane arrays were considered. The scan blindness phenomenon was seen to be reduced with the introduction of randomization, and to disappear completely only when the full extent of randomization was introduced. Several large finite arrays with element positions generated from a uniform random variable were analyzed and averaged data from these arrays compared well with the infinite array calculation.

A limitation of the practicality of this analysis is the stipulation of a fixed terminal current at each dipole, which would be a difficult and cost prohibitive measure to implement in an array of printed dipoles. A fixed terminal current at each dipole reduces the effects of mutual coupling on the array pattern, however, which can be quite severe in

a random array. The alternative is the case of using free excitation for each dipole. This method, while being easily implemented, suffers greatly from mutual coupling effects in the random array environment.

These effects can be seen by examining the patterns shown in Figure 1.14. The patterns shown are for the cases of free excitation and fixed terminal current, and for both cases the element positions are the same. The effect of mutual coupling in the free excitation case is easily seen in the high sidelobes that are present in the radiation pattern, which is a major problem associated with randomly spaced arrays. For the case of fixed terminal currents, the sidelobes are of much lower intensity.

A conclusion of this work is that the method of using randomly spaced elements in an array of printed dipoles, while being a valid technique for eliminating scan blindnesses, is not very attractive in terms of performance and cost. A much more practical method is to make a proper choice of substrate in order to move any scan blindness effects near endfire.

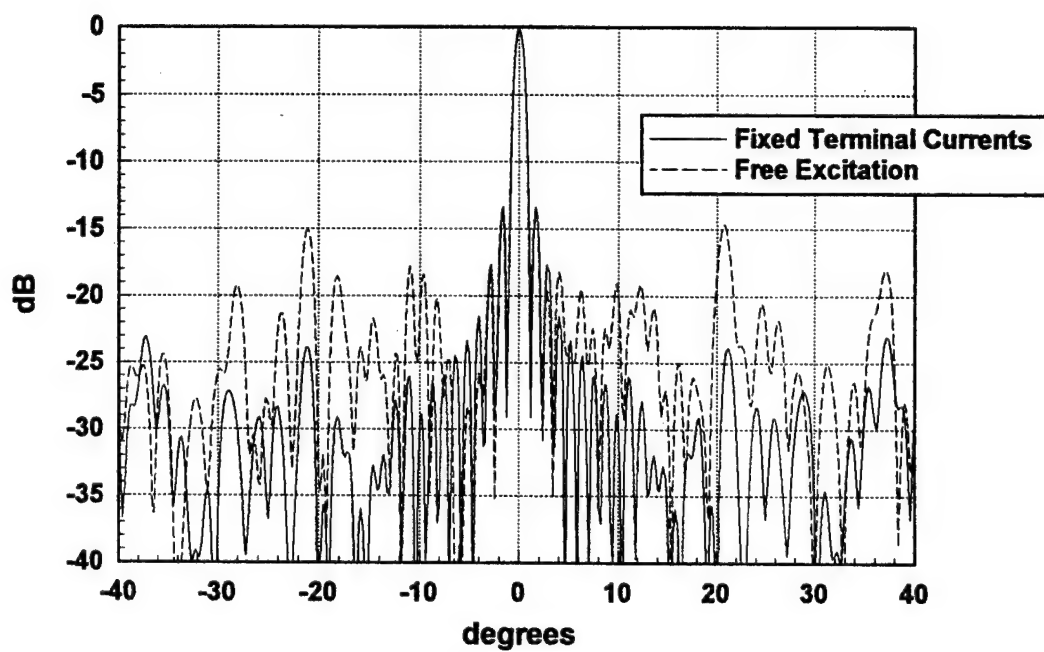


Figure 1.14. Radiation patterns for a 99 element E-plane linear array of printed dipoles with randomly spaced elements. Element positions were generated with $\delta=0.2\lambda$, $a=0.5\lambda$, $l=0.156\lambda$, $w=0.01\lambda$, $d=0.06\lambda$, $\epsilon_r=12.8$.

CHAPTER 2

ANALYSIS AND DESIGN OF MICROSTRIP REFLECTARRAYS USING PATCHES OF VARIABLE SIZE

2.1 Introduction

In a great number of microwave applications a highly directive antenna with a main beam scanned to a certain angle is required. Two types of antennas that do this are reflectors and arrays. The reflector antenna uses its geometry to create the desired phase across the aperture, while an array antenna employs distinct elements fed with progressive phasing. Reflector antennas are advantageous in that they typically exhibit large bandwidth and low loss; the main disadvantage of the reflector is the geometrical constraint it imposes on the design. The most widely used reflector, the parabolic reflector, also produces a cross polarized field which is inherent in its geometry. Microstrip patch arrays are lightweight, low-profile antennas that are capable of low cross polarization levels but typically have small bandwidth and fairly large loss at microwave frequencies.

Obviously, cases arise where it would be beneficial to combine some of the more attractive features of reflectors and arrays. This is accomplished by the reflectarray [8]. Reflectarrays are illuminated by a feed antenna which excites an array of radiating elements comprising a reflecting surface, and these elements produce a scattered field. Many types of reflectarrays, the microstrip reflectarray included, also produce a specularly reflected field component as in the case of a geometric reflector. The total field then consists of the scattered field and any specular reflection. The array elements can be tuned to produce the required phasing over the aperture, thereby eliminating the

geometrical constraint of ordinary reflectors. Also, the radiating elements are typically tuned so that the radiated field reacts favorably with any specularly reflected field.

Early reflectarray designs employed arrays of dipoles, spirals, and waveguides [8], [9], [10]. By using microstrip elements in the reflectarray, one gains all of the advantages of microstrip, and with this reasoning a microstrip reflectarray using circular elements was proposed in 1978 by Malagisi [11]. More work on microstrip reflectarrays with circular elements, including a treatment of scattering from infinite arrays, was performed by Montgomery [12].

In [13], a microstrip reflectarray was designed using patches with an attached microstrip line stub for phasing as radiating elements. In [14], it was shown that the same type of phase control could be achieved by using patches of variable resonant length, without tuning stubs. This technique eliminates the need for a triangular grid spacing to accommodate the stubs, and produces a slightly larger bandwidth since the bandwidth of the stubs is no longer a factor.

In this chapter the steps taken in the design of a microstrip reflectarray using patches of variable size will be outlined. The design procedure will be similar to that of [13], using the moment method solution for plane wave scattering from an infinite array of microstrip patches as a building block on which to design the electrically large, albeit finite sized, reflectarray. At each unit cell in the reflectarray, reflection phase data computed from the solution of plane wave scattering from infinite array of uniformly sized patches is used to pick a patch length, and then a patch of the required length is placed in the corresponding unit cell of the reflectarray. This results in a large array of elements, each with a slightly different resonant length. Each unit cell in the reflectarray is then assumed to radiate with the same characteristics as if it was in the infinite array environment.

Several topics in the analysis and design of microstrip reflectarrays which were not treated in [13] are discussed in this chapter, specifically:

- Computational efficiency issues for the moment method analysis, with a marked increase in resulting efficiency .
- The effect of including both TE and TM polarized field components in describing the incident field, including the generation of a cross polarized field similar to that produced by a parabolic reflector.
- The effect of using an offset feed to reduce beam squint with frequency.
- A detailed analysis of dielectric and conductor losses.
- An involved discussion on potential sources of phase error that can degrade the performance of the reflectarray.
- The design, manufacture, and test of several millimeter wave microstrip reflectarrays to see if the concept is feasible at these frequencies.

2.2 The Moment Method Solution of Plane Wave Scattering From an Infinite Array of Microstrip Patches

The moment method solution for plane wave scattering from an infinite array of stub tuned patches is described in great detail in [13]. For that problem, piecewise sinusoidal (PWS) modes were used in the analysis. These modes were needed due to the

irregular shape of the stub tuned patch. In [14], a similar solution is performed on patches of varying length, however, due to the simple rectangular shape of the patches, entire domain modes were used. This speeds up the analysis since fewer modes are needed.

In both cases the results from the moment method solution are employed in designing a finite reflectarray. It should be noted that both of these methods achieve essentially the same effect; the relative phase of the total far field as the patch is operated off resonance is tailored to produce a collimated beam. In [13], a variable length stub on a fixed size patch shifts the resonant frequency; in [14] a variable length patch produces the same result.

The geometry of the infinite array problem is shown in Figure 2.1. A patch of length l and width w resides in a unit cell of dimensions a and b in the x and y direction, respectively. The patches reside a distance d above a ground plane, separated by a dielectric substrate with relative permittivity ϵ_r . A triangular grid is used for the first design example in Chapter 3, however, the rectangular grid is used for all other examples and presented results.

A brief outline of the moment method solution described in [14] is now presented. The incident field is a plane wave of the form

$$\vec{E}^{inc} = \vec{E}_0 e^{jk_0(xu_0 + yv_0 + z \cos \theta_0)} \quad (2-1)$$

In general, the incident field contains a TM component (θ polarized) and a TE component (ϕ polarized). Since the reflecting surface is infinite, we can also describe the specularly reflected and scattered fields as plane waves. The specularly reflected and scattered fields are given by

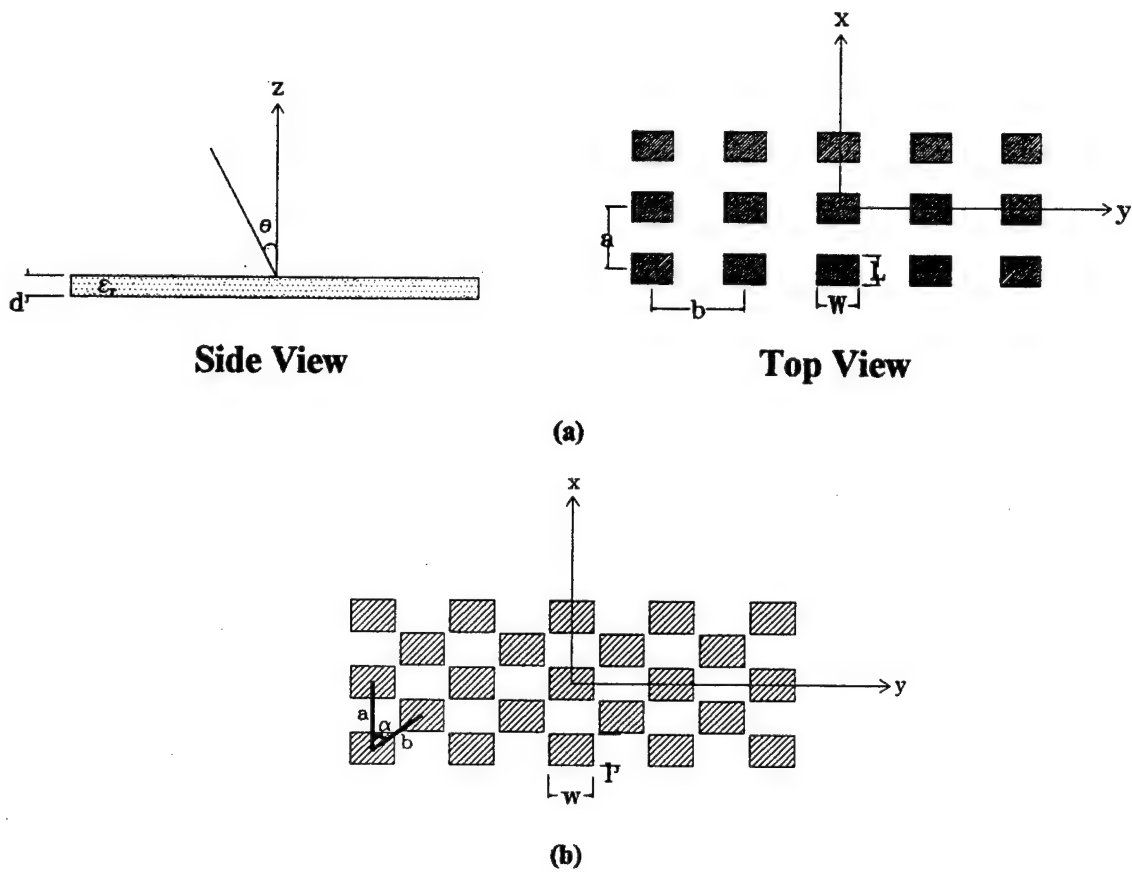


Figure 2.1. Geometry of the infinite array scattering problem. (a) Rectangular array grid. (b) Triangular array grid.

$$\bar{E}^{ref} = \bar{\bar{R}} \cdot \bar{E}_o e^{jk_o(xu_o + yv_o - z \cos \theta_o)} \quad (2-2)$$

$$\bar{E}^{scat} = \bar{\bar{S}} \cdot \bar{E}_o e^{jk_o(xu_o + yv_o - z \cos \theta_o)} \quad (2-3)$$

$$u_o = \sin \theta_o \cos \phi_o \quad v_o = \sin \theta_o \sin \phi_o$$

where

$$\bar{\bar{R}} = \begin{bmatrix} R_{\theta\theta} & 0 \\ 0 & R_{\phi\phi} \end{bmatrix} \quad \bar{\bar{S}} = \begin{bmatrix} S_{\theta\theta} & S_{\theta\phi} \\ S_{\phi\theta} & S_{\phi\phi} \end{bmatrix} \quad (2-4)$$

The total field is then the vector sum of the specularly reflected and scattered fields. The specular reflection matrix can be computed easily through a transmission line analogy, and the scattering matrix is computed using the moment method solution. The patch current is expanded in a set of N basis functions,

$$\bar{J}(x, y) = \sum_{i=1}^N I_i \bar{J}_i(x, y) \quad (2-5)$$

where the I_i are the unknown coefficients of each mode, and each expansion mode has a Fourier Transform $\bar{F}_i(k_x, k_y)$. The unknown coefficients can then be found as

$$\bar{I} = \bar{\bar{Z}}^{-1} \cdot \bar{V} \quad (2-6)$$

where

$$Z_{ij} = -\frac{1}{ab} \sum_{m=-\infty}^{\infty} \sum_{n=-\infty}^{\infty} \bar{F}_i \cdot \bar{G} \cdot \bar{F}_j \quad (2-7a)$$

for the rectangular grid, and, for the triangular grid [13]

$$Z_{ij} = -\frac{1}{ab \sin \alpha} \sum_{m=-\infty}^{\infty} \sum_{n=-\infty}^{\infty} \bar{F}_i^* \cdot \bar{\bar{G}} \cdot \bar{F}_j \quad (2-7b)$$

Also,

$$V_i = \iint_S \bar{J}_i \cdot (\bar{E}^{inc} + \bar{E}^{ref}) ds \quad (2-8)$$

In equations (2-7a) and (2-7b), $\bar{\bar{G}}$ is the dyadic Green's function for an electric current source on a dielectric substrate [13], and in (2-8) the area of integration S is the area of the patch.

The summations in (2-7a) are over the Floquet modes defined as

$$k_x = k_o u_o + \frac{2\pi m}{a} \quad (2-9a)$$

$$k_y = k_o v_o + \frac{2\pi n}{b} \quad (2-9b)$$

while in (2-7b), (2-9b) becomes

$$k_y = k_o v_o + \frac{2\pi n}{b \sin \alpha} - \frac{2\pi m}{a \tan \alpha} \quad (2-9c)$$

2.2.1 An Efficient Mode Set for the Plane Wave Scattering Problem

In the computer program that implements the moment method solution most of the CPU time required is in computing the impedance matrix elements of (2-7), since the expression for each matrix element is not in closed form, but in the form of an infinite sum. Therefore, choosing a set of basis functions which provides convergence with a minimum number of modes is essential for obtaining good computational efficiency.

The set of basis functions used in [14] is a set of entire domain sine modes,

$$f_s^m(x) = \begin{cases} \sin \frac{m\pi}{l}(x + l/2), & \text{for } |x| < l/2 \\ 0 & \text{for } |x| > l/2 \end{cases} \quad (2-10)$$

with Fourier Transforms given by

$$F_s^m(k_x) = \frac{2m\pi}{l} \frac{\cos k_x l/2}{\left(\frac{m\pi}{l}\right)^2 - k_x^2} \quad (2-11)$$

where l is the mode length.

For the plane wave scattering problem, odd modes (those with an even numbered index) make a negligible contribution for incidence angles of less than 60° . Therefore, in all calculations presented here, only even modes will be used. Even using just these modes, a large number are needed for convergence of the moment method problem.

A plot of computed reflection phase versus number of entire domain modes used is shown in Figure 2.2. It is evident from this plot that convergence of the phase does not occur until over 100 modes are used, resulting in a huge impedance matrix, and long computation times. This is due to the fact that the computed resonant frequency of the patch changes slightly as more modes are used. For very narrowband patches, such as the one in this example, a slight shift in resonant frequency produces a large shift in reflection phase. For patches that exhibit wider bandwidth, the reflection phase is not as dependent on resonant frequency, and the moment method solution converges with fewer modes. However, more than twenty modes are needed for almost all cases, and the matrix fill time is significant.

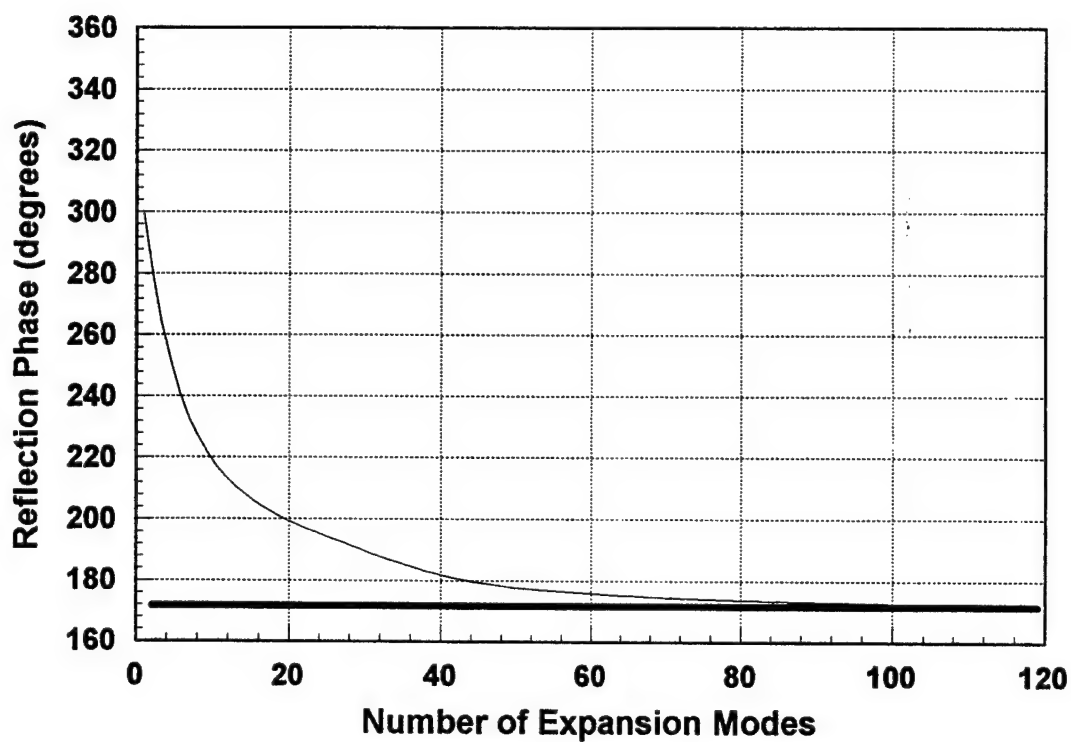


Figure 2.2. Computed reflection phase of infinite array of microstrip patches versus number of entire domain expansion modes. Thick line is reflection phase computed with one entire domain mode and one edge condition mode. $f=27.3$ GHz, $a=.6087$ cm, $b=.6667$ cm, $\epsilon_r=2.95$, $d=.0254$ cm, $\tan \delta=.0074$, $l=.3$ cm, $w=.3$ cm, $\theta=0^\circ$, $\phi=0^\circ$.

In order to find a more efficient mode set for this problem, the current vector of (2-6) was examined. For many different test cases, it was found that the current coefficients were all in phase and their magnitude dropped off asymptotically, with increasing index. A plot of the magnitude of the current coefficients is shown in Figure 2.3. The logarithmic graph shows a linear dependence for $n \geq 2$ modes, suggesting that the magnitude drops off as n^s , where $s = -1.5$ is the slope of the line.

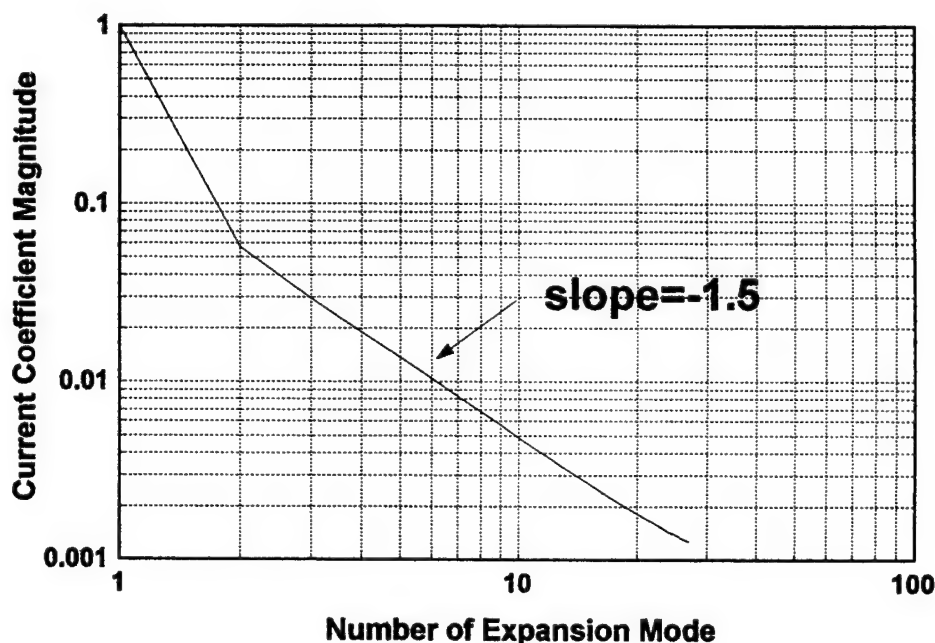


Figure 2.3. Computed magnitude of current coefficients of entire domain expansion modes for the moment method solution of an infinite array of microstrip patches versus mode number. $f=27.3$ GHz, $a=.6087$ cm, $b=.6667$ cm, $\epsilon_r=2.95$, $d=.0254$ cm, $\tan \delta=.0074$, $l=.3$ cm, $w=.3$ cm, $\theta=0^\circ$, $\phi=0^\circ$.

Since only even entire domain modes are used, the current coefficients are akin to the coefficients of a Fourier cosine series. A suitable expansion mode whose Fourier cosine series coefficients exhibit the same asymptotic behavior shown in Figure 2.3 is the edge condition mode [15] given by

$$J_e(x, y) = \frac{1}{a} \sqrt{a^2 - x^2} \quad (2-12a)$$

with Fourier transform

$$F_e(k_x) = \frac{\pi}{k_x} J_1(k_x a) \quad (2-12b)$$

where $J_1(x)$ is the Bessel function of the first kind with order one. The large argument formula for this Bessel function is

$$J_1(x) \approx \sqrt{\frac{2}{\pi x}} \cos\left(x - \frac{3\pi}{4}\right) \quad (2-13)$$

Substitution of (2-13) into (2-12b) reveals the asymptotic behavior of Figure 2.3.

By using this edge condition mode, only two expansion modes are needed for convergence of the moment method solution - the first mode in the entire domain expansion of (2-10) and the edge condition mode of (2-12). The computed reflection phase using these two modes for the case in Figure 2.3 was 171.5 degrees, the same value arrived at with the entire domain expansion, but using over one hundred fewer modes. Adding more modes along with the edge condition mode does not change the value of the reflection phase, showing that the solution has indeed converged.

2.2.2 Increasing the Computational Efficiency of the Floquet Mode Summation

The infinite sums of (2-7) are computed numerically, therefore, a limit must be set by which to truncate the series. In [1] a range of $-60 \leq m \leq 60$, $-60 \leq n \leq 60$ provided sufficient convergence, and that range also provides sufficient convergence for most cases in the present case. This gives a summation over the square region of the k_x, k_y plane as shown in Figure 2.4a.

Such a wide region is not needed for convergence, however. Because the infinite array assumption provides a summation over discrete Floquet modes instead of an integration over a continuous spectrum, performing the calculation over an irregularly shaped region is easily implemented - only a single FORTRAN program line was needed to define the region shown in Figure 2.4b. For a single element or finite array, where an integration in polar coordinates is performed, the technique is still valid but the implementation is much more complex.

To find a suitable region to sum over, the magnitude of the quantity inside the summation of (2-7) was examined. Areas inside the region depicted in Figure 2.4a where the magnitude is sufficiently small can be neglected in the summation, as their contribution to the final sum is negligible. A contour plot of this quantity is shown in Figure 2.5. Parameters for a typical case were used to construct the plot, and the patches are near resonance. Entire domain cosine modes were used as the expansion and testing modes, however, using the edge mode of (2-12a) produces similar results. From this plot it is readily seen that the summation of the Floquet modes only needs to be performed over a hyperbolic region as shown in Figure 2.4b. This region is defined by the equation

$$abs(m^2 n) \leq a \quad (2-14)$$

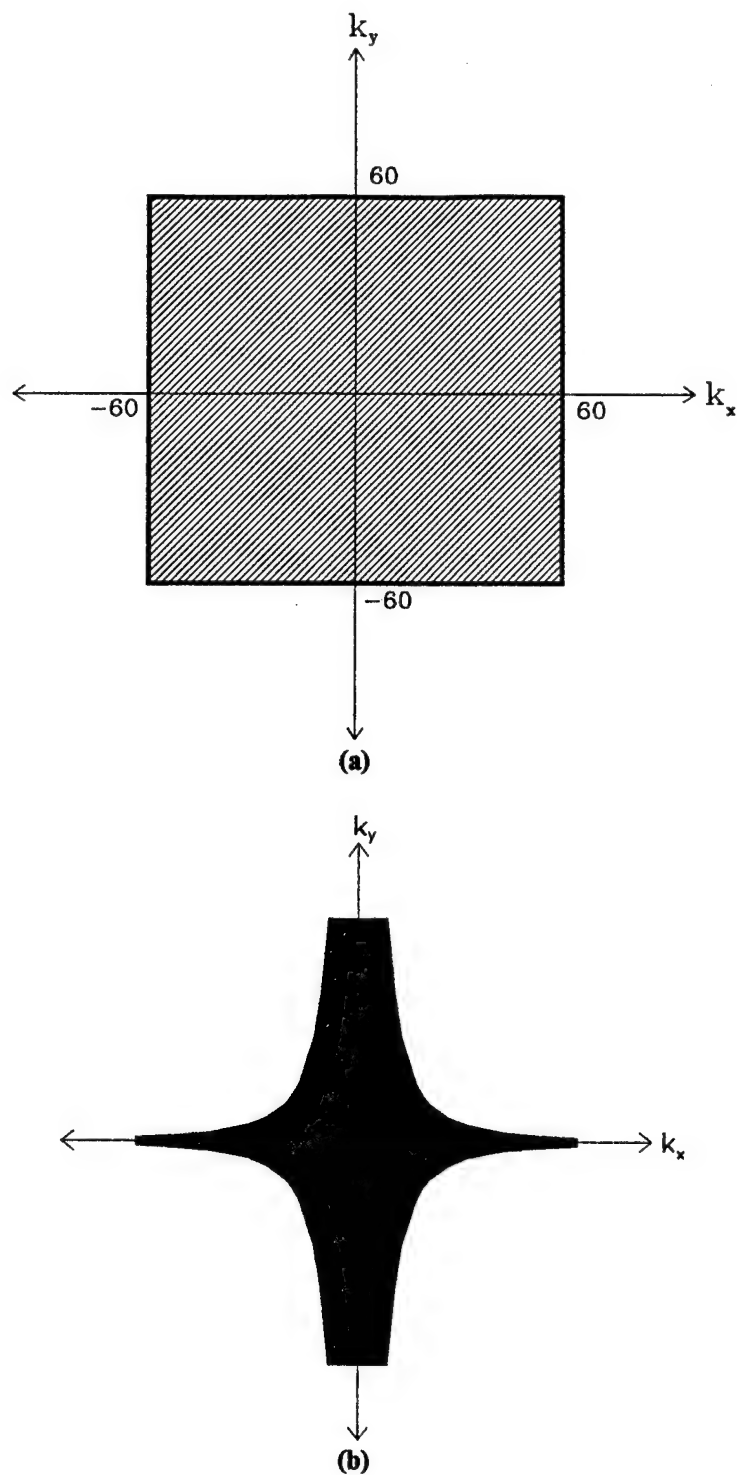
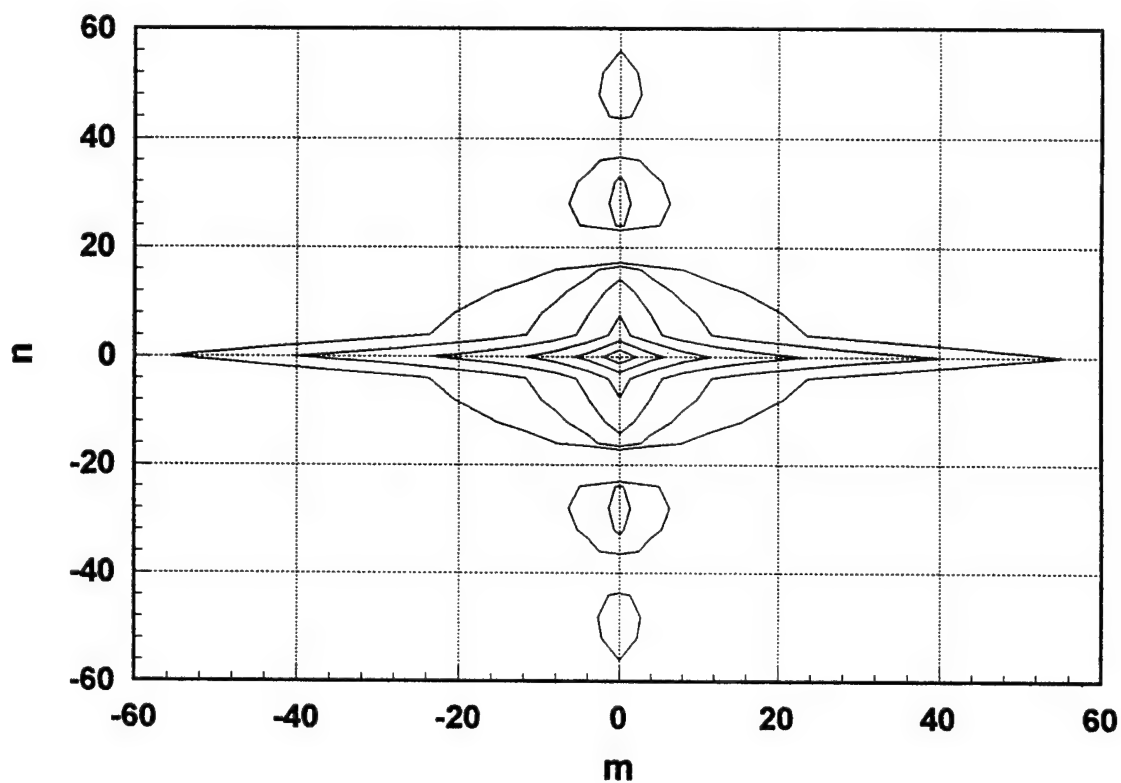


Figure 2.4 Area of summation of Floquet modes in the spectral domain. Indices shown are m,n .
 (a) Square region. (b) Hyperbolic region.



Logarithmic Scale
Contours -50, -40, -30, -20, -10, 0 dB

Figure 2.5. Contour plot of magnitude of $i=1, j=1$ impedance matrix element versus m, n .
 $f=27.3$ GHz, $a=.6087$ cm, $b=.6667$ cm, $\epsilon_r=2.95$, $d=.0254$ cm, $\tan \delta=.0074$, $l=.3$ cm,
 $w=.3$ cm, $\theta=0^\circ$, $\phi=0^\circ$.

where α is a constant. A value of 4000 provides excellent convergence while resulting in a 4 to 1 savings in CPU time needed to compute each impedance matrix element. In order to validate that the region is large enough to ensure convergence of the summation, several curves of reflection phase versus element length were computed using the parameters given in Figure 2.5. The results are shown in Figure 2.6. It is seen that the hyperbolic region is indeed large enough for convergence.

The hyperbolic region is valid for most practical cases, and it also appears to be valid for any moment method solution involving microstrip patches where entire domain modes are used. However, the extents of the region vary with some of the parameters used. This is due to the fact that the region is formed mostly by the shape of the Fourier transforms of the expansion and testing functions. Entire domain modes with higher indices will increase the size of the region, as will the use of very small patch dimensions since both of these factors have the effect of "widening" the respective Fourier transforms.

For the problem of plane wave scattering, however, the phase response is dominated by the specular reflection when the patch dimensions are small. Also, as was shown in the previous section, entire domain expansion modes with indices higher than one are not needed for convergence of the moment method solution, and the behavior of the edge mode of (2-12a) is very similar to that shown in this section. Therefore we can use the same hyperbolic region for all patch lengths with a great deal of accuracy.

2.3 Effect of Using TE and TM Incident Field Components

For the reflectarray design process described in [13], the incident field at each unit cell is locally approximated by a TM polarized plane wave incident at angle $(\theta, \phi) =$

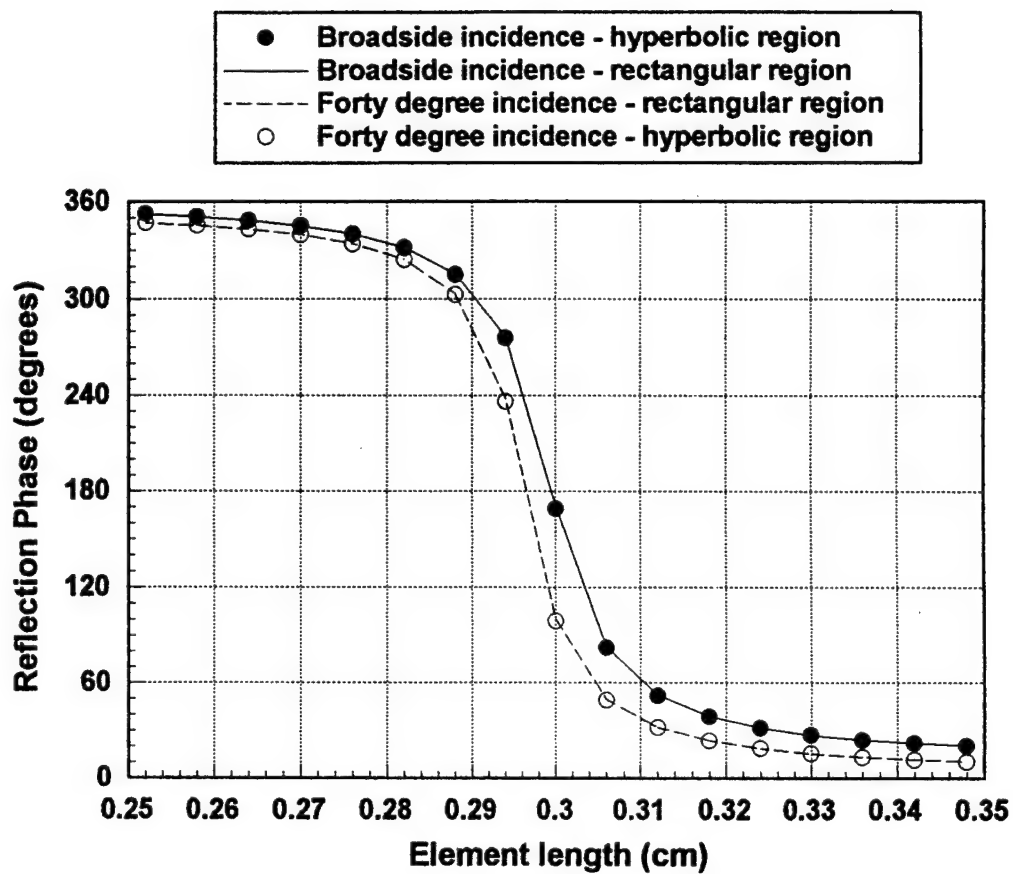


Figure 2.6. Computed reflection coefficient phase versus element length using Floquet mode summation over rectangular and hyperbolic regions. $f=27.3$ GHz, $a=.6087$ cm, $b=.6667$ cm, $\epsilon_r=2.95$, $d=.0254$ cm, $\tan \delta=.0074$, $l=.3$ cm, $w=.3$ cm, $\theta=0^\circ$, $\phi=0^\circ$.

$(\theta_i, 0)$. This gives a x-polarized tangential field across the dielectric-free space boundary, and also reduces the complexity of the scattering problem since for this case only a TM polarized scattered field will result. The pattern function is then generated by

$$F(\theta, \phi) = \sum_{i=1}^N E_{inc}^i \cdot R_{tot}^i \cdot e^{jk(\bar{r}_i \cdot \hat{r}_o)}$$

where

$$\begin{aligned} E_{inc}^i &= \text{incident field at } i^{\text{th}} \text{ patch} \\ R_{tot}^i &= R_{\theta\theta}^i + S_{\theta\theta}^i \\ \bar{r}_i &\text{ is a vector from the origin to the } i^{\text{th}} \text{ patch} \\ \hat{r}_o &\text{ is a unit vector in the direction } (\theta, \phi) \end{aligned} \tag{2-15}$$

Because only one polarization is assumed, all quantities above are scalars and only the co-polarized field can be computed.

The incident field at each unit cell is more accurately described by a combination of TE and TM polarized plane waves incident at $(\theta, \phi) = (\theta_i, \phi_i)$, where the subscript i denotes the unit cell of interest in the reflectarray. This, however, provides a much more complex problem. Due to the difference in specular reflection, the moment method solution must be run separately for the TE and TM components. Also, computation of the reflectarray scattered field is more complex due to the fact that more than one field component is now present in the total scattered field.

In order to compute the reflectarray scattered field, equivalent electric currents are defined which produce the computed total far field. To find these currents, an infinite array of infinitesimal dipoles on the dielectric substrate is assumed, and the element at the origin in this infinite array is placed in the unit cell of interest in the finite reflectarray. The

procedure for defining the infinitesimal current starts by obtaining the total reflected and scattered far field components, E_θ and E_ϕ , from the infinite array solution outlined in Section 2.2. Then, following theory presented in [13],

$$E_x = \cos \theta \cos \phi E_\theta - \sin \phi E_\phi \quad (2-16a)$$

$$E_y = \cos \theta \sin \phi E_\theta + \cos \phi E_\phi \quad (2-16b)$$

and

$$J_x = \frac{ab}{\tilde{G}_{xx}\tilde{G}_{yy} - \tilde{G}_{xy}^2} (\tilde{G}_{yy}E_x - \tilde{G}_{xy}E_y) \quad (2-17a)$$

$$J_y = \frac{ab}{\tilde{G}_{xx}\tilde{G}_{yy} - \tilde{G}_{xy}^2} (-\tilde{G}_{xy}E_x + \tilde{G}_{xx}E_y) \quad (2-17b)$$

where \tilde{G} is the Fourier transform of the Green's function listed in the Appendix and is evaluated at the point $(k_x, k_y) = (\sin \theta \cos \phi, \sin \theta \sin \phi)$.

An infinite array of these infinitesimal dipoles (with appropriate phasing to generate a plane wave at the required angle) produces the same *total* field (specular and radiated) that was computed from the moment method solution. Then, the "unit cell" concept is employed and the infinitesimal current located at the origin is placed in the unit cell of interest in the finite reflectarray. Repeating this procedure for each cell in the reflectarray produces a finite array of infinitesimal dipoles that is the same size as the reflectarray. The pattern function for this array is then easily computed. An alternative method for the calculation of the pattern function for the reflectarray without using these equivalent currents is presented in [16].

By using this approach, it is possible to see the dependence of reflection phase versus azimuth incidence angle. A plot of the normalized reflection phase for the co-polarized field versus azimuth incidence angle for several different incidence angles in elevation is shown in Figure 2.7. It is seen that when the elevation angle is small there is not much difference in the reflection phase versus azimuth, but as the elevation angle increases there is a large deviation in the reflection phase. This result is not unexpected, since for larger incidence angles in elevation there is a marked difference in the specular

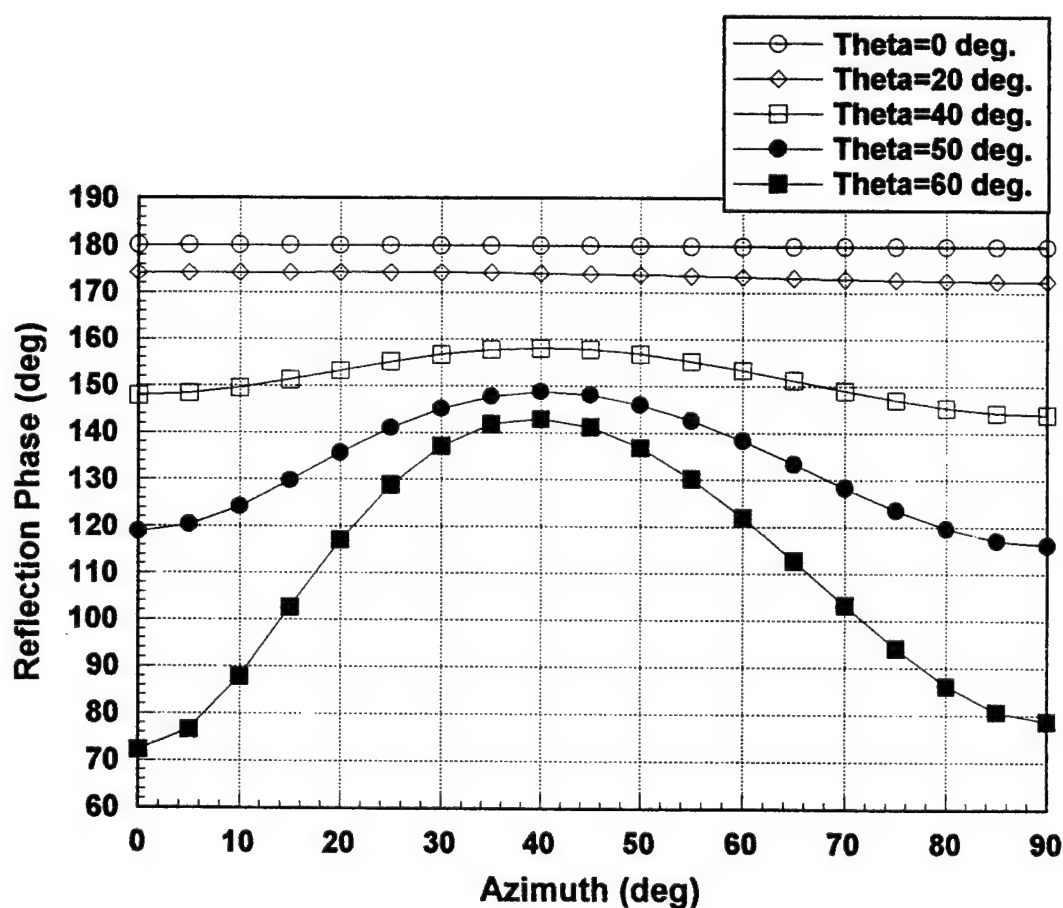


Figure 2.7. Computed reflection coefficient phase versus azimuth incidence angle for different elevation incidence angles. $f=28$ GHz, $a=.5442$ cm, $b=.5442$ cm, $\epsilon_r=2.2$, $d=.0508$ cm, $\tan \delta=.0028$, $l=.315$ cm, $w=.315$ cm

reflection phase for TE and TM components of the reflected field. However, it is interesting to note that the reflection phase for purely TM ($\phi=0^\circ$) and purely TE ($\phi=90^\circ$) incidence is not that different; it is the case where the ratio of TM and TE components in the incident field is almost equal (around $\phi=45^\circ$) where the largest deviation in reflection phase (as referenced to the value for purely TM incidence) occurs.

For reflectarray designs with an f/D ratio of 0.7 or higher, there are few unit cells where the elevation incidence angle is large enough to cause any significant change in the reflection phase versus azimuth, and in these cases the approximation of using a TM polarized plane wave incident at angle $(\theta, \phi)=(\theta_i, 0)$ at each unit cell is quite good. However, for designs with a lesser f/D , care should be taken in the design process to account for phase deviation with azimuth as this effect is more significant.

Another interesting phenomenon which occurs in using this approach is the generation of a cross-polarized field. Again, due to the difference in the specular reflection phase for TE and TM components of the reflected field, a cross-polarized field results. This field is not unlike the cross-polarized component generated by a parabolic reflector; for a broadside beam the cross-polarized field is zero in the principal planes and has its maximum in the diagonal plane. In the analysis presented here, the cross-polarized field is modeled by the y-directed currents as given in (2-17b).

An example of the currents used in the computer model is shown in Figure 2.8. For this design, the main beam was scanned off to 25° in the E-plane (x-direction). Note the anti-symmetry of the y-directed currents with respect to the x-axis; this produces a null in the E-plane for the cross-polarized field. If the reflectarray was designed to produce a broadside beam, a similar anti-symmetry would exist with respect to the y-axis, producing

Equivalent Currents Generated by Reflectarray

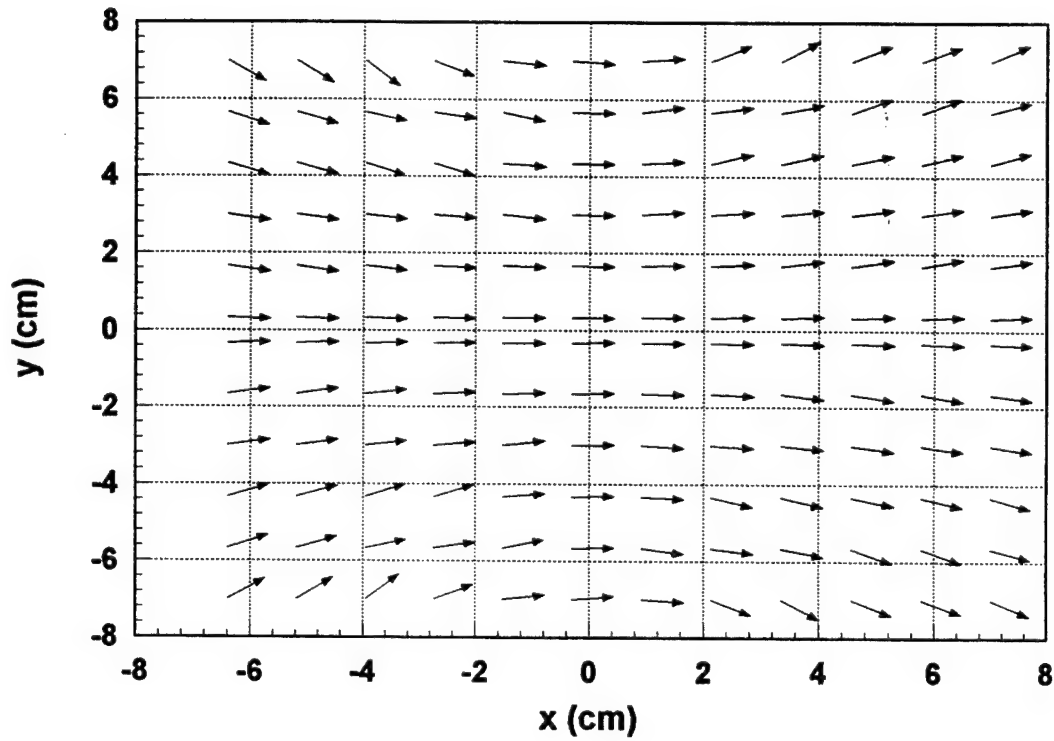


Figure 2.8. Example of equivalent currents used in computer model for reflectarray scattered field.
 $f=27.3$ GHz, $a=.6087$ cm, $b=.6667$ cm, $\epsilon_r=2.95$, $d=.0254$ cm, $\tan \delta=.0074$, $l=.3$ cm,
 $w=.3$ cm, $\theta=0^\circ$, $\phi=0^\circ$.

a null in the cross-polarized field in the H-plane. Measured results support this type of behavior, as will be shown in Chapter 3.

2.4 Finite Reflectarray Design

As previously stated, the "unit cell" concept is employed in the process of using the data from the solution of the infinite array problem to design the finite sized reflectarray. The incident spherical wave from the feed is locally approximated by a plane wave at each unit cell. The required phase is achieved by selecting the proper patch length from the infinite array data, and a patch of that size is placed inside the corresponding unit cell in the finite reflectarray. This design process has been used before [13],[14], but is included here for completeness.

The required phase at each element is arrived at by ray tracing, and the geometry of the finite reflectarray is shown in Figure 2.9. The incident phase at each unit cell is $-k_o R_i$, where k_o is the free space wavenumber at the design frequency. In order to offset the phase delay from the incident spherical wave, a phase shift of $+k_o R_i$ is required. Then, to create a planar wavefront at angle θ_o , an additional phase shift is needed. This gives the total required phase shift at each element as

$$\phi_i = k_o (R_i - \bar{r}_i \cdot \hat{r}_o) \quad (2-18)$$

where \hat{r}_o is a unit vector in the direction of the main beam. In this work, only cases where the main beam is scanned off broadside in the E-plane are considered. This simplifies (2-18) to

$$\phi_i = k_o (R_i - x_i \sin \theta_o) \quad (2-19)$$

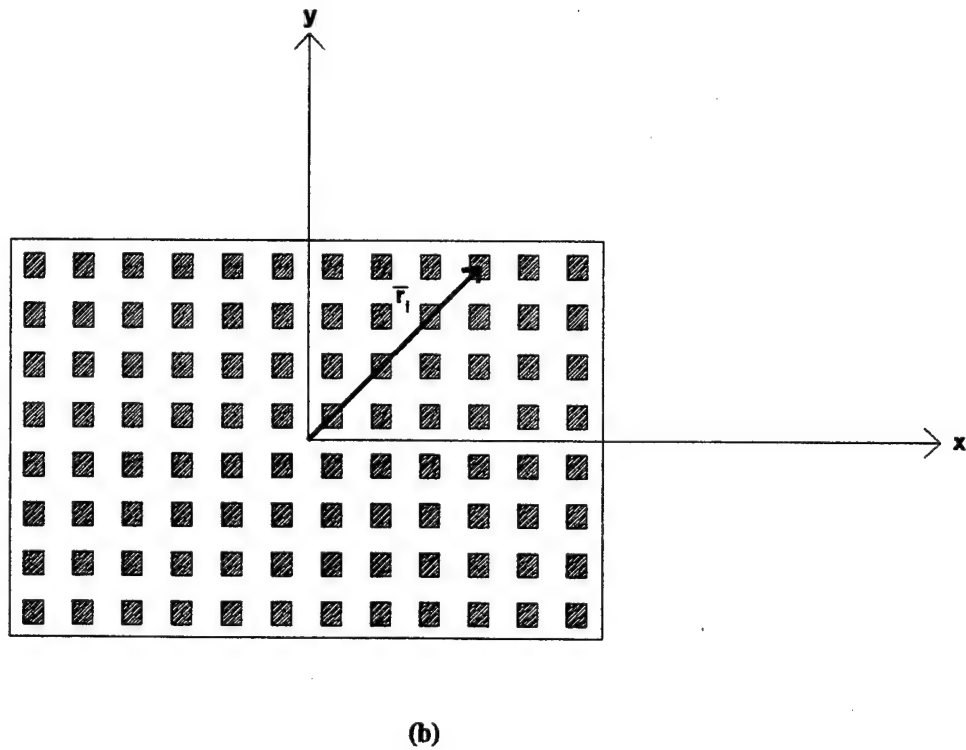
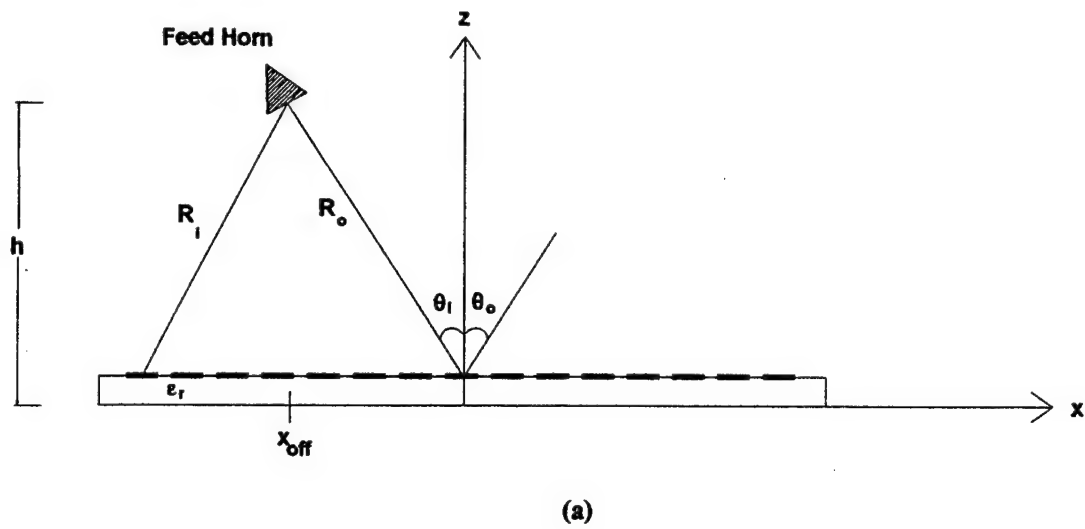


Figure 2.9. Geometry of finite sized reflectarray. (a) Side view. (b) Top view.

2.5 Prime Focus and Offset Feeds

Using a prime focus feed is the most straightforward design approach for a reflector or reflectarray. This corresponds to the geometry of Figure 2.9 by having $x_{\text{off}}=0$ and $\theta_i=0^\circ$. Unfortunately, this configuration results in aperture blockage effects and, in reflectarrays which are scanned off broadside, beam squint with frequency occurs. For high gain reflectarrays with narrow beamwidths, this poses a serious problem.

The offset feed is more attractive in the sense that aperture blockage effects are minimized, at the expense of a slightly more complicated design and analysis procedure. Also, the effect of beam squint with frequency can be greatly minimized by choosing the correct offset distance.

To gain insight into how beam squint with frequency occurs in reflectarrays scanned off broadside, a linear E-plane reflectarray is considered. For collimation of the main beam at angle θ_o , the progressive total phase (including all time delay effects from feed radiation and total reflection phase of the elements) is

$$\phi(x) = -k_f x \sin \theta_o \quad (2-20)$$

where k_f is the free space wavenumber at some frequency other than the design frequency. The beam pointing angle then depends on the differential phase,

$$\theta(x) = \sin^{-1} \left(-\frac{1}{k_f} \frac{d\phi(x)}{dx} \right) \quad (2-21)$$

Note that the main beam angle given by (2-21) depends on position in general. This can be interpreted as if a pair of elements close to that position are trying to create a main beam at angle $\theta(x)$. If there is no dependence on position, i.e. the derivative of $\phi(x)$ is constant, then there is no phase error across the the array and a well defined beam will be produced at angle θ .

Assuming that the incident phase at each patch is $-k_o R_i$, using (2-19) gives the total differential phase across the aperture as

$$\frac{d\phi(x)}{dx} = (k_o - k_f) \frac{x - x_{off}}{R_i} - k_o x \sin \theta_o \quad (2-22)$$

For a prime focus feed, $x_{off}=0$, and substitution into (2-21) yields

$$\theta(x) = \sin^{-1} \left(\frac{x}{R_i} \frac{k_f - k_o}{k_f} + \frac{k_o}{k_f} \sin \theta_o \right) \quad (2-23)$$

The position dependent term in (2-23) comes from a non-progressive quadratic phase error which results in higher sidelobes and loss in gain but does not affect the position of the main beam [17]. With this in mind, the beam pointing angle becomes independent of position and is given by

$$\theta = \sin^{-1} \left(\frac{k_o}{k_f} \sin \theta_o \right) \quad (2-24)$$

For the offset feed, the position dependent term in (2-22) results from a combination of linear and quadratic phase errors, so that this term now affects the position of the main beam. However, we can use this linear phase error to reduce the beam squint effect in (2-24) with the correct choice of feed offset.

Using the condition in (2-20), no beam squint will occur if

$$\frac{d\phi(x)}{dx} = -k_f \sin \theta_o \quad (2-25)$$

Substitution into (2-22) yields

$$\sin \theta_o = \frac{x - x_{off}}{R_f} \quad (2-26)$$

The above condition is again a function of position, and cannot be met for all values of x . The beam position then depends on a weighted average of $\theta(x)$ as defined by (2-21). A very good criterion to use for reducing beam squint with frequency is to enforce (2-26) at $x=0$. This yields simply,

$$\theta_o = \theta_i \quad (2-27)$$

where θ_i is defined as the angle from the phase center of the feed element to the center of the array, as depicted in Figure 2.9.

In order to show the reduction in beam squint with frequency for the offset feed, a 64 element linear E-plane reflectarray using constant phase shifters for the

elements was analyzed for both offset and prime focus feeds. The condition of (2-27) was implemented for the offset feed, and the main beam was scanned to 40° in the E-plane at the center frequency of 11.95 GHz. A plot of main beam position versus frequency for both cases is shown in Figure 2.10. It is evident that the beam squint is eliminated for the offset case, while there is a great deal of movement of the main beam with the prime focus feed.

The condition of (2-27) is generally good enough to prevent any appreciable squint of the main beam, however, the position of the main beam is also a function of the feed illumination. The tilt angle of the feed horn with respect to the normal to the reflectarray plane, θ_h , can also slightly affect beam squint. Setting $\theta_h = \theta_i = 40^\circ$ gave a total beam squint of $\pm 0.1^\circ$ over the frequency range shown, while setting $\theta_h = 42^\circ$ gave the result of Figure 2.10, an elimination of practically all beam squint over the range of frequencies.

2.6 Computation of Reflectarray Directivity

The pattern function, $F(\theta, \phi)$, of (2-15) computes only the co-polarized component of the reflectarray scattered field. However, since the amount of power in the cross-polarized field is extremely small, (2-15) can be used in computing the directivity of the reflectarray. The simplicity of the equation also makes it well suited for this purpose.

The directivity of the reflectarray can be computed as

$$D_o = 4\pi \frac{F^2(\theta, \phi)|_{\max}}{\int_0^{2\pi} \int_0^\pi F^2(\theta, \phi) \sin \theta d\theta d\phi} \quad (2-28)$$

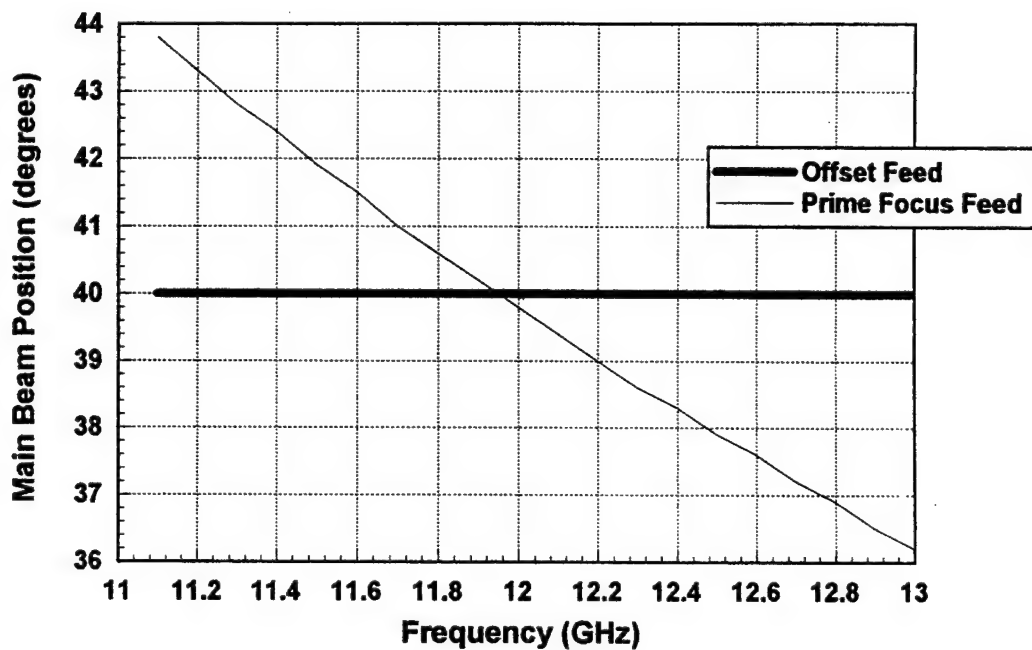


Figure 2.10. Position of main beam versus frequency for 64 element E-plane linear reflectarray. Feed illumination is $\cos^8\theta$. $x_{off} = -42\text{cm}$, $h = 50\text{cm}$ for offset feed; $h = 70\text{cm}$ for prime focus feed.

The denominator is the radiated power from the reflectarray. However, the double integration in this expression must be computed numerically. Each point taken for the integration involves a summation over all unit cells as defined in (2-15). For the cases of interest in this work, high gain reflectarrays with hundreds or even thousands of elements, this approach is computationally infeasible. Also, the narrow beamwidths of these arrays require many more integration points to be taken.

To increase the computational efficiency of the problem, the directivity is computed by an approximate method which is accurate when there is not a very large amount of phase error across the array. The radiated power is computed as the sum of the reflected power (same as incident power for the lossless case) from each unit cell. Each unit cell is modeled as a uniform aperture; the expression for the radiated far-field of the uniform aperture [18] is used in computing the numerator, while the aperture distribution itself is integrated to find the radiated power. The expression for directivity then becomes

$$D_o = \frac{4\pi ab}{\lambda^2} \cos \theta_o \frac{\left| \sum_{i=1}^N E_i^{inc} \cdot R_i^{tot} \cdot e^{jk(\hat{r}_i \cdot \hat{r}_o)} \right|^2}{\sum_{i=1}^N |E_i^{inc} \cdot R_i^{tot}|^2} \quad (2-29)$$

where the unit vector \hat{r}_o is in the direction of maximum radiation. The $\cos \theta_o$ term takes into account the projected aperture as the main beam is scanned off broadside. This expression takes taper losses into account, but does not include spillover losses. These losses will be explained more fully in section 2.7.1.

2.7 Microstrip Reflectarray Gain-Loss Budget

An excellent way to gain insight into the performance of microstrip reflectarrays is through a gain-loss budget. By examining such a budget, one can establish the maximum gain possible for a given size reflectarray, quantify all sources of loss, and then use that information to improve on a particular design.

The maximum directivity for the reflectarray aperture occurs when all terms in the numerator summation of (2-29) are in phase and equal in magnitude, yielding

$$D_o^{\max} = \frac{4\pi Nab}{\lambda^2} \cos \theta_o \quad (2-30)$$

The gain of the reflectarray is then related to the maximum directivity by

$$G = \eta D_o^{\max} \quad (2-31)$$

The overall efficiency of the reflectarray, η , is a product of several individual sources of loss which decrease the gain. In general, the efficiency is given by

$$\eta = \eta_s \eta_t \eta_p \eta_c \eta_d \eta_x \eta_b \eta_r \quad (2-32)$$

where

η_s = spillover efficiency
 η_t = taper efficiency
 η_p = phase efficiency
 η_c = conductor efficiency
 η_d = dielectric efficiency
 η_x = polarization efficiency
 η_b = aperture blockage efficiency
 η_{sw} = surface wave efficiency
 η_r = random error efficiency

The main sources of loss in the reflectarray are spillover, taper, conductor, dielectric, and phase error loss, and therefore these losses only will be considered. Polarization loss, resulting from power being scattered into cross-polarized fields, and aperture blockage loss, resulting from power reflected from the reflectarray surface being blocked by the feed or its supporting structure, are very small as compared to other sources of loss and are therefore ignored. For very large planar microstrip arrays such as the ones incorporated into the typical microstrip reflectarray design, surface wave losses are also very small. Losses due to random surface errors are included in phase loss.

2.7.1 Spillover and Taper Loss

Spillover loss occurs from power radiated by the feed that is not intercepted by the reflecting surface, i.e. it "spills over" the edge. Taper loss occurs from having a non-uniform field incident on the reflectarray surface. An ideal feed source would provide uniform illumination over the surface of the reflectarray and would not radiate at all in other regions, but this is not physically realizable.

For practical feeds, there exists a tradeoff between spillover and taper loss. A good basis for choosing a feed is for it to have about a -10dB taper at the edge of the reflectarray, which usually provides a near optimal tradeoff between spillover and taper losses. The maximum product of spillover and taper efficiencies is approximately 0.8 for practical feeds.

Spillover efficiency can be computed by integrating the Poynting vector over the reflectarray surface and dividing the result by the total radiated power from the feed.

$$\eta_s = \frac{\frac{1}{2} \iint_S \bar{\mathbf{E}} \times \bar{\mathbf{H}}^* \cdot d\bar{\mathbf{s}}}{\int_0^{2\pi} \int_0^{\pi/2} F_{feed}(\theta, \phi) \sin \theta d\theta d\phi} \quad (2-33)$$

where F_{feed} is the power pattern of the feed and the integration in the numerator is over the reflectarray surface. Some algebraic manipulation yields

$$\eta_s = \frac{\iint_S \frac{F_{feed}(\theta, \phi)}{R^2} \cos \theta ds}{\int_0^{2\pi} \int_0^{\pi/2} F_{feed}(\theta, \phi) \sin \theta d\theta d\phi} \quad (2-34)$$

Both of these integrations are easily computed numerically, and the integration in the numerator can be in either rectangular or polar coordinates, depending on the surface geometry.

Taper efficiency can be computed easily by eliminating phase error from (2-29) and comparing the result to the maximum directivity of (2-30). This yields

$$\eta_t = \frac{\left(\sum_{i=1}^N |E_i^{inc} \cdot R_i^{tot}| \right)^2}{\sum_{i=1}^N |E_i^{inc} \cdot R_i^{tot}|^2} \quad (2-35)$$

2.7.2 Dielectric and Conductor Loss

At millimeter wave frequencies, dielectric and conductor losses in large microstrip structures can become quite high. Microstripline fed arrays typically suffer from high losses in the feed network. One of the distinct advantages of microstrip reflectarrays over series or corporate fed microstrip arrays at these frequencies is the elimination of feed network losses, however, dielectric and conductor losses are still present in a microstrip reflectarray.

Dielectric loss is easily found by using a complex permittivity in the moment method analysis,

$$\epsilon = \epsilon_o \epsilon_r (1 - j \tan \delta) \quad (2-36)$$

Conductor loss is slightly more involved to calculate. It can be computed in the moment method solution by enforcing the condition $\bar{E}_{tan} = Z_s \bar{J}$ on the patch surface, where Z_s is the surface impedance of the conductor [15]. This changes the impedance matrix elements of (2-7) to

$$Z_{ij} = -\frac{1}{ab} \sum_{m=-\infty}^{\infty} \sum_{n=-\infty}^{\infty} \bar{F}_i^* \cdot \bar{G} \cdot \bar{F}_j + \Delta Z_{ij} \quad (2-37)$$

where

$$\Delta Z_{ij} = Z_s \iint_s \bar{J}_i \cdot \bar{J}_j ds \quad (2-38)$$

$$Z_s = (1 + j) \sqrt{\frac{\omega \mu}{2\sigma}} \quad (2-39)$$

With the edge mode of (2-12a) having the index 1 and the entire domain mode of (2-10) (with $m=1$) having the index 2, substitution of these modes into (2-38) yields

$$\Delta Z_{11} = \frac{2Z_s l}{3w} \quad (2-40a)$$

$$\Delta Z_{12} = J_1(\pi/2) \frac{Z_s l}{w} = 0.5668 \frac{Z_s l}{w} \quad (2-40b)$$

$$\Delta Z_{22} = \frac{Z_s l}{2w} \quad (2-40c)$$

where l is the patch length and w the patch width.

Due to the nature of the moment method solution, dielectric and conductor loss cannot be separated without running the solution twice to isolate each source of loss. Therefore, it is convenient to consider both sources of loss in one variable as the conductor-dielectric efficiency.

The total conductor-dielectric efficiency can be computed as

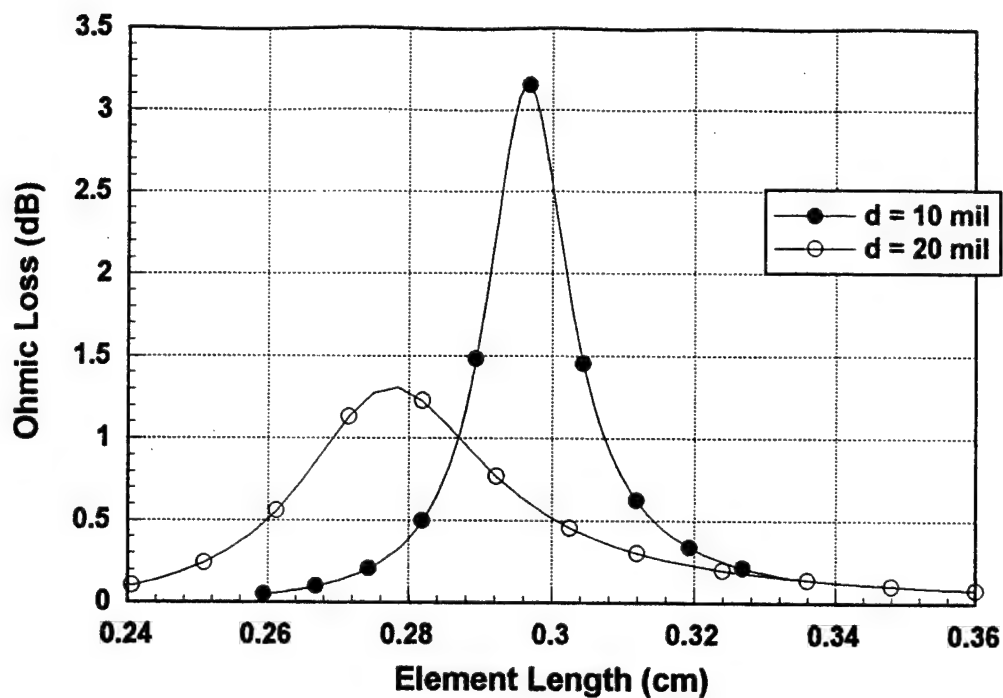
$$\eta_{cd} = \frac{\sum_{i=1}^N |R_i^{tot}|}{N} \quad (2-41)$$

Figure 2.11a shows the total conductor and dielectric loss for patches of different lengths and constant width on various substrate thicknesses. It is evident that the loss is large for patches near resonance, but is smaller for patches of other lengths. A slight shift in resonant frequency between the two cases is also evident. This is due to the fact that the fields underneath the patch are intensified near resonance, and the high loss tangent of the material causes a large amount of dielectric loss. Patches on thicker substrates have significantly less loss than those on thin substrates.

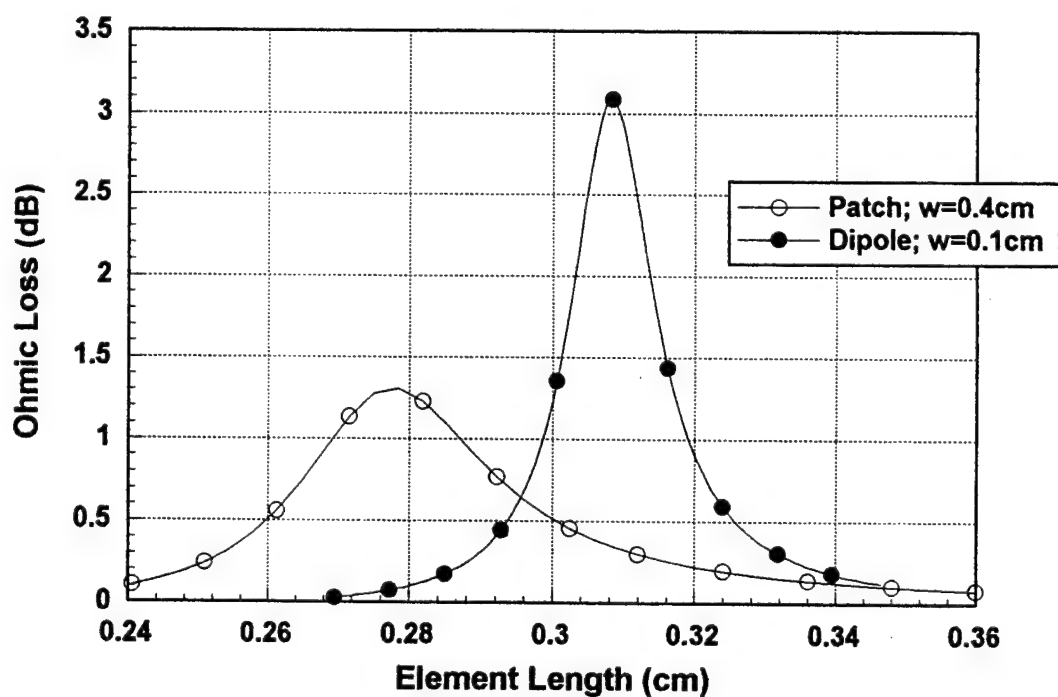
Figure 2.11b shows total conductor and dielectric loss for patches of various widths and lengths, while the substrate thickness is held constant. Loss for the thin dipole is much greater near resonance than for the wide patch, however, the loss for the dipole drops off sharply so that loss for the wide patch is slightly greater for patches off resonance. This is explained by the narrowband nature of the printed dipole. The higher loss for the resonant dipole is explained by increased conductor loss which is caused by high current density on the dipole.

2.7.3 Losses Due to Phase Errors

In the microstrip reflectarray application, there are two main sources of phase error, namely, phase error incurred in the design process and random phase errors resulting from fabrication tolerances. These phase errors reduce the directivity of the array, and therefore decrease the overall efficiency.



(a)



(b)

Figure 2.11. Computed ohmic (conductor and dielectric) losses for reflectarray elements. (a) for varying substrate thicknesses; element width is 0.4cm. (b) for varying element widths; substrate thickness is 0.0508cm. $f = 27.3$ GHz, $a = .6087$ cm, $b = .6667$ cm, $\epsilon_r = 2.95$, $\tan \delta = .0074$, $\theta = 0^\circ$, $\phi = 0^\circ$.

Three types of phase error occur in the design process. One source is the dependence on the reflection phase versus azimuth incidence angle, as was described in Section 2.3. For most of the designs presented in the next chapter, only the incidence angle in elevation was considered in the design process. For the other designs, sets of data were computed at azimuth incidences of 0° , 45° , and 90° , and the appropriate patch lengths were interpolated from this data. Each design method contributes some small phase error, however, and the resultant directivity loss can be quantified by taking azimuth incidence angle into account in the reflectarray analysis.

Phase error also results from the fact that the entire range of reflection phases from 0 to 360 degrees cannot be achieved, as can be seen by examining the reflection phase versus patch length curve of Figure 2.12. Basically, the range of unattainable phases is equal to $2k_0 d \cos \theta$ for square or wide patches. This phenomenon occurs because the grid of patches looks like a ground plane as the patch sizes approach the size of the unit cell. For narrow width dipoles, this effect is not as apparent and a greater range of phases may be attained. Phase error contributed in this manner can be also be quantified in the reflectarray analysis.

Another source of error that occurs in the design process comes from the use of the infinite array approximation. When computing the reflection phase it is assumed that all elements are of equal dimensions, but in the actual reflectarray this is not the case as each unit cell contains a patch of a different length. The effect of mutual coupling, albeit small, is obviously different in these two cases, resulting in an error in the computed resonant frequency of each patch, and therefore phase error. This phase error is smaller for patches with wider bandwidth, as for these cases a shift in resonant frequency contributes less phase error. Unfortunately this error can not be quantified without

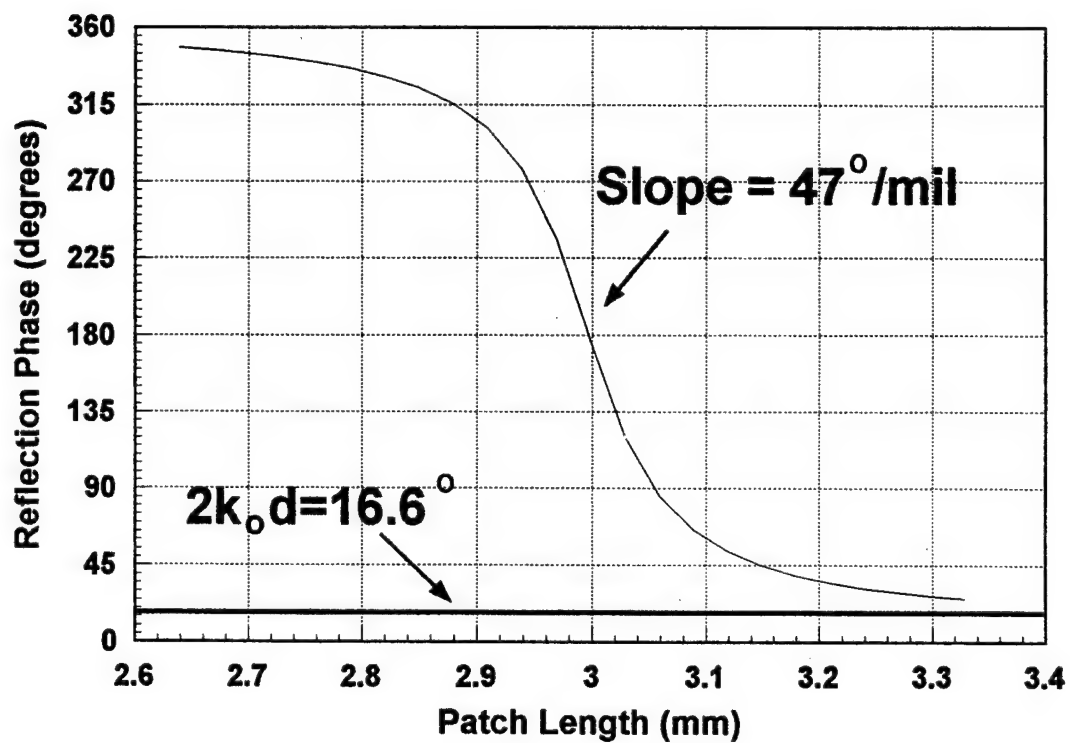


Figure 2.12. Reflection phase versus patch length for plane wave scattering from an infinite array of microstrip patches. $f=27.3$ GHz, $a=.6087$ cm, $b=.6667$ cm, $\epsilon_r=2.95$, $d=.0254$ cm, $\tan \delta=.0074$, $l=.3$ cm, $w=.3$ cm, $\theta=0^\circ$, $\phi=0^\circ$.

computing the actual moment method solution for the finite reflectarray, which is computationally impractical.

At millimeter wave frequencies, slight random errors in fabrication (specifically, etching errors which affect the size of each patch) have the potential to create large phase errors. This is separate from systematic errors in fabrication, which will instead cause a shift in operating frequency. The potential for phase error is evident by examining the reflection phase versus length curve as depicted in Figure 2.12. Most patches in a typical reflectarray design are close to resonant length and operate in the linear region of the curve. For the particular case shown, the slope of the linear region is $47^\circ/\text{mil}$, and for a fabrication tolerance of 0.5 mil for each edge, random fabrication error can contribute as much as 47° of phase error. Again, this effect is not as significant for patches that exhibit wider bandwidths since the slope of the linear region is not as great.

Random phase error contributed from fabrication tolerances, substrate inhomogeneties, surface errors, etc. also cannot be quantified analytically. All of the phase errors that cannot be quantified analytically are a possible source of directivity loss. If the rms phase error is known, the approximate directivity loss for small phase errors is given by [19]

$$D = D_o \frac{1}{1 + \sigma^2} \quad (2-41)$$

where D_o is the directivity without phase error and σ is the rms phase error across the array. As will be demonstrated in the next chapter, these phase errors are not large enough to disable the beam collimation effect of the reflectarray.

CHAPTER 3

MICROSTRIP REFLECTARRAY DESIGN EXAMPLES

3.1 Introduction

In order to test the validity and feasibility of the analysis and design procedure described in the previous chapter, six reflectarray examples were designed, fabricated, and tested. A short description of each of these reflectarray examples is given in Table 3.1.

Table 3.1. List of microstrip reflectarray designs.

Design #	Approximate Design Frequency	Size	Substrate (ϵ_r , thickness)	F/D Ratio	Feed Type
1	5.3 GHz	18"x24"	Rogers 5870 2.33, 62 mil	0.866	Pyramidal Horn
2	28 GHz	6"x6"	Taconic TLE 2.95, 10 mil	0.656	Corrugated Conical Horn
3	28 GHz	6"x6"	Rogers 5880 2.20, 20 mil	0.656	Corrugated Conical Horn
4	28 GHz	9" diameter circular	Taconic TLE 2.95, 10 mil	0.33	Backfire Feed [21]
5	76 GHz	6"x6"	Rogers 5880 2.20, 5 mil	0.33	Open-ended waveguide
6	76 GHz	6"x6"	Rogers 5880 2.20, 5 mil	0.33	Cassegrain

In this chapter, measured results are presented for each of the design examples and are compared with theoretical predictions. Differences between measured and computed results are discussed, along with possible explanations for the discrepancies. A gain-loss budget is presented for each example, and each budget is examined in order to gain insight on how to improve the design. Also, several theoretical and measured radiation patterns are presented for each design over a given bandwidth.

3.2 Microstrip Reflectarray Design Example #1

Design #1 was constructed in order to provide a direct comparison with the stub-tuned microstrip reflectarray presented in [13]. This is a C-band design with the only difference from [13] being that variable sized patches are used to provide phase shift instead of stub tuned patches. The performance of both the stub-tuned reflectarray and the reflectarray using variable size patches is then compared.

A scaled mask of this reflectarray is shown in Figure 3.1. This design was constructed on a 62 mil thick Rogers 5870 substrate, with a relative permittivity of 2.33. The reflectarray measured 18"x24", and a triangular grid spacing was employed with $a=5.39\text{cm}$, $b=3.23\text{cm}$, and $\alpha=33.4^\circ$. The design consisted of 263 patches with a fixed width of 2.382cm and varying length. Wide fixed-width patches provide better bandwidth than square patches, however, they can only be used for linear polarization. The feed horn was a pyramidal horn with the same dimensions as that in [13], with an aperture size of 12.7cm x 8.89cm in the H-plane and E-plane, respectively. The feed was a prime focus feed placed 46.67cm over the face of the array, giving a f/D ratio of 0.866 with respect to the x-dimension of the reflectarray. The phase across the reflectarray was chosen to produce a main beam scanned to 25° in the E-plane (x-direction).

A curve of total reflection phase versus patch length for this design for broadside incidence is shown in Figure 3.2. Graphs such as this are the essential building block in the design process, but they can also lend some insight into the performance of the reflectarray even before it is analyzed. The familiar "s-shaped" curve that was evident in Figure 2.12 is also apparent here. Two aspects of the curve that lend insight into the performance of the reflectarray are the slope of the linear region near resonance and the

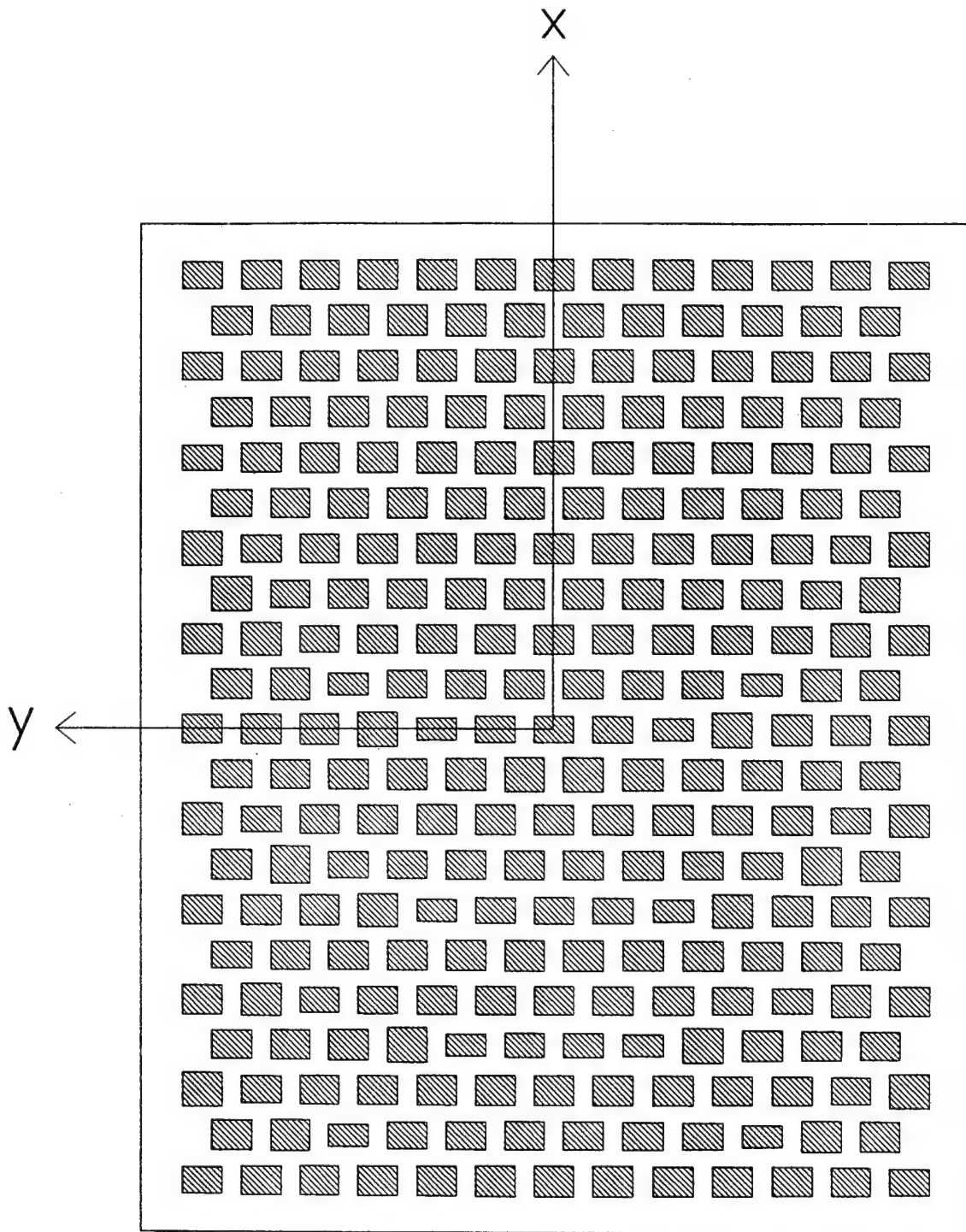


Figure 3.1. Scaled drawing of reflectarray design example #1.

Reflection phase versus length for broadside incidence

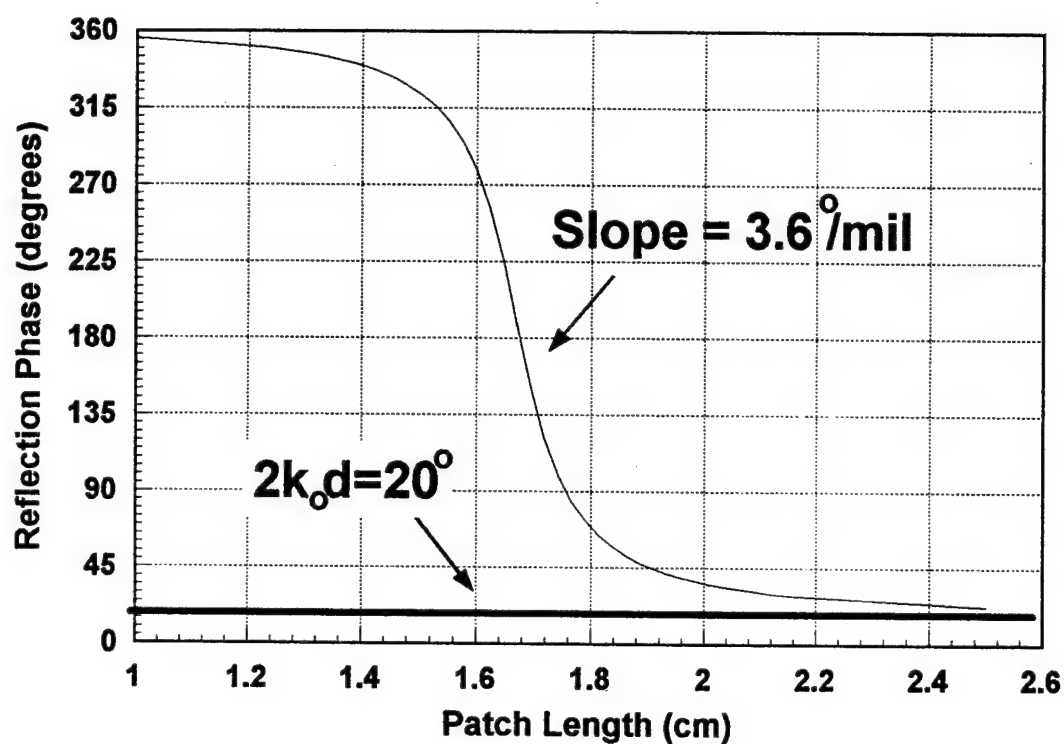


Figure 3.2. Computed reflection phase of infinite array of microstrip patches versus patch length. Triangular array grid. $f=5.3$ GHz, $a=5.39\text{cm}$, $b=3.23\text{cm}$, $\alpha=33.4^\circ$, $\epsilon_r=2.33$, $d=.158\text{cm}$, $\tan \delta=.001$, $w=2.382\text{cm}$, $\theta=0^\circ$, $\phi=0^\circ$.

range of reflection phases that cannot be attained, which is approximately equal to $2k_0d$ for patches. The slope of the linear region is directly related to the operating bandwidth of the reflectarray, and also can be a sign of how critical fabrication tolerances will be. Normally the range of phases that cannot be attained is small enough not to cause a significant change in the performance of the reflectarray, however, a region of 60° or more has the potential to deteriorate the performance significantly. Analyzing the data shown in Figure 3.2 yields the slope of the linear region to be $3.6^\circ/\text{mil}$ and a 20° range of phases that cannot be attained.

Computed and measured E-plane radiation patterns taken at the center-band frequency of 5.2 GHz are shown in Figure 3.3, and similar H-plane patterns are shown in Figure 3.4. This center frequency is slightly lower than the design frequency of 5.305 GHz due to the fact that only 7 entire domain modes were used in the design process, which employed an early version of the moment method computer program. Use of one entire domain mode and one edge condition mode as described in Section 2.2.1 predicts this frequency shift. Examination of the radiation patterns shows a very good comparison of measured and computed results. The H-plane patterns are in very close agreement, while the measured sidelobe level and 3dB beamwidth are slightly higher in the E-plane. These effects can be attributed to aperture blockage effects and phase errors that were not included in the analysis. In either event, the overall result is a small drop in directivity for the reflectarray.

Measured and computed H-plane cross-polarization patterns are shown in Figure 3.5. Agreement between measured and computed patterns is fairly good, considering the low level of cross-polarized radiation present. The measured level of -30dB relative to the co-polarized field is 3dB higher than the computed level but still very low. With such a low level of cross-polarized radiation, many factors can alter the measured patterns or

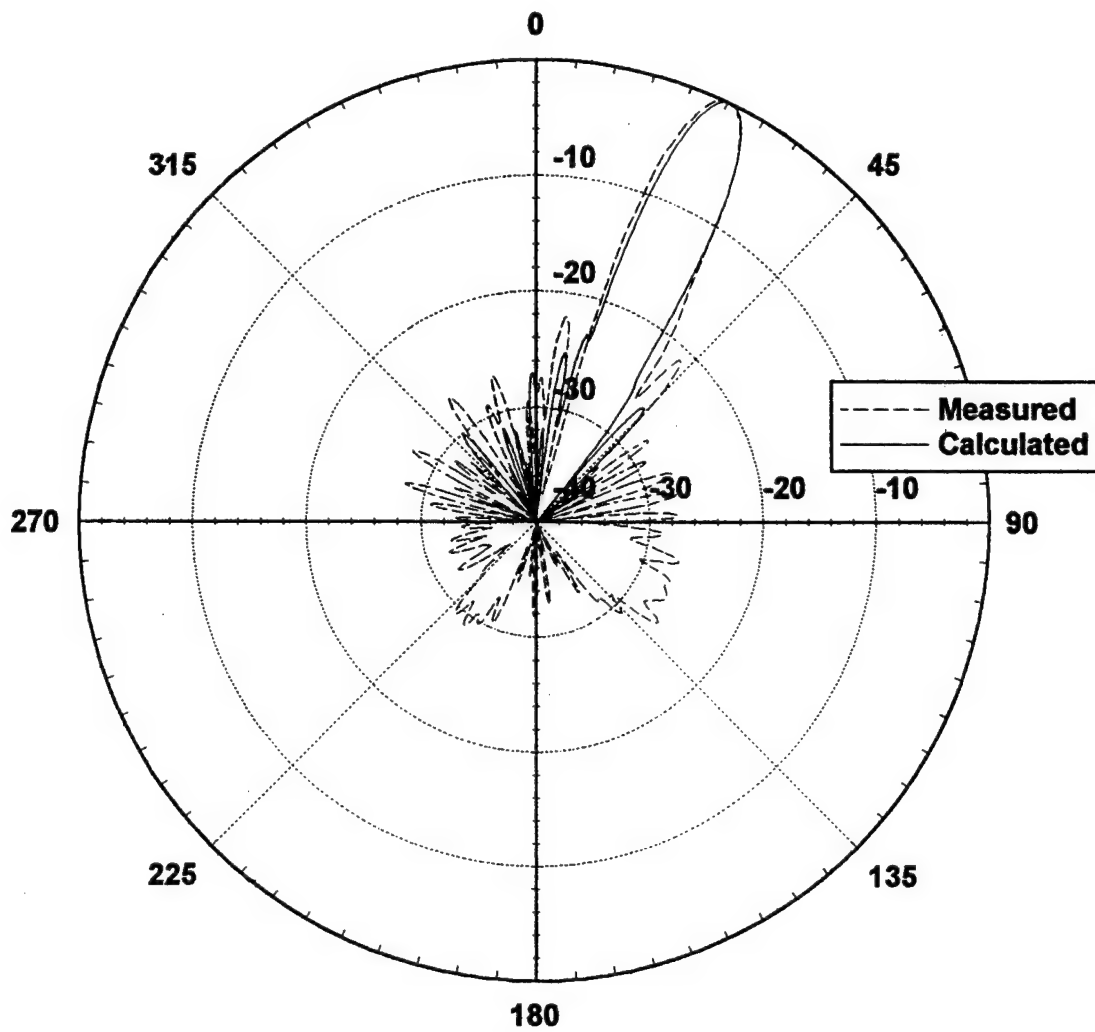


Figure 3.3. E-plane patterns at 5.2 GHz for reflectarray example #1.

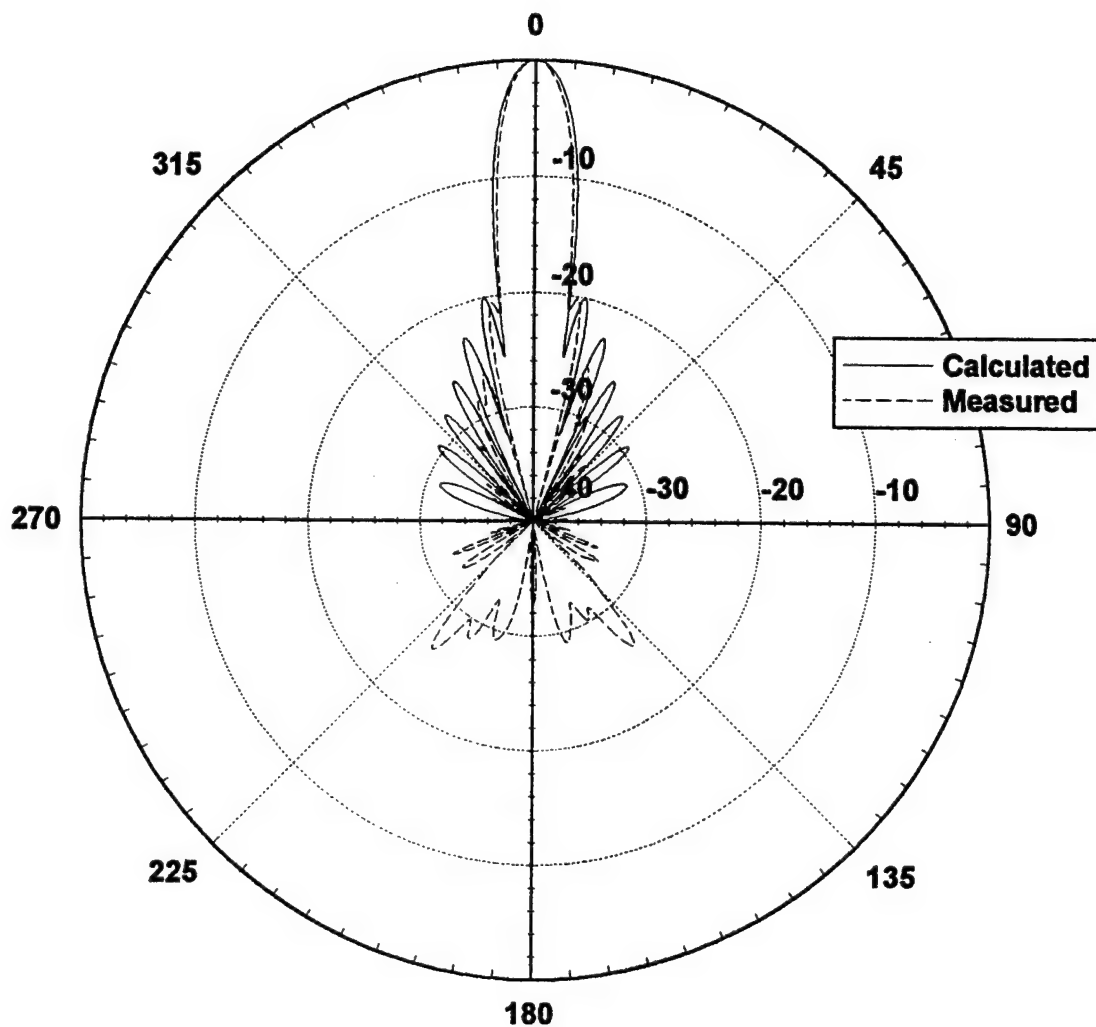


Figure 3.4. H-plane patterns at 5.2 GHz for reflectarray example #1.

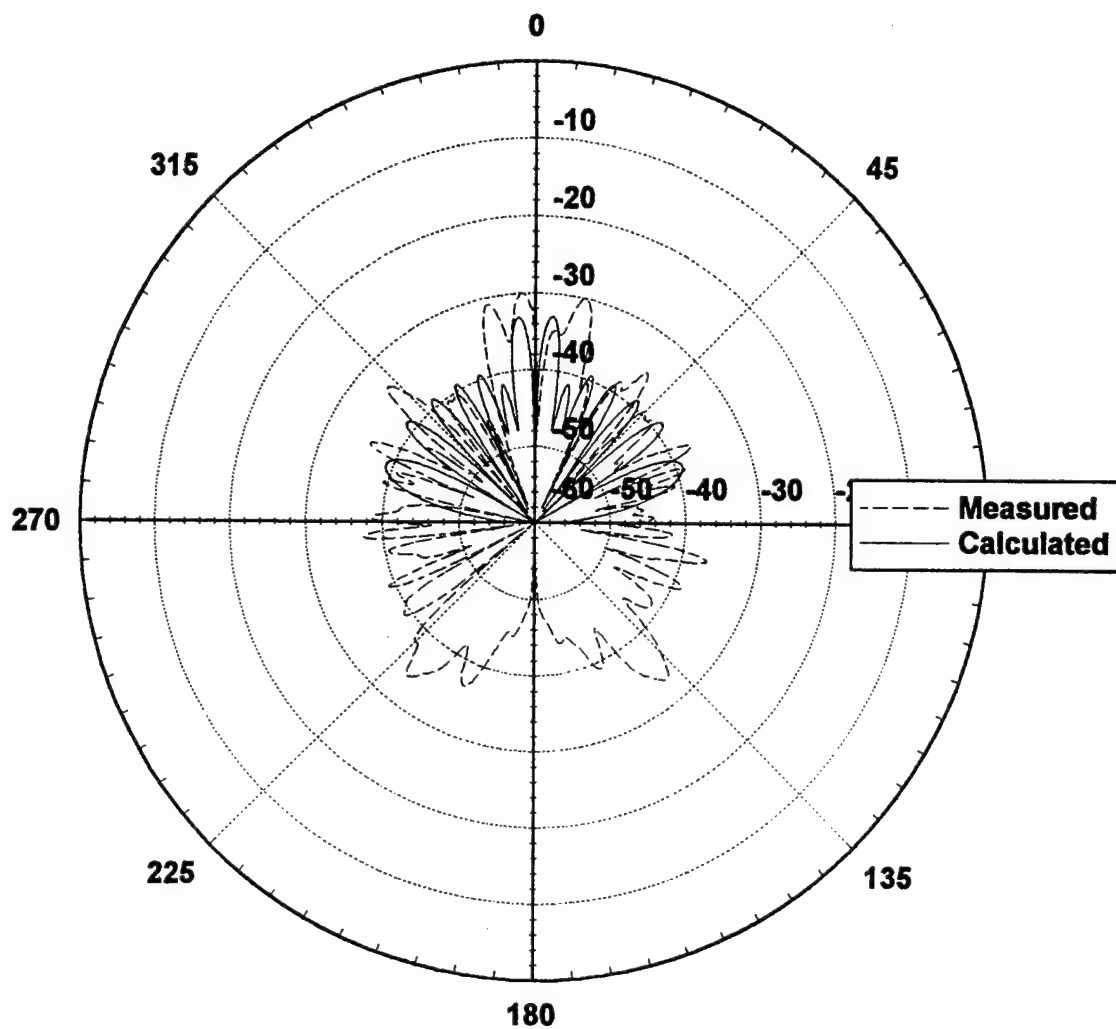


Figure 3.5. H-plane cross-polarization patterns at 5.2 GHz for reflectarray example #1.

relative amplitude of the field, such as scattering off of the feed or its supporting structure or misalignment between the feed, radiating patches, and the transmit horn.

To understand the degradation of the performance of the reflectarray with frequency, one can examine the radiation patterns at frequencies other than the design frequency. Such a plot is shown in Figure 3.6 - a plot of measured E-plane patterns at 5.2 GHz and 5.7 GHz. Two effects are immediately apparent from examining the plots; a beam squint with frequency as described in Section 2.5, and also a rise in the specular reflection from the reflectarray surface.

In most microstrip reflectarray designs, the majority of patches operate close to resonance at the center frequency. For this design example, 53% of all patches are within 5% of the resonant length of 1.71 cm at 5.2 GHz. Also, at resonance, the scattered field is 180° out of phase with the specularly reflected field [13]. This fact, combined with the abundance of patches that are operating near resonance, creates a cancellation of specular reflection near the design frequency. However, only 13% of all patches operate within 5% of resonance at 5.7 GHz; this leads to a rise in the specularly reflected field.

A gain-loss budget for this reflectarray at the center frequency of 5.2 GHz is shown in Table 3.2. Maximum directivity for the aperture and all losses were computed as described in Section 2.6. Measured gain at 5.2 GHz was 27.0 dBi, yielding an aperture efficiency of 58%. The computed gain of 27.53 dBi does not include losses due to random phase errors or aperture blockage effects, however, so the fact that the measured gain is about 0.5 dB less than the computed gain is not surprising. A plot of computed and measured gain is shown in Figure 3.7, and while the computed levels are slightly higher for most frequencies, the bandwidth for a 1 dB drop in gain compares well. A bandwidth of 5.0% is calculated, while a 4.5% bandwidth was measured. Taking into

account a possible gain measurement error of ± 0.5 dB, a computed bandwidth between 2.9% and 5.9% is within the limits of measurement error.

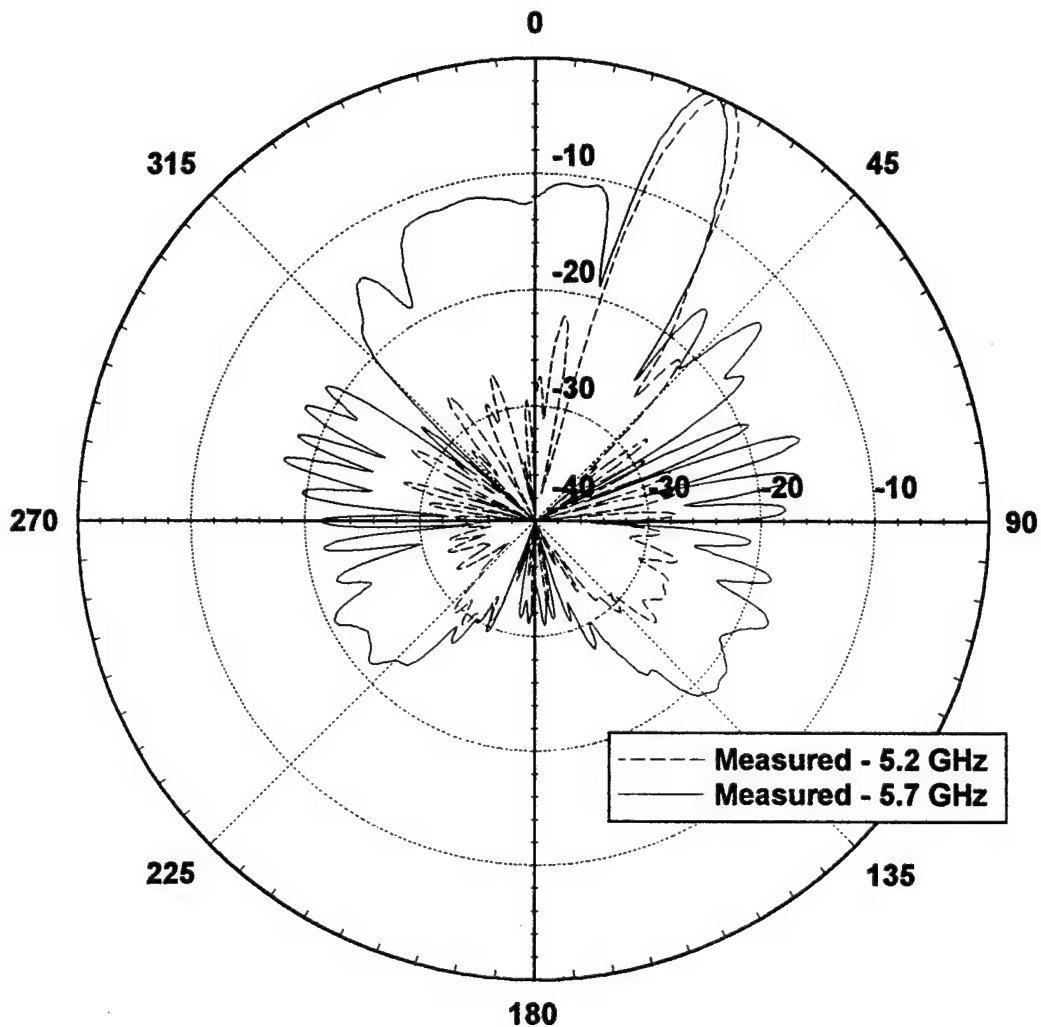


Figure 3.6. Measured E-plane radiation patterns at 5.2 GHz and 5.7 GHz.

Table 3.2. Gain-loss budget for reflectarray #1.

Maximum Directivity	29.78 dBi
Spillover Loss	-0.66 dB
Taper Loss	-0.83 dB
Cos θ Scan Loss	-0.43 dB
Dielectric and Conductor Loss	-0.15 dB
Design Phase Error	-0.18 dB
Computed Gain	27.53 dBi

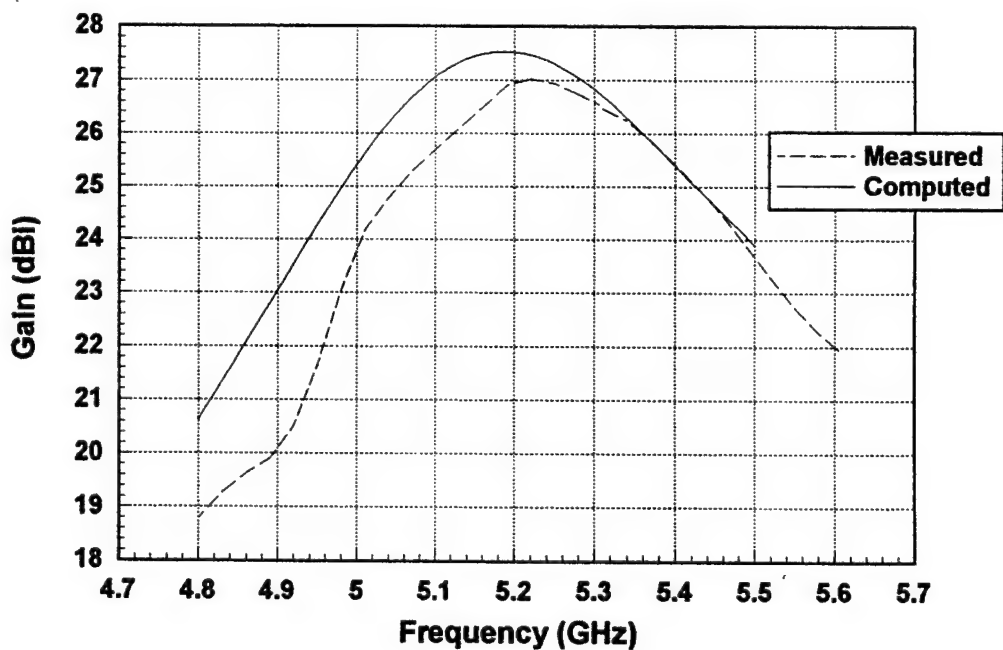


Figure 3.7. Measured and computed gain for reflectarray design example #1.

Table 3.3 shows a comparison of the performance of this reflectarray design using variable size patches to control the reflection phase versus the design presented in [13], which used stub tuned patches. The performance of both reflectarrays is similar, supporting the conclusion that both methods achieve essentially the same effect by shifting the resonant frequency of each patch. One difference between the performance of the two reflectarrays is the gain bandwidth (defined by a 1dB drop from the peak gain) - 3.7% for the stub tuned reflectarray and 4.5% for the reflectarray using variable size patches. A possible explanation is the fact that as the frequency shifts, both the electrical size of the patch and tuning stub shift in the same direction, causing the reflection phase from the unit cell to shift more than it would from just a single patch with no stub attached. However, due to the error inherent in the gain measurement, the difference in actual bandwidth may not be significant.

The use of variable size patches also introduces several favorable design characteristics. A triangular grid is no longer needed to accommodate the tuning stubs for each patch. Also, square patches may be used for either dual-linear or circular polarization.

Table 3.3. Microstrip reflectarray performance comparison.

	Reflectarray Using Tuning Stubs [13]	Reflectarray Using Variable Size Patches
Peak Gain	27.1 dBi	27.0 dBi
E-plane Beamwidth	7.7 degrees	7.5 degrees
H-plane Beamwidth	7.7 degrees	7.5 degrees
E-plane Sidelobe level	-22 dB	-20.5 dB
H-plane Sidelobe level	-18 dB	-20 dB
Gain bandwidth	3.7 %	4.6 %
E-plane cross polarization level	-29 dB	-40 dB

3.3 Microstrip Reflectarray Design Example #2

Design example #2 was a Ka-band reflectarray with a center frequency of 27.3 GHz. The motivation behind this design was to see if the reflectarray concept was feasible at this frequency due to the increased fabrication tolerances required, and to see the effect of larger random phase errors on the operation of the reflectarray.

A scaled overhead drawing of this reflectarray is shown in Figure 3.8. This design was constructed on a 10 mil thick Taconic woven PTFE substrate, with a relative permittivity of 2.95. The loss tangent of the material was estimated to be 0.0074 at 28 GHz using the guidelines of [20]. Data for the loss tangent of common microwave substrates is generally not available at frequencies above 10 GHz, but measured data at other frequencies suggests that the loss tangent increases approximately linearly with frequency. The reflectarray measured 6"x6", and a rectangular grid spacing was employed with $a=0.6087\text{cm}$ and $b=0.6667\text{cm}$. The design consisted of 528 square patches of varying size. The square patches, while providing less bandwidth than wide fixed-width patches, can be used for dual-linear or circular polarization. The feed horn was a corrugated conical horn with an aperture radius of 0.88cm and an axial length of 3.55cm. The feed was a prime focus feed placed 10cm over the face of the array, giving a f/D ratio of 0.656. As with the first design, the main beam was scanned 25° off broadside in the E-plane.

A curve of total reflection phase versus patch length for this design for broadside incidence was shown in Figure 2.12. The familiar "s-shaped" curve is evident - this curve is characteristics of all of the design examples presented here. Analyzing the data shown in Figure 2.12 yields the slope of the linear region to be $47^\circ/\text{mil}$, with a 16.6° region of phases that cannot be attained. The slope of the linear region is increased by a factor of

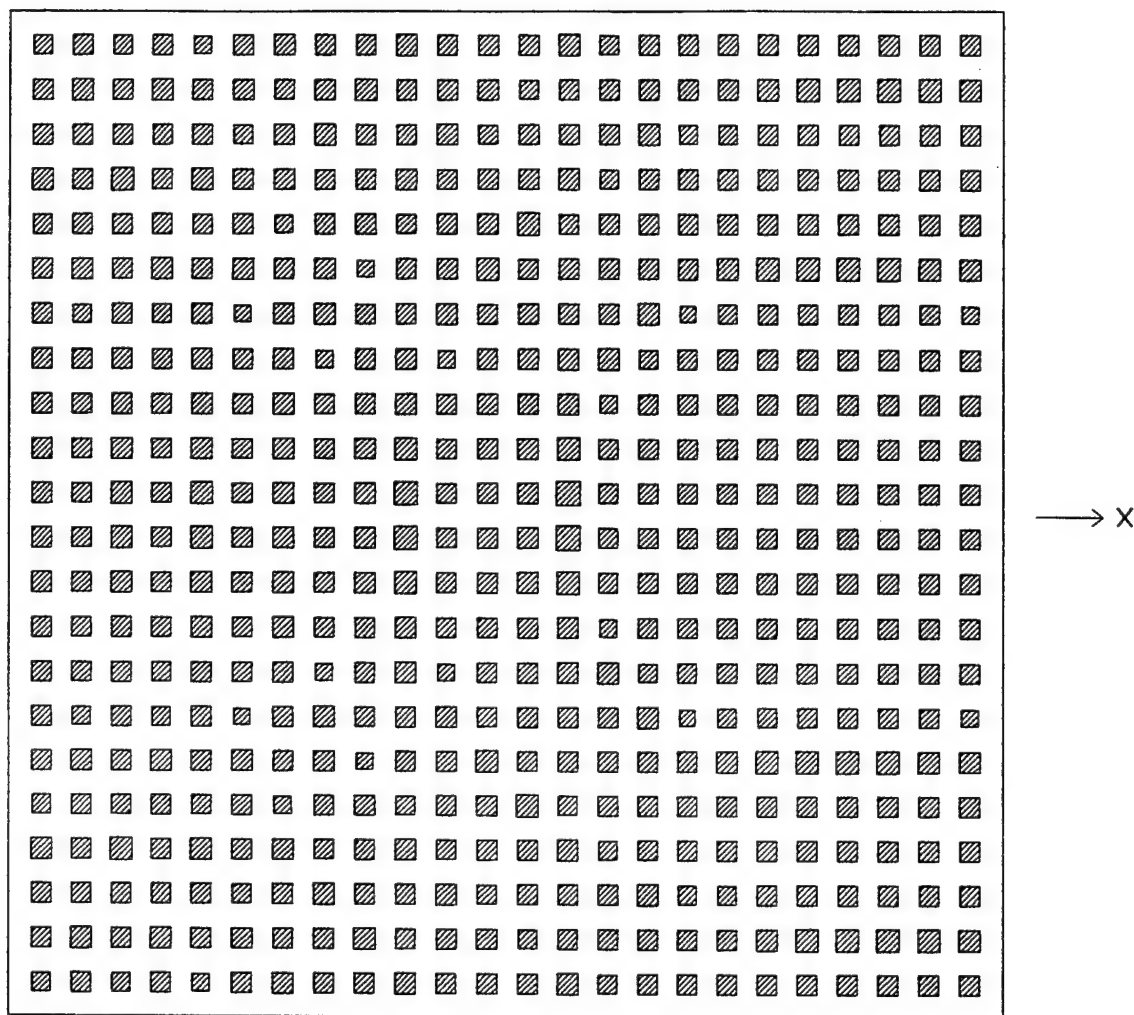


Figure 3.8. Scaled drawing of reflectarray design example #2.

13 over that of design example #1, thereby greatly increasing the potential random phase error that can result from errors in fabrication.

Computed and measured E-plane radiation patterns taken at the center-band frequency of 27.3 GHz are shown in Figure 3.9, and similar H-plane patterns are shown in Figure 3.10. This center frequency is also slightly lower than the design frequency of 28 GHz due to the fact that the design was performed before the edge mode of Section 2.2.1 was introduced into the program and that inspection underneath a microscope found the patches to be underetched by an average of 0.002". Use of one entire domain mode and one edge condition mode as described in Section 2.2.1 predicts a center frequency of 27.7 GHz, which is a 1% shift from the original design frequency. Examination of the radiation patterns again shows a very good comparison of measured and computed results similar to those of design example #1. The H-plane patterns are in very close agreement, while the measured sidelobe level and 3dB beamwidth are again slightly higher in the E-plane, possibly due to aperture blockage or phase errors not included in the analysis. Measured and computed patterns for frequencies other than 27.3 GHz exhibit the same behavior as those of design example #1 with a rise in specular reflection and beam squint with frequency, which are characteristics of all prime focus fed microstrip reflectarrays with beams scanned off broadside.

A gain-loss budget for this reflectarray at the center frequency is shown in Table 3.4. Measured gain at 27.3 GHz was 28.5 dBi, yielding an aperture efficiency of 35%. The computed gain of 29.52 dBi is 1dB greater than the measured gain; the difference can be explained by directivity loss due to random phase errors incurred during fabrication. A great deal of ohmic loss occurs because of the high loss tangent of the material, and this decreases the aperture efficiency significantly. This reasoning was verified by changing the substrate material in example #3.

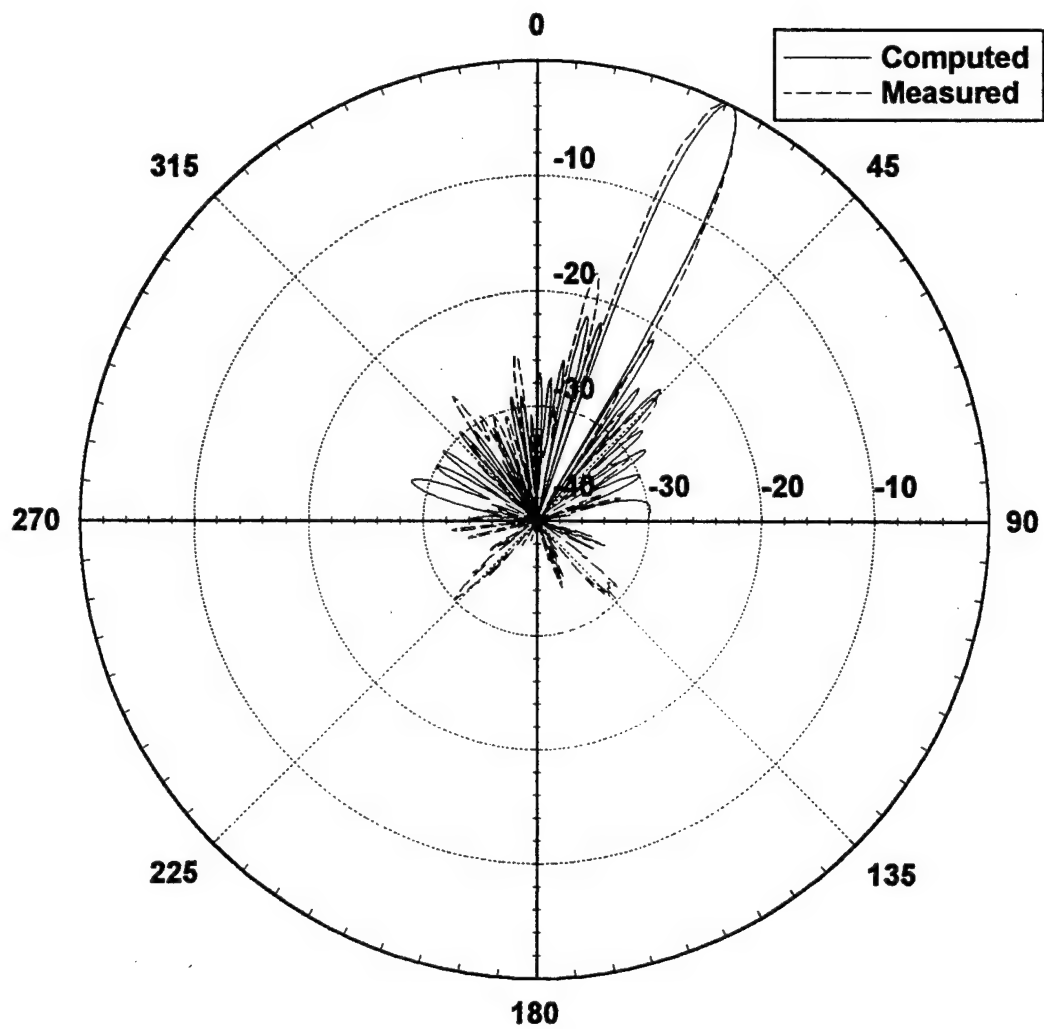


Figure 3.9. Measured and computed E-plane radiation patterns at 27.3 GHz for design example #2.

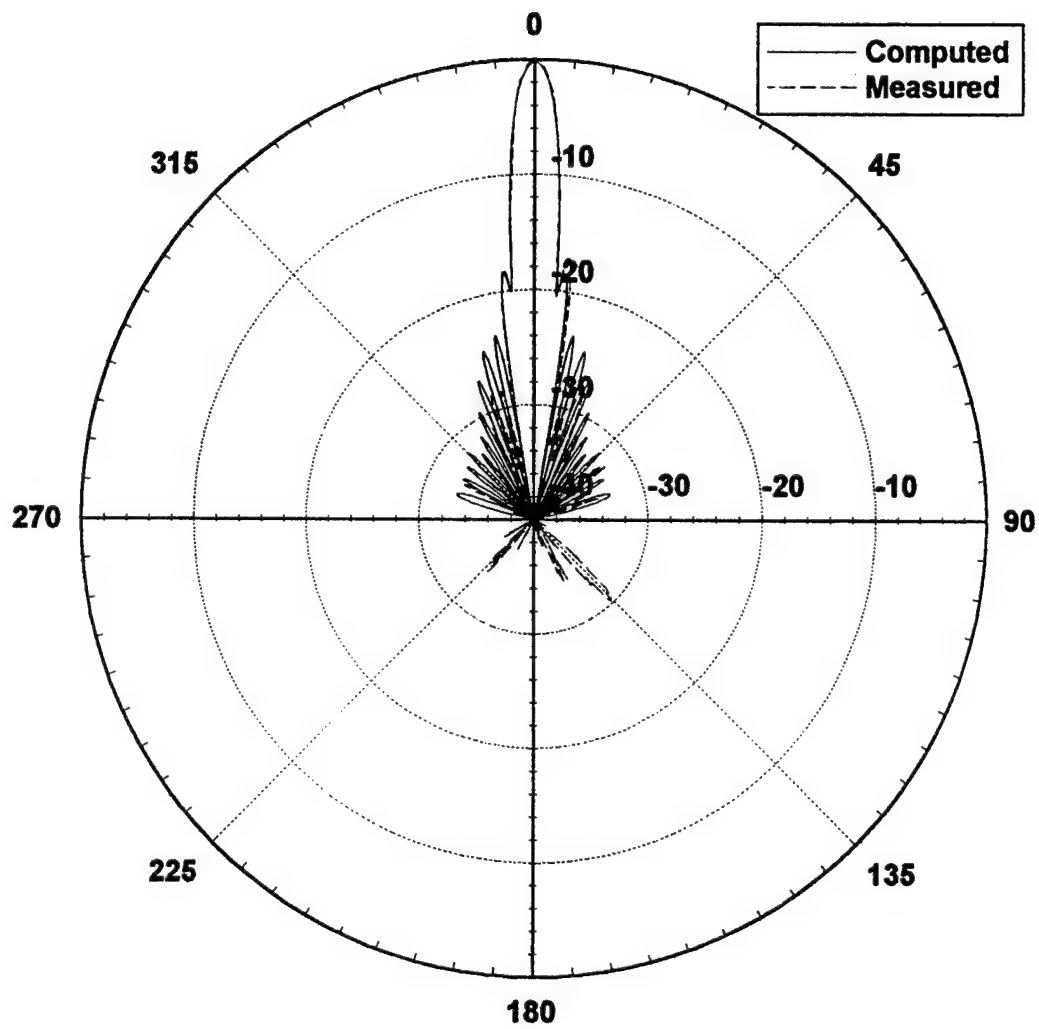


Figure 3.10. Measured and computed H-plane radiation patterns at 27.3 GHz for design example #2.

A plot of computed and measured gain is shown in Figure 3.11. The computed levels are again slightly higher for most frequencies, since the effect of random phase errors due to fabrication is not included. The bandwidth for a 1dB drop in gain compares well; a bandwidth of 2.3% is calculated, while a 2.7% bandwidth was measured. Taking into account a possible gain measurement error of ± 0.5 dB, a computed bandwidth between 1.5% and 2.8% is within the limits of measurement error.

Table 3.4. Gain-loss budget for reflectarray #2.

Maximum Directivity	33.48 dBi
Spillover Loss	-0.74 dB
Taper Loss	-0.61 dB
Cos θ Scan Loss	-0.43 dB
Dielectric and Conductor Loss	-2.03 dB
Design Phase Error	-0.15 dB
Computed Gain	29.52 dBi

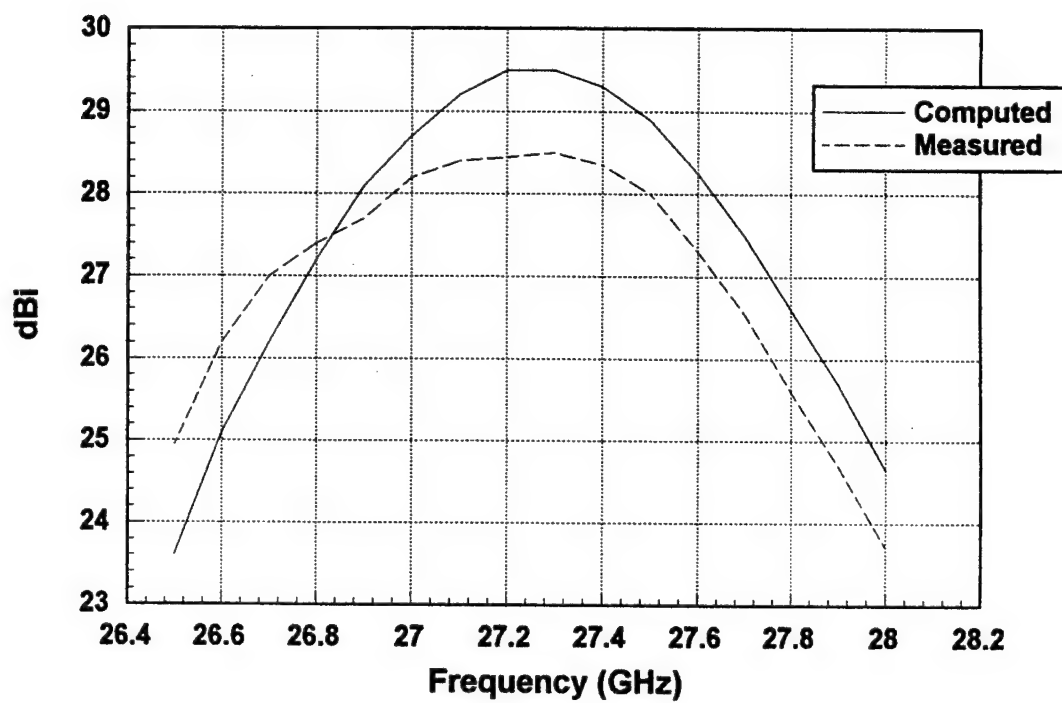


Figure 3.11 Measured and computed gain for reflectarray design example #2.

3.4 Microstrip Reflectarray Design Example #3

Design example #3 was a Ka-band reflectarray with a center operating frequency of 28.5 GHz, similar to example #2. The motivation behind this design was to increase the aperture efficiency of the previous design by trying to reduce the dielectric losses and amount of phase error contributed from fabrication errors. To accomplish this, a thicker substrate with lower dielectric constant and a lower loss tangent was used for the design. This decreases both the dielectric loss and the slope of the linear region of the reflection phase curve, thereby increasing the bandwidth of the patch elements and minimizing the effects of etching errors. The efficiency due to dielectric loss is significantly improved.

A scaled drawing of this reflectarray is shown in Figure 3.12. This design was constructed on a 20 mil thick Rogers 5880 Duroid substrate, with a relative permittivity of 2.2. The loss tangent of the material was estimated to be 0.0028 at 28 GHz, compared to the value of 0.0074 for the Taconic material used in example #2. The reflectarray measured 6"x6", and a rectangular grid spacing was employed with $a=b=0.5442\text{cm}$. This grid spacing allowed for the azimuth angle to be taken into account in the analysis without the appearance of grating lobes for the infinite array. The design consisted of 784 square patches of varying length. The same feed horn and f/D ratio from design example #2 was used, and the main beam was scanned to 25° off broadside in the E-plane.

The curve of total reflection phase versus patch length for this design for broadside incidence yields the slope of the linear region to be $12^\circ/\text{mil}$ and a 34° region of phases that cannot be attained. The slope of the linear region is decreased by almost a factor of 4 over that of design example #2, but the range of phases that cannot be obtained was increased by more than a factor of 2. This decreases the potential random phase error that can result from errors in fabrication, but increases the amount of phase error that is inherent in the

design. Radiation patterns for this example were similar to those of design example #2, and are not included here.

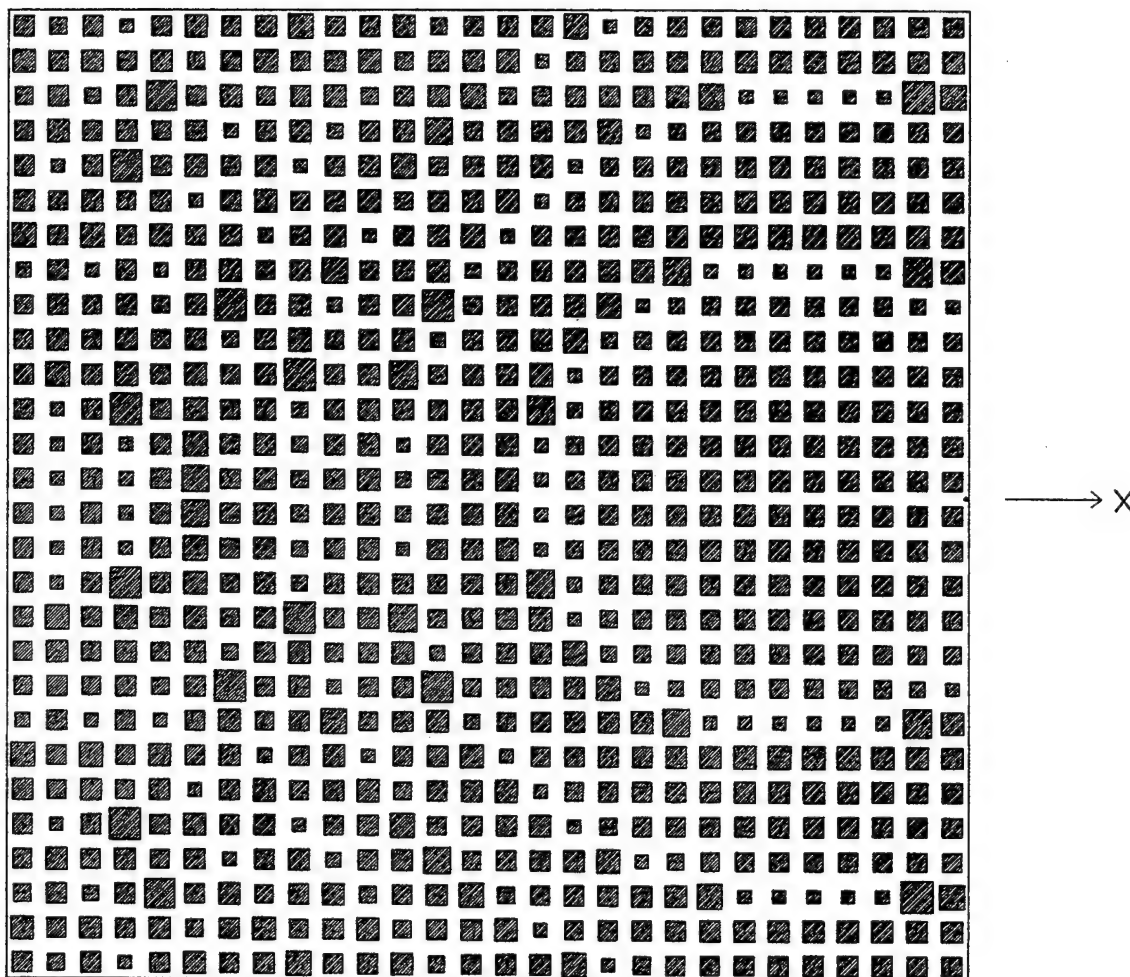


Figure 3.12. Scaled drawing of reflectarray design example #3.

A gain-loss budget for this reflectarray at the center frequency is shown in Table 3.5. Measured gain at 28.5 GHz was 30.9 dBi, yielding an aperture efficiency of 52% - a 17% increase over the previous design. The maximum computed gain of 31.68 dBi is 0.8dB greater than the measured gain. Comparison to the 1 dB difference of the previous design suggests a decrease in sensitivity to fabrication tolerances, however, the closer element spacing in this design has the potential to increase phase errors due to mutual coupling. Also, ohmic losses in this design were reduced by 1.78 dB through the choice of dielectric material. Phase errors inherent in the design were increased only by 0.07 dB.

A plot of computed and measured gain is shown in Figure 3.13. There is a 1.8% frequency shift between the peak gain for the computed and measured results. The bandwidth for a 1dB drop in gain has increased over design #2; a bandwidth of 6.1% is calculated, while a 4.9% bandwidth was measured. Taking into account a possible gain measurement error of ± 0.5 dB, a computed bandwidth between 2.5% and 6.1% is within the limits of measurement error.

Table 3.5. Gain-loss budget for reflectarray #3.

Maximum Directivity	34.05 dBi
Spillover Loss	-0.75 dB
Taper Loss	-0.72 dB
Cos θ Scan Loss	-0.43 dB
Dielectric and Conductor Loss	-0.25 dB
Design Phase Error	-0.22 dB
Computed Gain	31.68 dBi

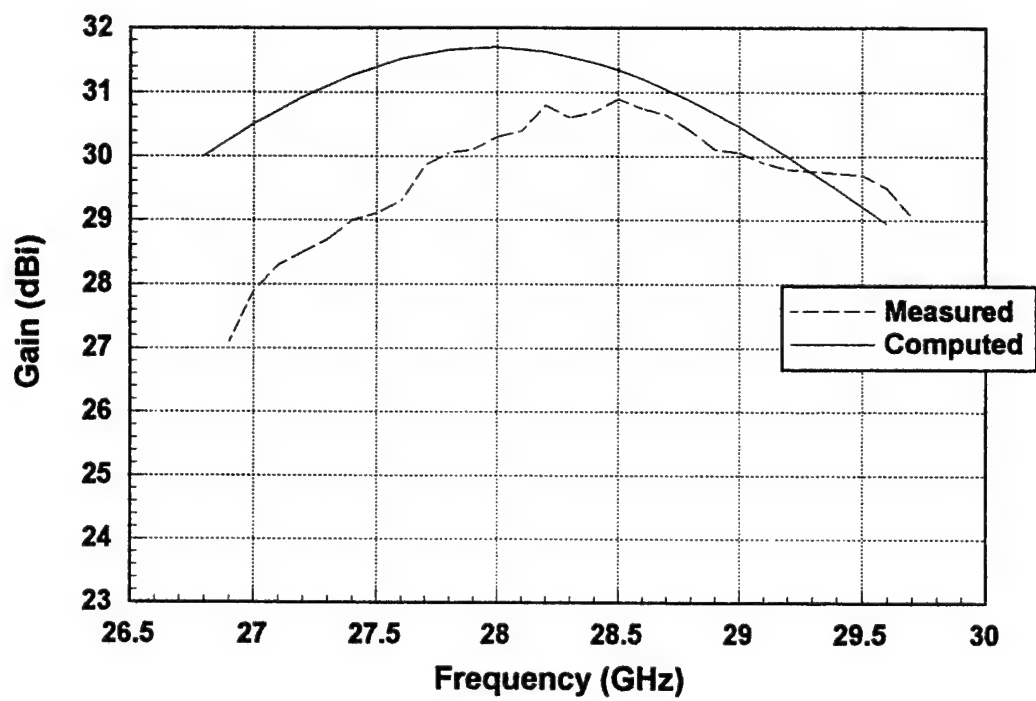


Figure 3.13. Measured and computed gain for reflectarray design example #3

3.5 Microstrip Reflectarray Design Example #4

Design example #4 was a circular shaped Ka-band reflectarray operating around 27-28 GHz. The motivation behind this design was to incorporate a backfire feed [21] into the design and to compare the performance of a circular aperture microstrip reflectarray with a similarly sized parabolic dish.

A scale drawing of this reflectarray is shown in Figure 3.14. This design was constructed on the same Taconic material as was used for design example #2. The reflectarray had a 9" diameter, and a rectangular grid spacing was employed with $a=0.56\text{cm}$ and $b=0.6667\text{cm}$. The design consisted of 996 rectangular patches of varying length and a fixed width of 0.4cm, and the center four patches are left out in order to leave room for the circular waveguide section for the feed. Analyzing the reflection phase versus patch length curves for this design yields the slope of the linear region to be $37^\circ/\text{mil}$ and a 16.6° region of phases that cannot be attained. The slope of the linear region is slightly decreased from that of design example #2 due to the fact that the fixed-width patches exhibit slightly larger bandwidth. The phase center of the feed element was placed 7.54cm above the face of the reflectarray, giving an f/D ratio of 0.33. The aperture phase was tailored to produce a broadside beam.

The feed element is shown in Figure 3.15. A section of circular waveguide leads into a dielectric (Rexolite) cone which is metallized with a splash plate. Measured E-plane and H-plane patterns for this feed are shown in Figures 3.16 and 3.17, respectively. To perform these measurements, the feed element was placed in front of a large ground plane and the resulting reflection off of the ground plane was measured. A great deal of ripple is present in the measured patterns, possibly due to diffraction effects from the edge of the splash plate and ground plane. Since a computer model for this type of feed was not

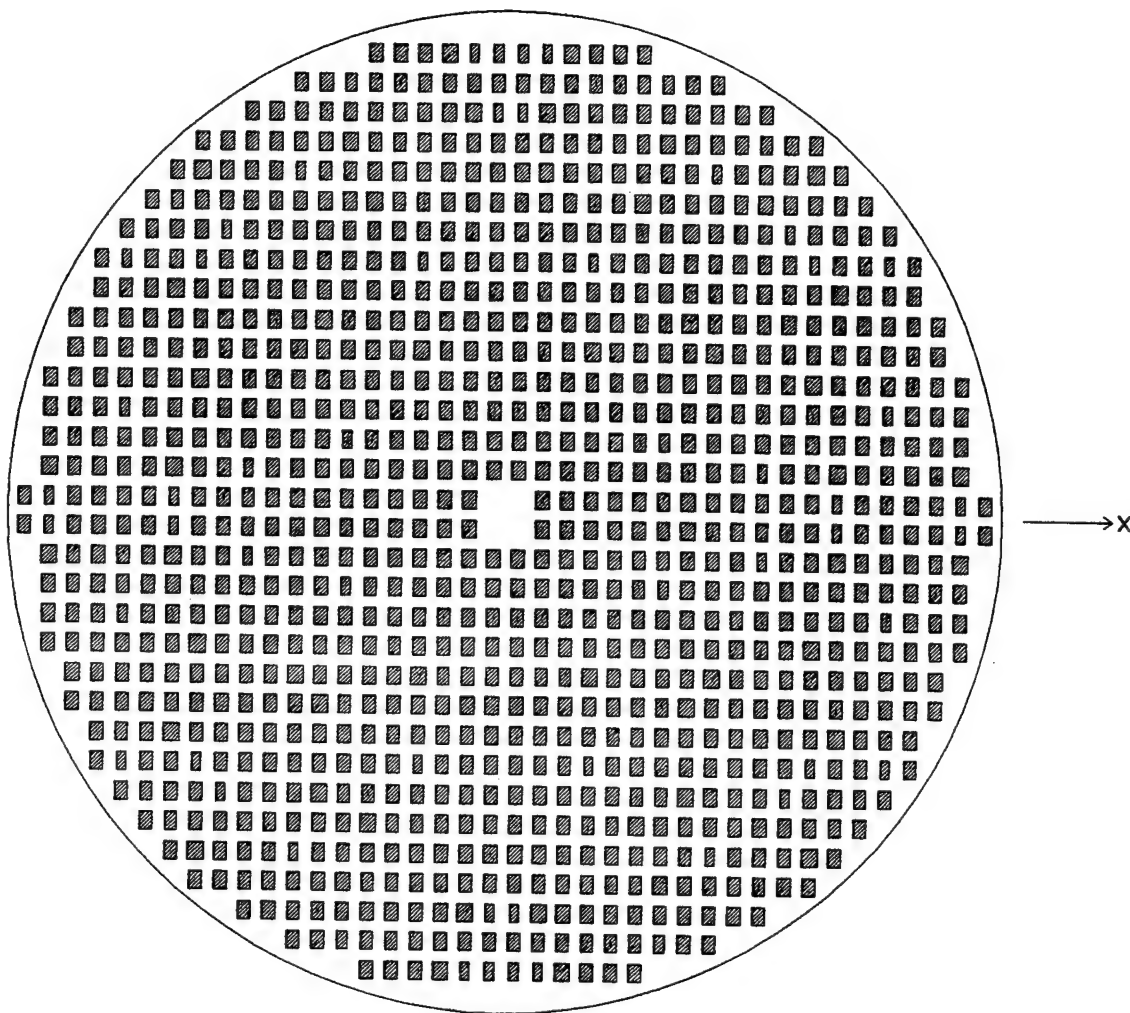


Figure 3.14. Scaled drawing of reflectarray design example #4.

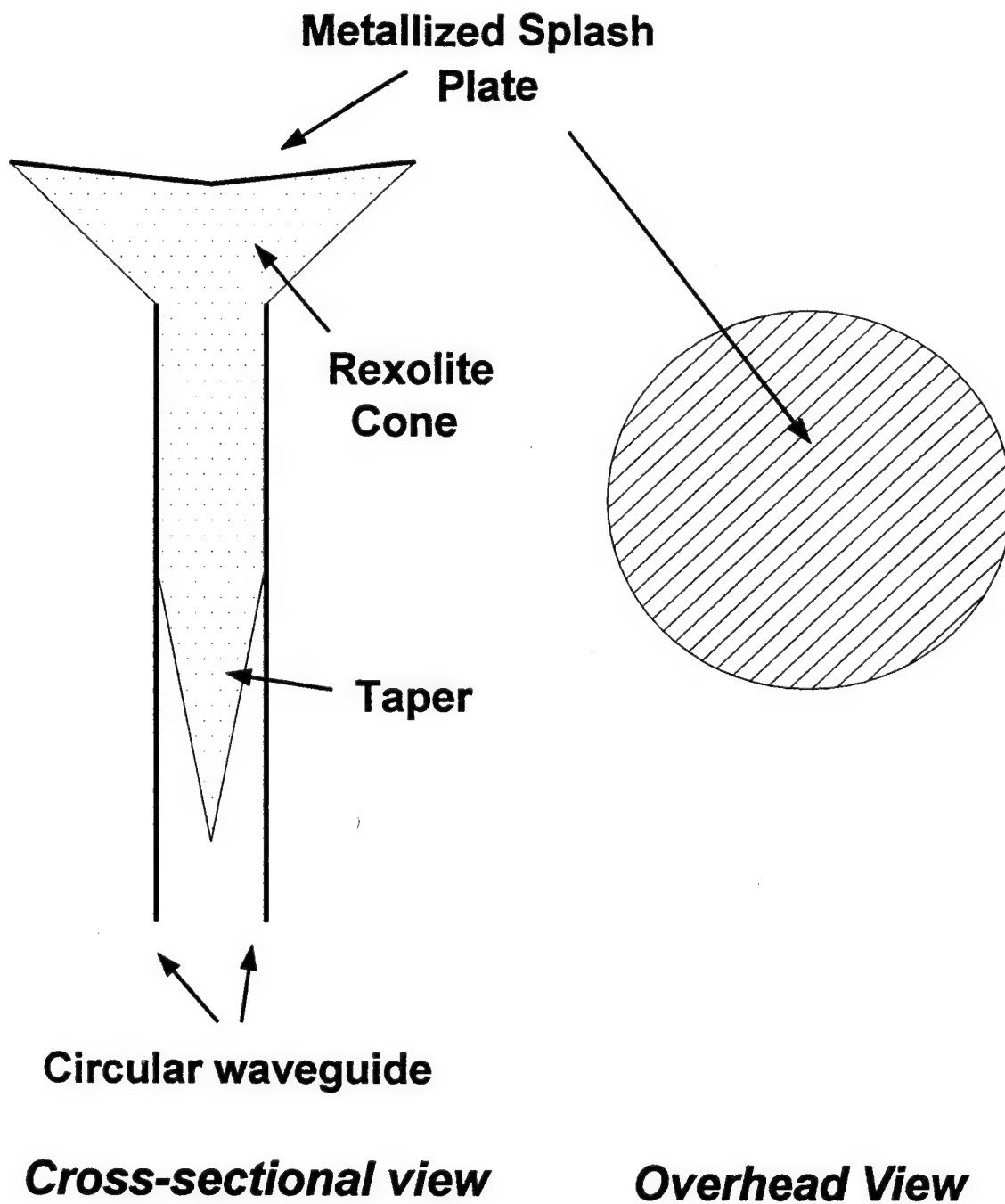


Figure 3.15. Backfire feed used in reflectarray design example #4.

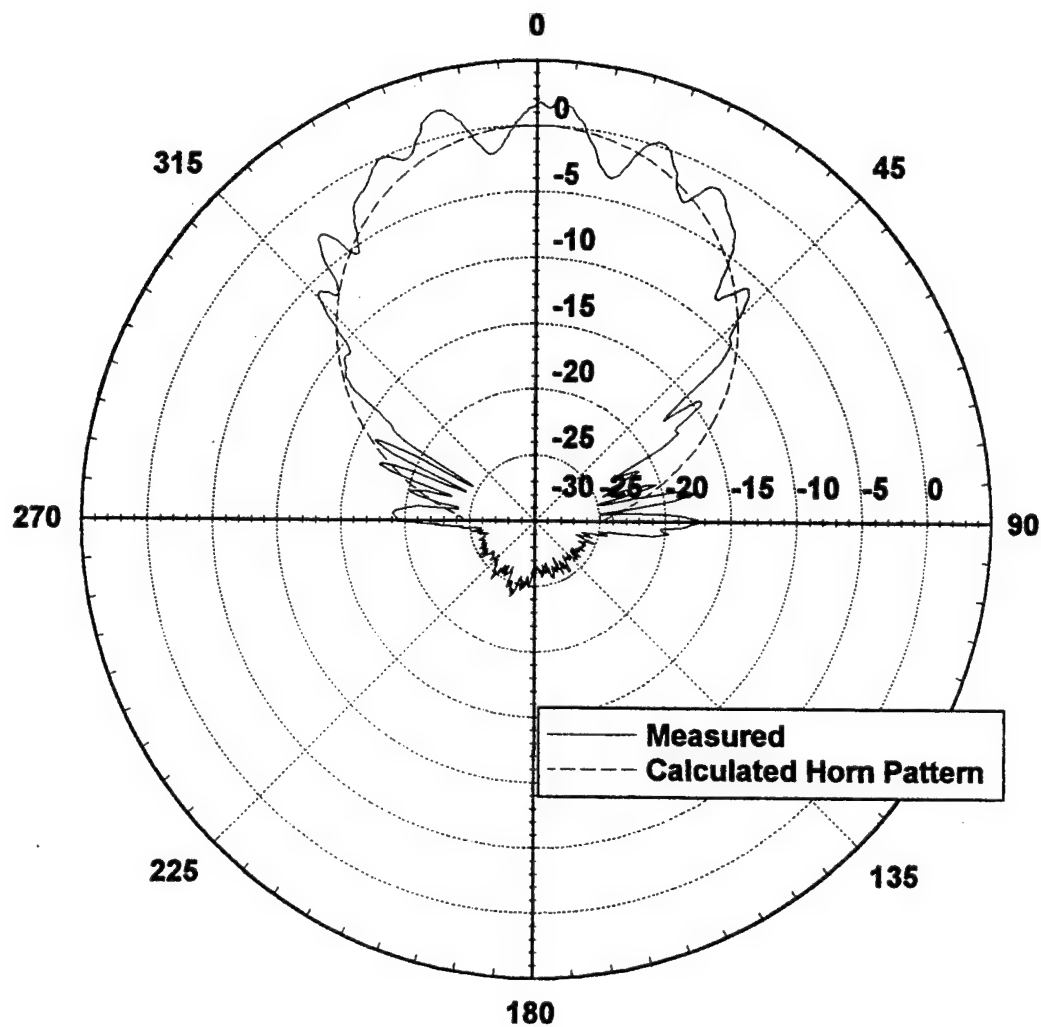


Figure 3.16. Measured E-plane pattern from backfire feed and computed pattern from pyramidal horn used to model feed. Frequency = 27 GHz.

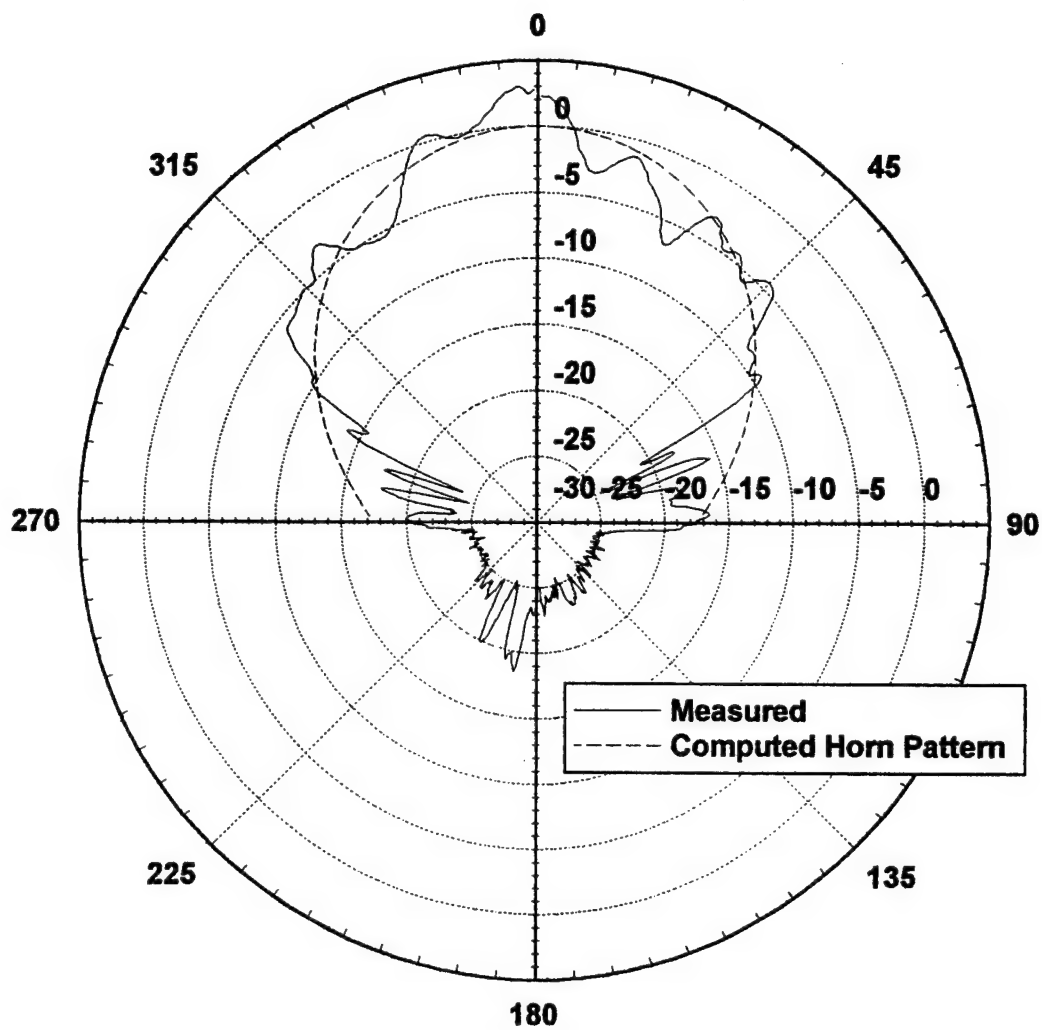


Figure 3.17. Measured H-plane pattern from backfire feed and computed pattern from pyramidal horn used to model feed. Frequency = 27 GHz.

available, a pyramidal horn with an H-plane aperture dimension of 1.2cm, an E-plane dimension of 1.0cm, and an axial length of 4cm was used to model the feed illumination. Computed E-plane and H-plane patterns for this horn are shown along with the measured patterns in Figures 3.16 and 3.17.

Computed and measured E-plane radiation patterns taken at 27.3 GHz from the reflectarray are shown in Figure 3.18, and similar H-plane patterns are shown in Figure 3.19. Examination of the measured and computed patterns shows a slightly smaller measured beamwidth in the E-plane and slightly larger measured beamwidth in the H-plane. This difference is most likely due to the approximate model used for the feed illumination. Also, measured sidelobe levels are higher in the E-plane, which could be a sign of phase error.

A gain-loss budget for this reflectarray at the center frequency is shown in Table 3.6. A peak measured gain of 31.2 dBi occurred at 27.2 GHz, yielding an aperture efficiency of 34%. This low value is not totally unexpected, based on the results of example #2 which used the same Taconic substrate. Ohmic losses in this design were reduced by approximately 0.5dB over design example #2 due to the fact that the wider patches exhibit lower loss. Taper loss is quite high, and could possibly be minimized through optimization of the feed. Phase errors inherent in the design were quite large due to the increased dependence on azimuth incidence angle for designs with a low f/D ratio. This dependence was not taken into account in the design process, since an early version of the design program which did not include this effect was used.

A plot of measured gain versus frequency is shown in Figure 3.20. The phase center of the feed element moves with frequency, making the bandwidth of the feed the limiting factor for gain bandwidth. This effect is seen by changing the positioning of the

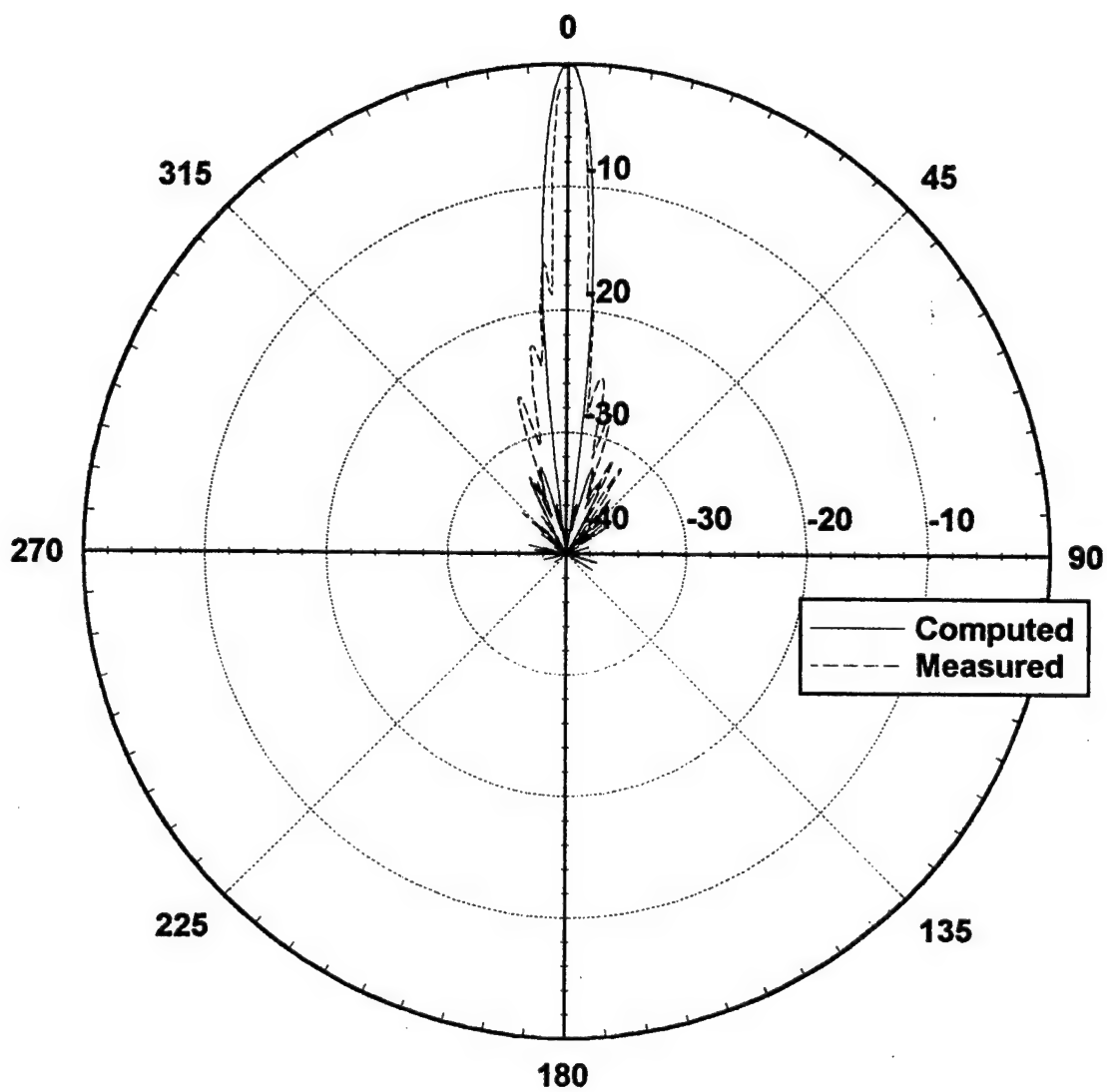


Figure 3.18. Measured and computed E-plane radiation patterns at 27.3 GHz for reflectarray #4.

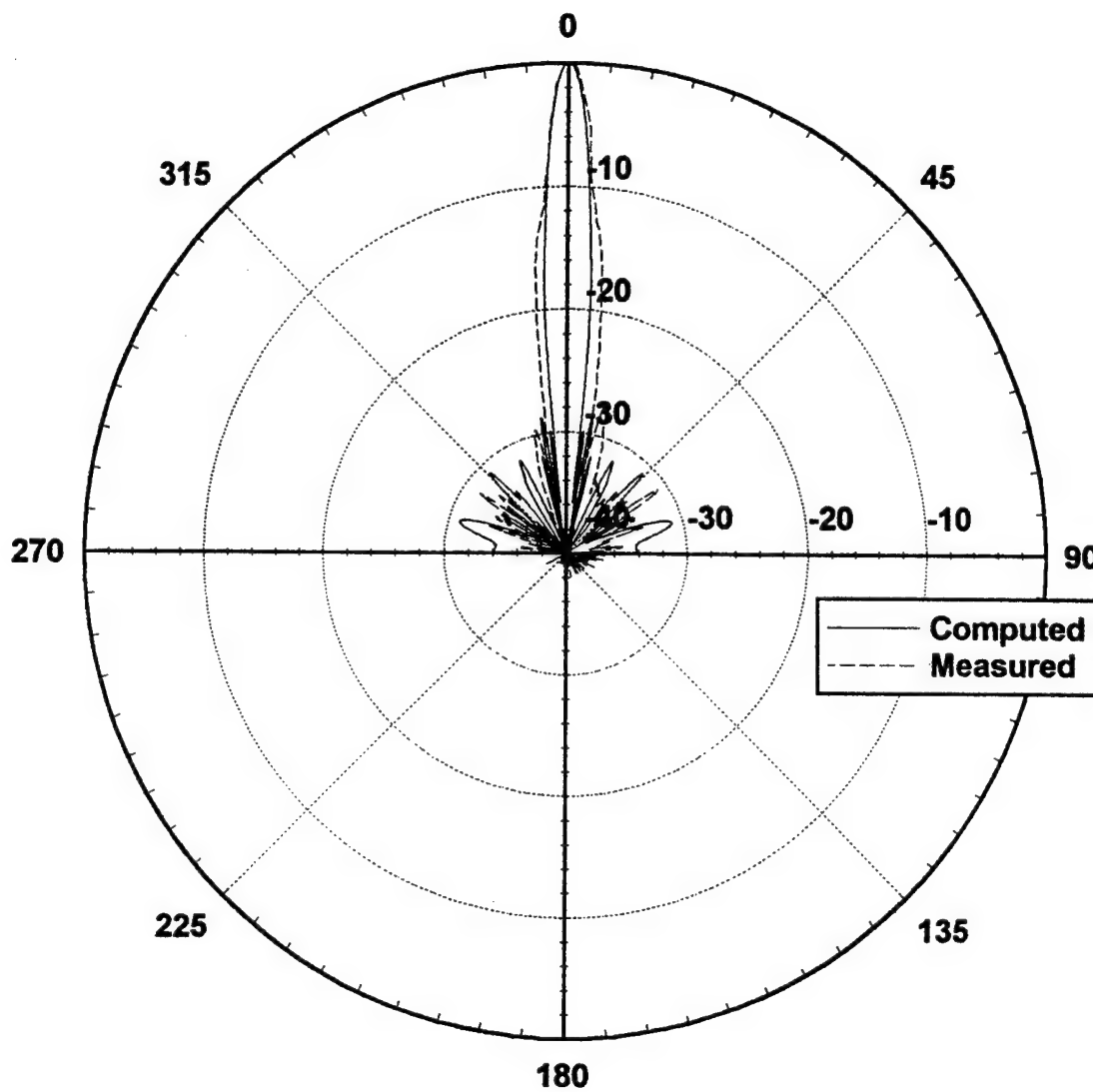


Figure 3.19. Measured and computed H-plane radiation patterns at 27.3 GHz for reflectarray #4.

feed element - by adjusting the height of the feed over the face of the reflectarray, the frequency at which the peak gain occurs is changed. This is seen in Figure 3.20. For feed positioning #1, a peak gain of 31.2 dBi occurs at 27.2 GHz, and for feed positioning #2 a peak gain of 30.8 dBi occurs at 27.6 GHz. The measured bandwidth for a 1dB drop in gain is 1.8% in both cases, while a bandwidth of 2.9% is calculated with the pyramidal horn feed.

Table 3.6. Gain-loss budget for reflectarray #4.

Maximum Directivity	35.91 dBi
Spillover Loss	-0.46 dB
Taper Loss	-1.12 dB
Dielectric and Conductor Loss	-1.51 dB
Design Phase Error	-0.87 dB
Computed Gain	31.95 dBi
Measured Gain	31.2 dBi

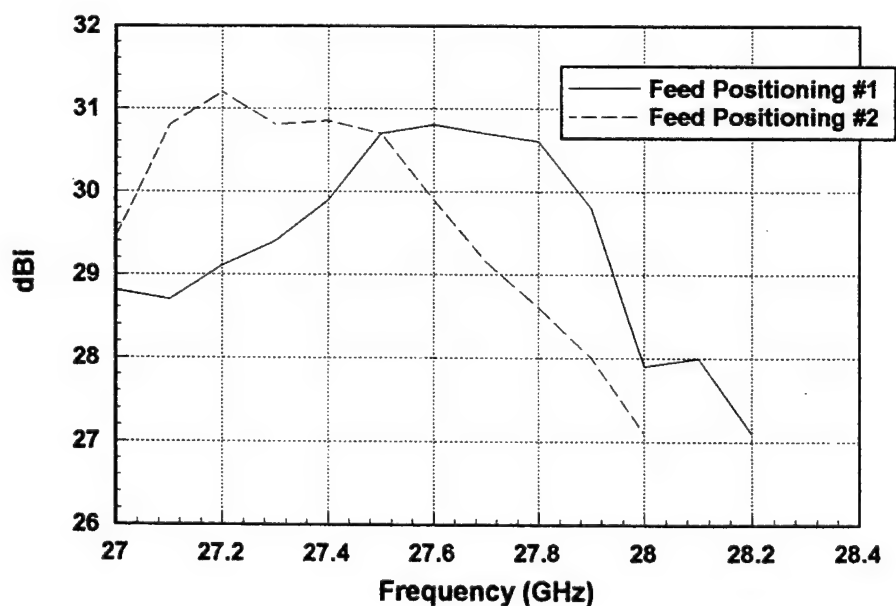


Figure 3.20. Measured gain for reflectarray design example #4.

The gain performance of this reflectarray was also compared with that of a parabolic reflector. The parabolic reflector was constructed from metallized plastic with a 9" diameter and an f/D ratio of 0.44, which produced a total subtended angle for the feed of 118° as compared to 113° for the reflectarray. These two values were close enough to give a one-on-one comparison of the gain performance of each antenna.

To model the feed illumination of the reflector the same pyramidal horn used for modeling the reflectarray was employed. A gain-loss budget for the parabolic dish at 27.3 GHz is shown in Table 3.7. The maximum directivity for the dish is slightly higher than that of the reflectarray since the value for the reflectarray only includes the area occupied by the unit cells in the array. This model does not account for different phase centers in the principal planes for the feed, so the measured gain is expected to be decreased by this phase error. Also, losses due to surface roughness of the dish are not included. These two factors can explain the 1dB difference in measured and computed gain.

Comparing the gain of the dish and reflectarray shows that the measured gain for the dish was 2.3 dB higher than for the reflectarray. Computed gain for the dish was 2.5 dB higher than the computed gain for the reflectarray, showing an excellent comparison between computed and measured results in this sense. The 2.5 dB difference between computed values is due almost totally to ohmic losses and phase errors present in the design, which could be minimized by approximately 2 dB through a change in the design process and the substrate material used.

The difference between measured and computed gain values for both antennas are also close (1.0 dB difference for the dish, 0.75 dB difference for the reflectarray). Since the same feed was used for both cases, this result implies that the effects of fabrication

errors - rms surface roughness for the dish and etching & substrate tolerances for the reflectarray - on the gain of the antenna are not much different for both antennas.

Table 3.7. Gain-loss budget for 9" diameter parabolic reflector.

Maximum Directivity	36.29 dBi
Spillover Loss	-0.39 dB
Taper Loss	-1.45 dB
Computed Gain	34.45 dBi
Measured Gain	33.5 dBi

3.6 Microstrip Reflectarray Design Example #5

Design example #5 was a 6" square W-band reflectarray with a design frequency of 76.5 GHz. The motivation behind this design was similar to the motivation behind the previous designs - to see if the microstrip reflectarray concept is feasible at this high frequency and to quantify sources of loss in the reflectarray. Also, sets of phase versus patch length data were computed for azimuth incidence angles of 0, 45, and 90 degrees. Each set of data contained curves for elevation incidence angles from 0 to 60 degrees in increments of 5 degrees. The azimuth incidence angle was taken into account in the design process by linearly interpolating in between the different sets of data.

A scale drawing of this reflectarray is shown in Figure 3.21. This design was constructed on a 0.005" thick Rogers Duroid 5880 substrate. The estimated loss tangent was 0.0077 at 76.5 GHz. The reflectarray measured 6" on each side, and a rectangular grid spacing was employed with $a = b = 0.2005\text{cm}$. The design consisted of 5776 rectangular patches of varying length and a fixed width of 0.135cm. Analyzing the

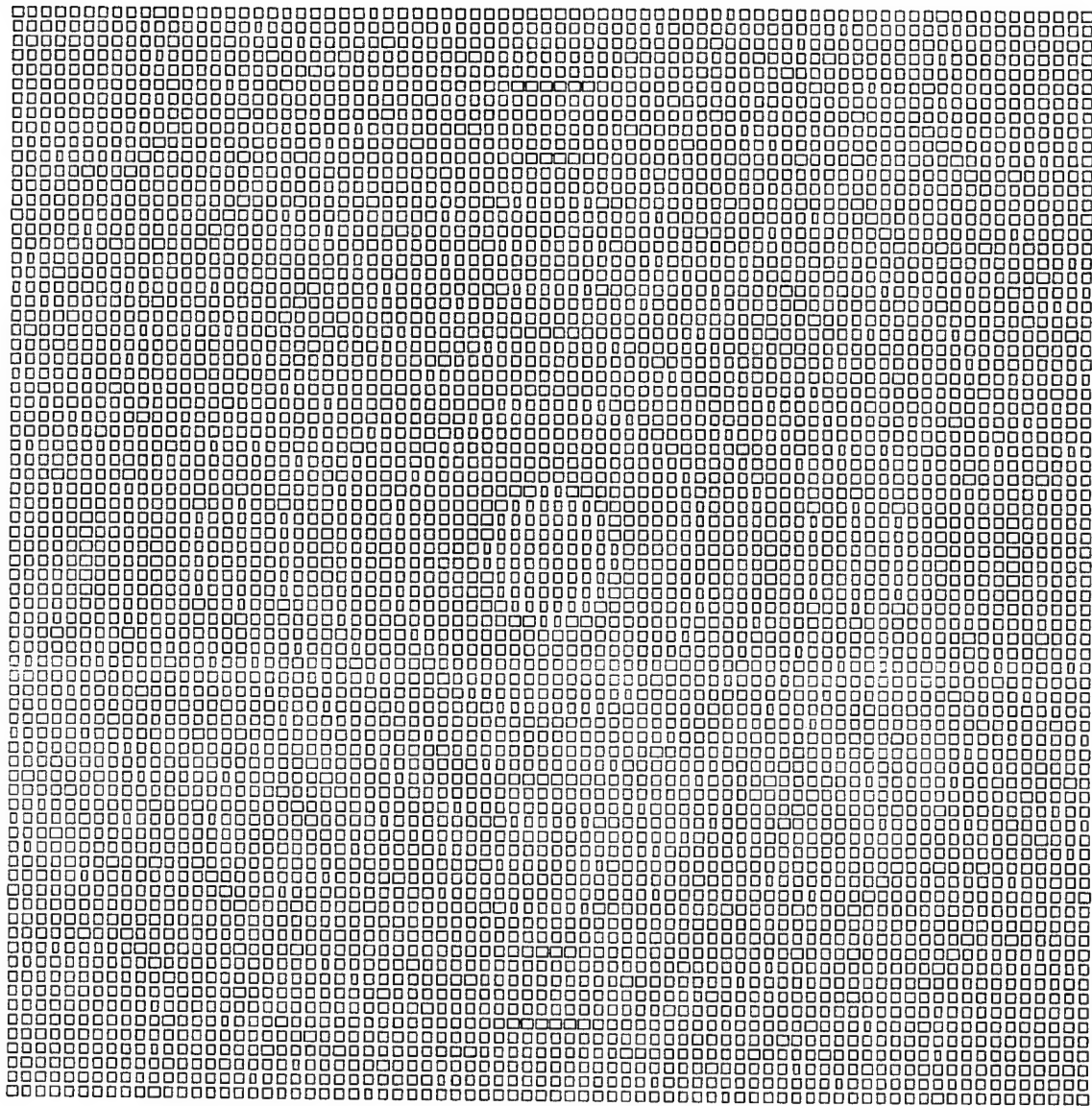


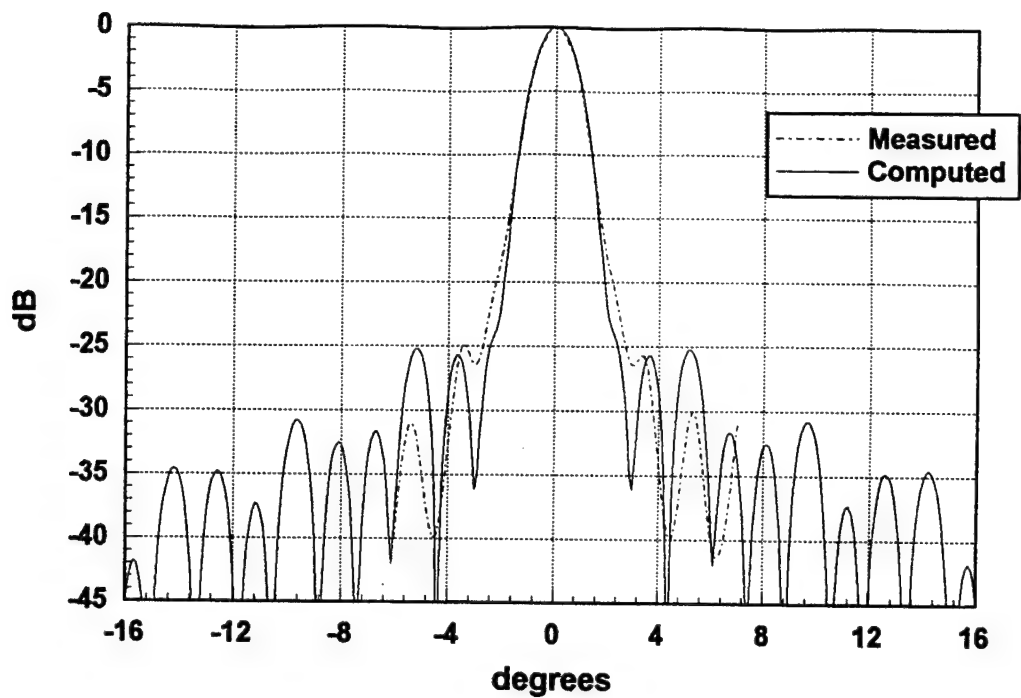
Figure 3.21. Actual size overhead drawing of reflectarray design example #5.

reflection phase versus patch length curves for this design yields the slope of the linear region to be $49^\circ/\text{mil}$ and a 23.3° region of phases that cannot be attained. The feed element was an open-ended section of W-band waveguide that was slightly flared to give a 0.3cm square aperture. The phase center of the feed was placed 5.03cm above the face of the reflectarray, giving an f/D ratio of 0.33. The aperture phase of the reflectarray was tailored to produce a broadside beam.

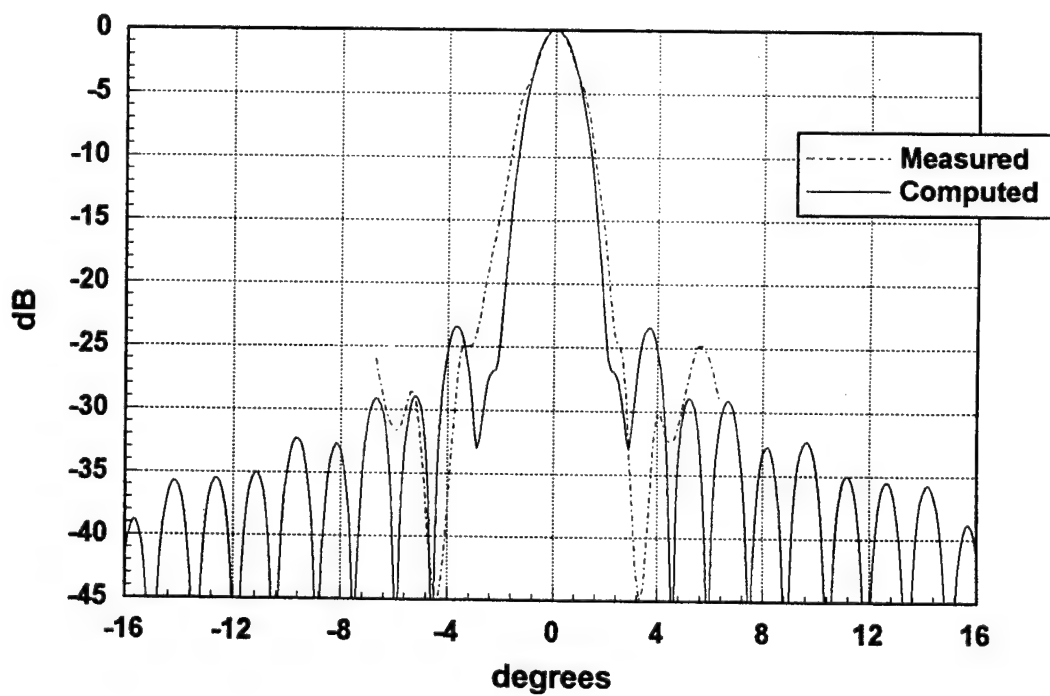
Computed and measured E-plane radiation patterns taken at 75 GHz are shown in Figure 3.22a, and H-plane patterns are shown in Figure 3.22b. Examination of the measured and computed patterns show that the measured and computed beamwidths in the E-plane and H-plane are nearly equal. Measured sidelobes are somewhat higher than computed, which is most likely due to phase errors incurred by fabrication errors.

A gain-loss budget for this reflectarray at the center frequency is shown in Table 3.8. A peak measured gain of 36.0 dBi occurred at 74.5 GHz, yielding an aperture efficiency of 22%. Ohmic losses in this design were not too great, showing that the Rogers substrate has reasonable loss characteristics even at W-band. Phase errors inherent in the design were diminished due to the azimuth interpolation included in the analysis.

A difference of about 3.5 dB remains between the measured and computed gain. This difference could result from many factors which are negligible at lower frequencies but could become a factor at W-band. Loss in the long waveguide section of the feed, errors due to the reflectarray surface not being perfectly flat, and slight positioning errors for the feed can all decrease the overall gain of the reflectarray. Unfortunately, only very limited measurements were able to be taken since they were performed at an outside facility.



(a)



(b)

Figure 3.22. Computed and measured radiation patterns for reflectarray #5. Measured patterns at 75 GHz; computed at 76.5 GHz. (a) E-plane. (b) H-plane.

Table 3.8. Gain-loss budget for reflectarray #5.

Maximum Directivity	42.55 dBi
Spillover Loss	-0.85 dB
Taper Loss	-0.96 dB
Dielectric and Conductor Loss	-1.13 dB
Design Phase Error	-0.08 dB
Computed Gain	39.53 dBi
Measured Gain	36.0 dBi

3.7 Microstrip Reflectarray Design Example #6

Design example #6 was a square W-band reflectarray with a design frequency of 76.5 GHz. The reflectarray itself was exactly the same as used in design #5, but the feed was changed to a cassegrain configuration. The geometry of the cassegrain feed is shown in Figure 3.23. The primary feed element was a conical horn with an aperture radius of 0.625cm and an axial length of 4cm. The subreflector shape was a hyperboloid in the x-z and y-z planes and circular with a radius of 0.762cm in the x-y plane. The virtual feed concept for a cassegrain reflector antenna [22] was used in the analysis.

Computed and measured E-plane radiation patterns taken at 76.5 GHz are shown in Figure 3.24a, and similar H-plane patterns are shown in Figure 3.24b. Examination of the measured and computed patterns show that the measured and computed beamwidths in the E-plane and H-plane are again nearly equal. The measured patterns shown for the cassegrain reflectarray exhibit better sidelobe levels and beam shape than the patterns for the prime focus case, however.

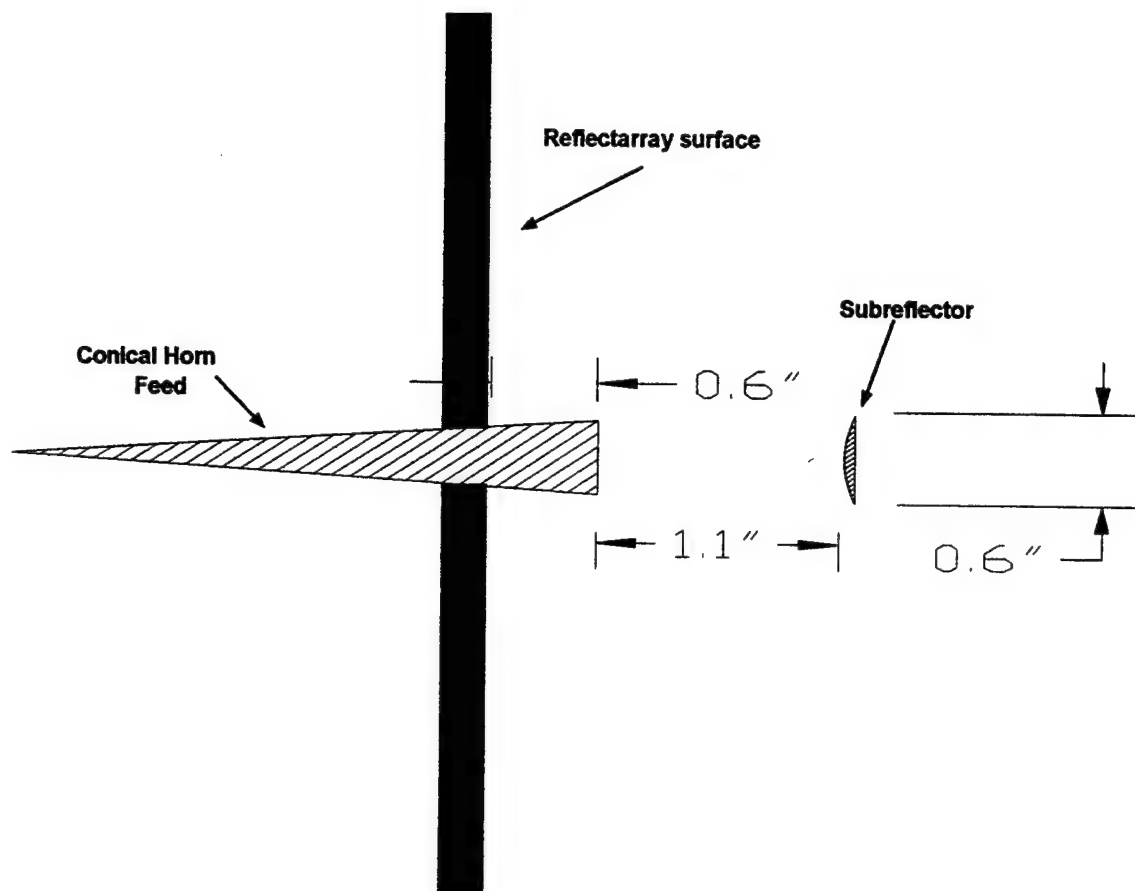
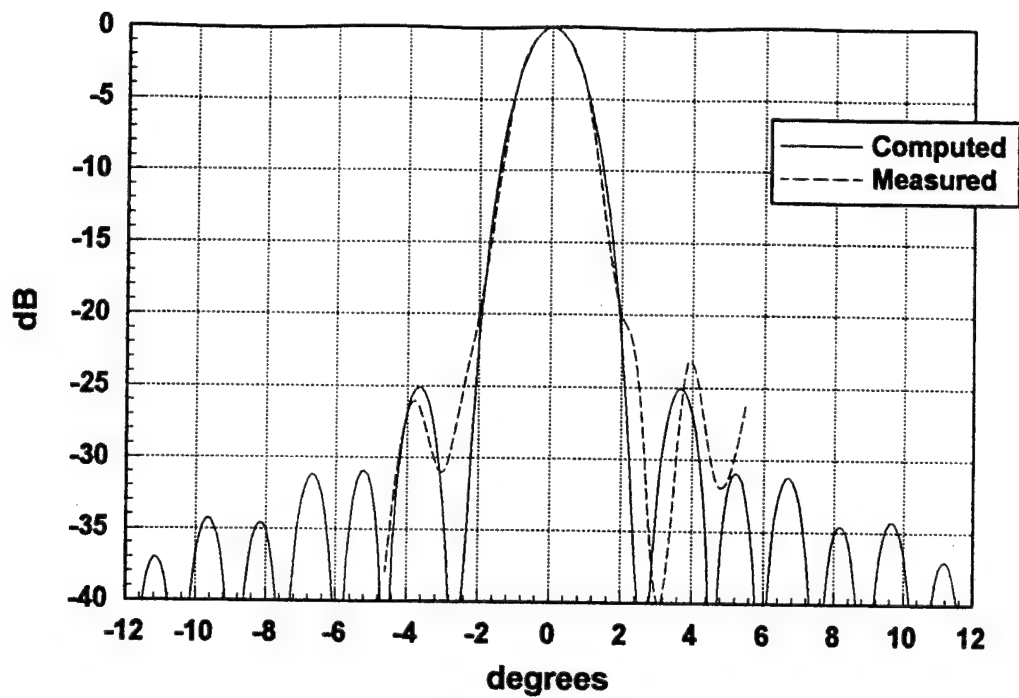
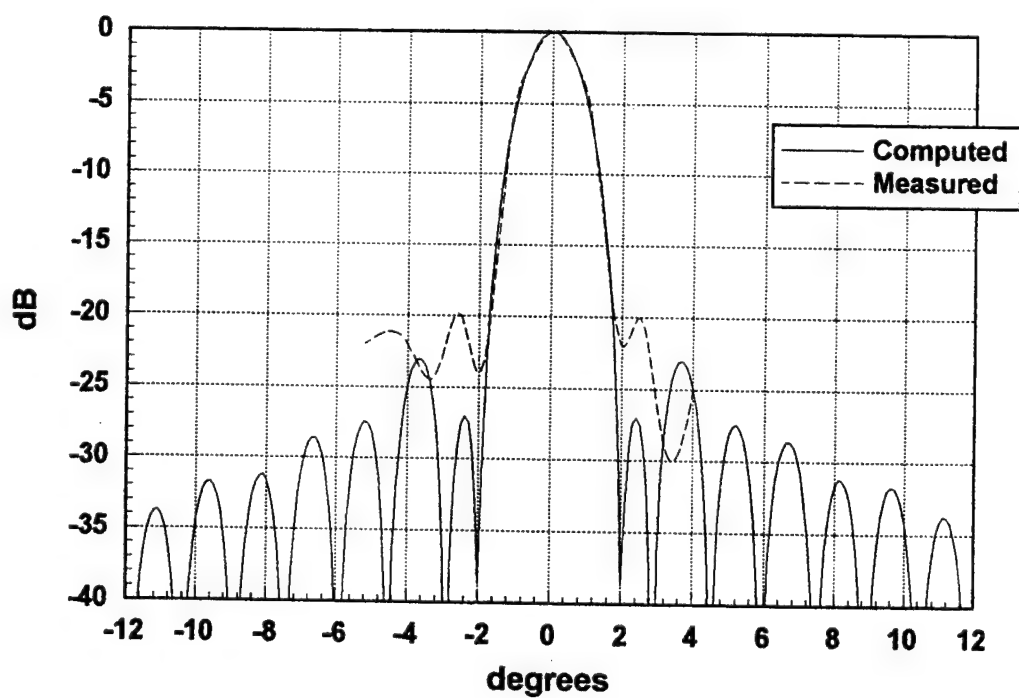


Figure 3.23. Geometry of cassegrain feed for reflectarray design example #6.



(a)



(b)

Figure 3.24. Measured and computed radiation patterns at 76.5 GHz for reflectarray #6. (a) E-plane. (b) H-plane.

A gain-loss budget for this reflectarray at the center frequency is shown in Table 3.9. A peak measured gain of 37.0 dBi occurred at 76.5 GHz, yielding an aperture efficiency of 26%. The spillover loss in this design is quite large due to a non-optimized feed and subreflector combination, i.e. the product of spillover and taper efficiency is not close to the maximum value of approximately 0.8. However, the measured gain is 1 dB higher than that of the prime focus fed reflectarray and the difference between computed and measured gain has been reduced to about 2 dB. These facts suggest that the former design may have suffered from more severe fabrication errors, a possible defocused feed, or higher than expected waveguide loss.

Table 3.9. Gain-loss budget for reflectarray #6.

Maximum Directivity	42.78 dBi
Spillover Loss	-1.55 dB
Taper Loss	-0.96 dB
Dielectric and Conductor Loss	-1.13 dB
Design Phase Error	-0.08 dB
Computed Gain	39.06 dBi
Measured Gain	37.0 dBi

CHAPTER 4

CONCLUSIONS

Two topics dealing with infinite arrays of microstrip elements were presented in this work. The first topic, the effect of random positioning errors on the input impedance of an infinite array of printed dipoles, deals mainly with the infinite array analysis, and provides insight into the scan blindness phenomenon for large arrays. The second topic, the analysis and design of microstrip reflectarrays, utilizes the data from the solution of plane wave scattering from an infinite array of microstrip patches to design a large, but finite sized, reflectarray.

In the first chapter, the solution for the expected value of input impedance for an infinite array of printed dipoles was presented, with both planar arrays and linear E-plane arrays being considered. The scan blindness phenomenon was seen to be reduced with the introduction of randomization, and to disappear completely only when the full extent of randomization was introduced. The limitation of a fixed terminal current on each dipole presents a formidable problem in implementing such a solution, however, such an implementation would have the added advantage of eliminating mutual coupling effects on the array pattern.

In the second chapter, topics in the analysis and design of microstrip reflectarrays are presented, with an added emphasis on reflectarrays operating in the millimeter wave frequency range. Problems such as loss and beam squint with frequency were analyzed, and options were presented so as to reduce the effects of both of these problems. Computational efficiency issues involving the infinite array scattering problem were also addressed, with a marked increase in efficiency resulting. The third chapter presented

measured results from six reflectarrays designed using the guidelines of the previous chapter.

The work presented here represents a step toward understanding the complex scattering mechanism of the microstrip reflectarray, especially at millimeter wave frequencies where ohmic losses and the potential for phase errors increase. However, in order to make the microstrip reflectarray a practical alternative for many applications where reflectors are normally used, much work still needs to be done.

A primary concern is the limited bandwidth of the microstrip reflectarray. This bandwidth is usually on the order of 3 to 5 percent, which is too small for many applications which employ reflector antennas. An increase in bandwidth may be achieved by using a thick foam substrate, with the use of thin dipoles for some elements to increase the range of reflection phases that may be achieved. A greater increase in bandwidth could possibly result from using stacked patches.

For shaped beam applications, a very precise knowledge of the total reflection phase from each element is needed. Therefore, in these applications, it would be beneficial to know the effect of mutual coupling in the reflectarray environment. Unfortunately, such a solution would involve a moment method computation for the entire reflectarray, which is computationally infeasible. A potential way around this problem would be to first design a reflectarray using the infinite array data and then perform three separate analyses for scattering from each element in the reflectarray - an analysis of the isolated element itself, a finite subarray composed of only the nearest neighbors to the element under analysis, and an infinite array of similar elements. Comparing the data from these solutions should give an idea as to the effect of mutual coupling on the reflection phase of each element in the reflectarray environment.

APPENDIX

GREEN'S FUNCTION FOR THE MICROSTRIP ELEMENT

Many calculations in this dissertation involve the use of the microstrip Green's function in the spectral domain. Expressions for this Green's function that are needed for calculations in the dissertation are presented here.

The dyadic spectral domain Green's function for the electric field at (x, y, d) of a single infinitesimal electric dipole located at (x_o, y_o, d) on a grounded dielectric slab is,

$$\overline{\overline{G}}(x, y | x_o, y_o) = -\frac{jZ_o}{4\pi^2 k_o} \int_{-\infty}^{\infty} \int_{-\infty}^{\infty} \overline{\overline{Q}}(k_x, k_y) e^{jk_x(x-x_o)} e^{jk_y(y-y_o)} dk_x dk_y \quad (A-1)$$

In this work we are only concerned with the tangential fields that produced by the currents on the surface described by $z=d$, i.e. the x and y directed electric fields due to the x and y directed currents.

The kernel functions for use in (A-1) are as follows:

For the x directed electric field produced by a x directed electric current:

$$Q_{xx} = \frac{(\epsilon_r k_o^2 - k_x^2) k_2 \cos(k_1 d) + j k_1 (k_o^2 - k_x^2) \sin(k_1 d)}{T_e T_m} \sin(k_1 d) \quad (A-2)$$

For the x directed electric field produced by a y directed electric current:

$$Q_{xy} = -\frac{k_x k_y [k_2 \cos(k_1 d) + j k_1 \sin(k_1 d)]}{T_e T_m} \sin(k_1 d) \quad (\text{A-3})$$

For the y directed electric field produced by a x directed electric current:

$$Q_{yx} = Q_{xy} \quad (\text{A-4})$$

For the y directed electric field produced by a y directed electric current:

$$Q_{yy} = \frac{(\epsilon_r k_o^2 - k_y^2) k_2 \cos(k_1 d) + j k_1 (k_o^2 - k_y^2) \sin(k_1 d)}{T_e T_m} \sin(k_1 d) \quad (\text{A-5})$$

In the above expressions:

$$k_1 = \sqrt{\epsilon_r k_o^2 - k_x^2 - k_y^2} \quad ; \quad \text{Im}(k_1) < 0 \quad (\text{A-6})$$

$$k_2 = \sqrt{k_o^2 - k_x^2 - k_y^2} \quad ; \quad \text{Im}(k_2) < 0 \quad (\text{A-7})$$

$$T_e = k_1 \cos(k_1 d) + j k_2 \sin(k_1 d) \quad (\text{A-8})$$

$$T_m = \epsilon_r k_2 \cos(k_1 d) + j k_1 \sin(k_1 d) \quad (\text{A-9})$$

BIBLIOGRAPHY

- [1] D.M. Pozar and D.H. Schaubert, "Scan Blindness in Infinite Phased Arrays of Printed Dipoles," *IEEE Transactions on Antennas and Propagation*, Vol. AP-32, pp. 602-610, Jun. 1984.
- [2] Y.T. Lo and V.D. Agrawal, "A Method for Removing Blindness in Phased Arrays", *Proc. IEEE(Lett.)*, vol. 56, pp. 1586-1588, Sep. 1968.
- [3] A.I. Zaghloul and R.H. MacPhie, "On the Removal of Blindness in Phased Antenna Arrays by Element Positioning Errors", *IEEE Transactions on Antennas and Propagation*, Vol. AP-20, pp. 637-641, Sep. 1972.
- [4] W.J. Hendricks, "The Totally Random Versus the Bin Approach for Random Arrays", *IEEE Transactions on Antennas and Propagation*, Vol. AP-39, pp. 1757-1762, Dec. 1991.
- [5] P.R. Haddad and D.M. Pozar, "Anomalous Mutual Coupling Between Microstrip Antennas", *IEEE Transactions on Antennas and Propagation*, Vol. AP-42, pp. 1545-1549, Nov. 1994.
- [6] B.W. Kwan, Mutual Coupling Analysis for Conformal Microstrip Antennas, Ph.D. dissertation, Dept. Elec. Eng., Ohio State University, Columbus, Ohio.
- [7] D.M. Pozar, "Analysis of Finite Phased Arrays of Printed Dipoles", *IEEE Transactions on Antennas and Propagation*, Vol. AP-33, pp. 1045-1053, Oct. 1985.
- [8] R.G. Malech, "The Reflectarray Antenna System", 12th Annual Antenna Symposium, USAF Antenna Research and Development Program 1, University of Illinois, 1962.
- [9] D.G. Berry and R.G. Malech, "The Reflectarray Antenna", *IEEE Transactions on Antennas and Propagation*, Vol. AP-11, pp. 645-651, Nov. 1963.
- [10] R. Tang and R.W. Burns, "Phased Array Antenna for Airborne Applications", *Microwave Journal*, pp. 31-38, Jan. 1971.
- [11] C.S. Malagisi, "Microstrip Disc Element Reflectarray", Electronics and Aerospace Systems Convention, Sep. 1978.
- [12] J.P. Montgomery, "Scattering by an Infinite Periodic Array of Microstrip Elements", *IEEE Transactions on Antennas and Propagation*, Vol. AP-26, pp. 850-853, Nov. 1978.

- [13] T.A. Metzler, Design and Analysis of a Microstrip Reflectarray, Ph.D. dissertation, University of Massachusetts, September 1992.
- [14] D.M. Pozar and T.A. Metzler, "Analysis of a Reflectarray Antenna Using Microstrip Patches of Variable Size", *Electronics Letters*, vol. 29, pp. 657-658, April 1993.
- [15] D.M. Pozar, personal communication, 1994.
- [16] D.M. Pozar, S.D. Targonski, and H.D. Syrigos, "Design of Millimeter Wave Microstrip Reflectarrays", submitted for publication in the *IEEE Transactions on Antennas and Propagation*
- [17] R.C. Hansen (ed.), Microwave Scanning Antennas, Peninsula Publishing, Los Altos, Vol 1, Chap. 2, pp. 139-146.
- [18] C.A. Balanis, Antenna Theory, Analysis and Design, Harper and Row, New York, 1982, pp. 468-469.
- [19] A.W. Rudge, K. Milne, A.D. Olver, and P. Knight (ed.), The Handbook of Antenna Design, vol. 2, chap. 9, pp. 75-76.
- [20] J.D. Worembke, "Soft Substrates Conquer Hard Designs", *Microwaves*, Hayden Publishing Co., Inc., Vol. 21, pp. 89-98, Jan. 1982.
- [21] H.D. Syrigos, "Backfire Feed Antenna Beats Cassegrain Design", *Microwave System News*, October 1983.
- [22] P.W. Hannan, "Microwave Antennas Derived from the Cassegrain Telescope", *IRE Transactions on Antennas and Propagation*, vol. AP-9, pp. 140-153, Mar. 1961.